

**UNIVERSITAT POLITÈCNICA DE VALÈNCIA**

**INSTITUTO INTERUNIVERSITARIO DE INVESTIGACIÓN DE  
RECONOCIMIENTO MOLECULAR Y DESARROLLO TECNOLÓGICO**



**Development of a reproducible and optimized  
synthetic protocol for the preparation of  
monodisperse core-shell-type magnetic  
mesoporous silica nanoparticles**

**PhD. THESIS**

Submitted by

**Santiago Sánchez Cabezas**

PhD. Supervisors:

**Dr. Vicent Esteve Moya**

**Dr. Félix Sancenón Galarza**

**Prof. Ramón Martínez Máñez**

Valencia, July 2019



*A mi familia*



*“Si buscas resultados distintos, no hagas siempre lo mismo”.*

**Albert Einstein.**

*“I have yet to see any problem, however complicated, which, when you look at it in the right way, did not become still more complicated”.*

**Poul Anderson.**

*“You can’t always get what you want, but if you try sometimes you might just find, you get what you need”.*

**The Rolling Stones.**



## Acknowledgements

Es difícil expresar en unas pocas líneas el agradecimiento que siento por todas esas personas que, de alguna forma o de otra, han hecho posible esta tesis. Algunas veces ha sido simplemente un consejo o una reflexión, otras veces ha sido compartir tiempo, dedicación y conocimientos. Pero sobre todo, en estos 5 años he tenido la suerte de compartir laboratorio y experiencias con gente realmente extraordinaria que han mostrado día a día su gran potencial humano. Por eso, no me cansaré de agradecer todo lo que habéis hecho por mí durante estos años tanto a nivel profesional como personal: Cris M., Lluís, Mar, Cris G., Àngela, María Moragues, Carol, Alba, Irene, Mónica, Sameh, Elena, Carmen, Andrea Bernardos, Mari Carmen, Toni, Lorena, Anita, Luis Pla, Maria Elena, Bea Lozano, Andy, Tania, Hazem, Ismael, Bea de Luis, Xente, Eva G., Àngels, Marta, María Alonso, Borja, Pablo, Eva B., Quique y Paula. ¡Sois un grupo extraordinario!

No quiero olvidarme de los compañeros con los que más he convivido, el grupo de la CPI: María Ruiz, Édgar, Cris T., Natali, Sara, Adrián y sobre todo Elisa. Son muchos los momentos que hemos compartido juntos y que guardaré como uno de los regalos más bonitos de la tesis. ¡Gracias! Por último, quiero agradecer a Amelia el haber estado ahí desde el primer hasta el último día (literalmente) y el haberme acompañado y cuidado tanto durante este camino que no siempre ha sido fácil. Gracias por tantos momentos, charlas y sobre todo buena comida!

También quiero dar las gracias a todos los investigadores con los que he tenido la suerte de colaborar en distintos proyectos, algunos de los cuales han quedado fuera del alcance de esta tesis. Gracias a Roberto por tantas horas de trabajo en el proyecto de hipertermia magnética y por estar siempre dispuesto a fabricar nuevos equipos para estudiar el comportamiento magnético de mis materials. Gracias a Clara y Javi del Hospital Universitari y Politècnic la Fe por confiar en mí y dedicar tanto esfuerzo al proyecto de Distrofia Muscular de Duchenne. Son muchas las cosas que hemos aprendido día a día, experimento a experimento, enfrentándonos siempre a las complicaciones con una sonrisa y la esperanza de conseguir nuestro objetivo en el próximo intento. Por último, quiero agradecer a Isabel Fariñas todo su tiempo e interés en el proyecto de seguimiento de células leucémicas a través de nanopartículas magnéticas, así como la dedicación y esfuerzo de Salomé y Sara en las múltiples pruebas realizadas. Ha sido un placer poder trabajar con vosotras

y aprender juntos tantas cosas sobre el complicado mundo de las interacciones entre nanodispositivos y sistemas celulares.

También quiero agradecer a Eduardo Ruiz todo su trabajo y ayuda en el proyecto de agentes teranósticos y neuroblastoma, así como la oportunidad que me ofreció para trabajar unos meses en su laboratorio del RCSI en Dublin. Gracias por estar siempre disponible a pesar de tu increíblemente ajetreada agenda: eres un gran profesional y por encima de todo una gran persona. Gracias también a Juan Gallo por su inestimable ayuda desde que comencé el doctorado y por compartir conmigo un poquito de su conocimiento. La semana en el laboratorio del INL en Braga fue quizá una de las más intensas y productivas de todo el doctorado: gracias por la ayuda con los experimentos y gracias también a Lorena García por su colaboración.

Quiero dar las gracias a Javier Castells por estar siempre dispuesto a hablar sobre ciencia y sobre mi proyecto, así como por su ayuda inestimable con medidas, software e incluso algún experimento. Gracias Javi, eres grande de verdad. También han sido muchas las charlas y discusiones con Luis Villaescusa, que siempre ha tenido abierta la puerta de su despacho para escuchar mis dudas, darme buenos consejos y sobre todo hablar de música! Gracias también a Loles por aconsejarme cada vez que he tenido alguna duda y por enseñarme a realizar el “mapping” con el microscopio electrónico. No puedo olvidar tampoco al gran equipo de técnicos del servicio central de microscopía de la UPV: Merche, Jose Luís, Manolo, Alicia y Chimo. Gracias por vuestra ayuda y consejo en todas y cada una de las técnicas que he utilizado (que no han sido pocas) y gracias por vuestra amabilidad y profesionalidad. I also want to thank Greg and Jen their support, especially their help checking the grammar and vocabulary of some of my works!

Quiero dar las gracias a mis directores de tesis Félix y Ramón por confiar en mí y sobre todo a Vicent, sin el cual esta tesis no hubiera sido posible. Gracias por tu interés en mi trabajo y por animarme en los momentos más difíciles. Ha sido todo un placer desarrollar contigo este proyecto y sobre todo descubrir esa forma de hacer ciencia que resulta tan gratificante. Gracias por estar ahí siempre que ha hecho falta, fuera de todo horario y en cualquier situación. No resulta nada fácil encontrar a una persona tan brillante y cercana al mismo tiempo. De todo corazón, gracias!



No puedo olvidarme de todos los profesores que tanto en el instituto de Enguera como en la Universidad de Valencia fueron poco a poco cultivando mi pasión por la ciencia y la investigación. Carmen Ramón, Teresa Córdoba y sobre todo Juan Hernández: vuestra forma de transmitir ciencia fue todo un ejemplo para mí, muchísimas gracias. Y gracias también a Rosendo, Ochando, Marga, Pepe Moratal, Rosa y Tere: sin duda mi pasión por la investigación bebió directamente de la ilusión que nos transmitisteis a lo largo de la carrera. Es algo que nunca olvidaré, gracias!

Como no, quiero dar las gracias a todos esos amigos que han estado a mi lado y han sido parte imprescindible de esta etapa de mi vida: Jorge M., Matías, Carles, Miguel, Carlos, Enrique, Rebeca, María, Jose, Sergio y Jorge. Gracias por vuestro apoyo y por compartir conmigo tantos buenos momentos, sin esa fuente de energía hubiese costado mucho llegar al final de este proyecto. También quiero dar las gracias a Margarita por sus sabios consejos y por ayudarme a recalcular la ruta cada vez que me extraviaba. Muchísimas gracias.

Quiero por último dar las gracias a mi familia: sin vuestro apoyo y cariño esto no hubiera sido posible. Gracias Charo por estar ahí cada vez que ha hecho falta. Gracias David por compartir tantos momentos. Y sobre todo, gracias papá y mamá por ser como sois y por todo lo que me habéis enseñado. Sabéis que sin vuestro apoyo nada de esto hubiera sido posible. No creo que pueda haber persona más afortunada que yo. GRACIAS.



## Resumen

La fabricación de nanopartículas con tamaños por debajo de los 100 nm ha permitido el desarrollo de innovadores nanodispositivos capaces de interactuar de forma directa con sistemas vivos a nivel celular y molecular, convirtiéndose en una parte fundamental dentro del campo de la nanomedicina. Uno de los principales retos a los que se enfrenta la ingeniería de nanopartículas es el desarrollo de nanodispositivos con propiedades físico-químicas bien definidas, ya que de ellas depende el comportamiento y biodistribución de dichos sistemas una vez introducidos en el organismo. No menos importante es el desarrollo de protocolos de síntesis reproducibles y optimizados, indispensables para la fabricación y escalado de nanodispositivos que puedan ser trasladados a futuras aplicaciones biomédicas.

El principal objetivo de este proyecto de doctorado es el estudio y fabricación de nanopartículas magnéticas mesoporosas de sílice con estructura “core-shell” para su aplicación como agentes teranósticos en el campo de la nanomedicina. En este estudio se analiza en profundidad la síntesis y caracterización de dichos nanomateriales con el objetivo de producir nanopartículas con unas propiedades físico-químicas bien definidas de forma controlada y reproducible. La obtención de dichas nanopartículas supondría un gran avance de cara al desarrollo de nanodispositivos más complejos y sofisticados.

El contenido de la tesis se ha estructurado en distintos capítulos que se detallan brevemente a continuación:

- **El capítulo 1** es una introducción a la nanomedicina, destacando el papel fundamental que tienen las nanopartículas en el desarrollo de nuevas aplicaciones biomédicas. A continuación se presentan las nanopartículas de sílice mesoporosa, mostrando la gran versatilidad de dichos nanomateriales para el desarrollo de dispositivos teranósticos así como sistemas para la liberación controlada de fármacos. Por último, se destaca la importancia de fabricar nanodispositivos con unas propiedades físico-químicas bien definidas como requisito indispensable para la traslación de los resultados experimentales hacia el campo clínico.

- **El capítulo 2** incluye los objetivos principales de la tesis así como los objetivos específicos propuestos para cada capítulo de la tesis.
- **El capítulo 3** se centra en la síntesis y caracterización de nanopartículas superparamagnéticas de óxido de hierro (USPIONS), siendo estas utilizadas en capítulos posteriores para la síntesis de las nanopartículas mesoporosas tipo “core-shell”. Las USPIONS son preparadas a través de un método sencillo de coprecipitación en el que se emplean condiciones de reacción moderadas. Las nanopartículas obtenidas son caracterizadas en profundidad, analizando sus propiedades magnéticas para su aplicación en hipertermia magnética y como agentes de contraste dual en imagen por resonancia magnética (MRI).
- **El capítulo 4** está dedicado a la preparación de nanopartículas magnéticas mesoporosas de sílice con estructura “core-shell”. Los conceptos fundamentales relacionados con los mecanismos de formación de este tipo de nanomateriales son ampliamente analizados, así como los parámetros de reacción involucrados en la síntesis. Como punto de partida, se propone un protocolo de síntesis general para la obtención de las nanopartículas tipo “core-shell”. A continuación, se analiza en profundidad el efecto que los distintos parámetros de reacción tienen en las propiedades físico-químicas de dichas nanopartículas. Para la fase de optimización se utiliza un modelo semi-empírico como referencia, racionalizando los resultados experimentales observados en base a un posible mecanismo de formación.
- **El capítulo 5** se centra en el análisis y caracterización de la estructura mesoporosa de las nanopartículas tipo “core-shell”. Además, se analiza el efecto que los distintos parámetros de reacción tienen sobre la estructura final de las nanopartículas, aportando información adicional sobre su posible mecanismo de formación.
- **El capítulo 6** recoge las conclusiones principales de este estudio.

## Resum

La fabricació de nanopartícules amb grandàries per davall dels 100 nm ha permès el desenvolupament d'innovadors nanodispositius capaços d'interactuar de forma directa amb sistemes vius a nivell cel·lular i molecular, convertint-se en una part fonamental dins del camp de la nanomedicina. Un dels principals reptes als quals s'enfronta l'enginyeria de nanopartícules és el desenvolupament de nanodispositius amb propietats físic-químiques ben definides, ja que d'elles depèn el comportament i biodistribució d'aquests sistemes una vegada introduïts en l'organisme. No menys important és el desenvolupament de protocols de síntesi reproduïbles i optimitzats, indispensables per a la fabricació a gran escala de nanodispositius que puguen ser utilitzats en futures aplicacions biomèdiques.

El principal objectiu d'aquest projecte de doctorat és l'estudi i fabricació de nanopartícules magnètiques mesoporoses de sílice amb estructura "core-shell" per a la seua aplicació com a agents teranòstics en el camp de la nanomedicina. En aquest estudi s'analitza en profunditat la síntesi i caracterització d'aquests nanomaterials amb l'objectiu de produir nanopartícules amb unes propietats físic-químiques ben definides de forma controlada i reproduïble. L'obtenció d'aquestes nanopartícules suposaria un gran avanç de cara al desenvolupament de nanodispositius més complexos i sofisticats.

El contingut de la tesi s'ha estructurat en diferents capítols que es detallen breument a continuació:

- El **capítol 1** és una introducció a la nanomedicina, destacant el paper fonamental que tenen les nanopartícules en el desenvolupament de noves aplicacions biomèdiques. A continuació es presenten les nanopartícules de sílice mesoporosa, mostrant la gran versatilitat d'aquests nanomaterials per al desenvolupament de dispositius teranòstics així com sistemes per a l'alliberament controlat de fàrmacs. Finalment, es destaca la importància de fabricar nanodispositius amb unes propietats físic-químiques ben definides com a requisit indispensable per a la translació dels resultats experimentals al camp clínic.
- El **capítol 2** inclou els objectius principals de la tesi així com els objectius específics proposats per a cada capítol de la tesi.

- El **capítol 3** està dedicat a la síntesi i caracterització de nanopartícules superparamagnètiques d'òxid de ferro (USPIONS), sent aquestes utilitzades en capítols posteriors per a la síntesi de les nanopartícules mesoporoses tipus “core-shell”. Les USPIONS són preparades a través d'un mètode senzill de coprecipitació en el qual s'empren condicions de reacció moderades. Les nanopartícules obtingudes són caracteritzades en profunditat, analitzant les seues propietats magnètiques per a la seua aplicació en hipertèrnia magnètica i com a agents de contrast dual en imatge per ressonància magnètica (MRI).
- El **capítol 4** està dedicat a la preparació de nanopartícules magnètiques mesoporoses de sílice amb estructura “core-shell”. Els conceptes fonamentals relacionats amb els mecanismes de formació d'aquest tipus de nanomaterials són àmpliament analitzats, així com els paràmetres de reacció involucrats en la síntesi. Com a punt de partida, es proposa un protocol de síntesi general per a l'obtenció de les nanopartícules tipus “core-shell”. A continuació, s'analitza en profunditat l'efecte que els diferents paràmetres de reacció tenen en les propietats físic-químiques d'aquestes nanopartícules. Per a la fase d'optimització s'utilitza un model semi-empíric com a referència, racionalitzant els resultats experimentals observats sobre la base d'un possible mecanisme de formació.
- El **capítol 5** està dedicat a l'anàlisi i caracterització de l'estructura mesoporosa de les nanopartícules tipus “core-shell”. A més, s'analitza l'efecte que els diferents paràmetres de reacció tenen sobre l'estructura final de les nanopartícules, aportant informació addicional sobre el seu possible mecanisme de formació.
- El **capítol 6** recull les conclusions principals d'aquest estudi.

## Abstract

The fabrication of nanoparticles with sizes below 100 nm has opened the door to the development of innovative nanodevices that directly interact with living systems at the cellular and molecular level, becoming an essential part of nanomedicine. One of the main challenges that nanoparticle engineering is currently facing is the design of nanodevices with well-defined physico-chemical properties, which ultimately determine the fate and function of these systems inside the organism. Similarly, the development of reproducible and versatile synthetic protocols is of great importance for manufacture purposes, a fundamental requirement for an efficient translation of this technology into the clinic.

The main objective of this PhD thesis is the study and fabrication of core-shell-type magnetic mesoporous silica nanoparticles (M-MSNs) for their application as theranostic nanodevices in the field of nanomedicine. A comprehensive study about the synthesis and characterization of this type of nanomaterials is presented with the aim of obtaining core-shell M-MSNs with well-defined physico-chemical properties in a robust and reproducible way. The fabrication of such particles would provide a versatile and reliable platform for the development of more complex nanodevices with advanced functionalities.

The thesis has been structured into several chapters that are briefly summarized as follows:

- **Chapter 1** is an introduction to the topic of nanomedicine, highlighting the importance of nanoparticles in the development of new biomedical applications. Mesoporous silica nanoparticles are then introduced, showing the great versatility that these nanomaterials offer for the development of theranostic nanodevices and smart drug delivery systems. Finally, the development of nanodevices with well-defined physico-chemical properties is identified as a crucial requirement for overcoming biological barriers and facilitate the translation of nanomedicines from the bench to bedside.
- **Chapter 2** presents the aims of this thesis and the specific objectives that are addressed in the following chapters.

- **Chapter 3** is devoted to the synthesis and characterization of ultrasmall superparamagnetic iron oxide nanoparticles (USPIONS), which are later used as magnetic seeds for the synthesis of core-shell M-MSNs. USPIONS are prepared through a simple coprecipitation method using mild reaction conditions. The obtained nanoparticles are fully characterized and their magnetic properties are analyzed focusing on magnetic hyperthermia and dual MR imaging applications.
- **Chapter 4** is a comprehensive study about the preparation of monodisperse core-shell M-MSNs. The main concepts related to the synthesis and formation mechanisms of this type of nanomaterials are revised, together with the reaction parameters that are expected to have a major contribution on the reaction. As a starting point, a general synthetic protocol for the synthesis of core-shell M-MSNs is presented. Then, specific reaction parameters are investigated in order to understand their effect on the physico-chemical properties of the obtained nanoparticles. The application of a semi-empirical model to the optimization stage is presented in an attempt to provide an adequate reference framework to understand the formation of this complex nanodevices.
- **Chapter 5** presents a detailed analysis about the characterization of mesoporous silica materials and, in particular, the assessment of the mesoporous structure of MSNs with a radial distribution of wormhole-like channels. The effects that specific reaction parameters have on the mesoporous silica structure of core-shell M-MSNs are also analysed, providing additional information about the formation of this type of nanoparticles.
- **Chapter 6** gathers the main conclusions of this thesis.



## Publications

Results of this PhD Thesis and other contributions have resulted in the following scientific publications:

- [1] **S. Sánchez-Cabezas**, R. Montes-Robles, J. Gallo, F. Sancenón, and R. Martínez-Máñez, "Combining magnetic hyperthermia and dual T 1/ T 2 MR imaging using highly versatile iron oxide nanoparticles," *Dalt. Trans.*, vol. 48, no. 12, pp. 3883–3892, **2019**.
- [2] A. L. Urbano-Bojorge, O. Casanova-Carvajal, N. Félix-González, L. Fernández, R. Madurga, **S. Sánchez Cabezas**, E. Aznar, M. Ramos, and J.J. Serrano-Olmedo. "Influence of Medium Viscosity and Intracellular Environment on the Magnetization of Superparamagnetic Nanoparticles in Silk Fibroin Solutions and 3T3 Mouse Fibroblast Cell Cultures," *Nanotechnology*, vol. 29, pp. 1–13, **2018**.
- [3] F. L. Portilho, E. Helal-Neto, **S. Sánchez-Cabezas**, S. Rocha Pinto, S. Nascimento dos Santos, L. Pozzo, F. Sancenón, R. Martínez-Máñez, and R. Santos-Oliveria. "Magnetic core mesoporous silica nanoparticles doped with dacarbazine and labelled with 99mTc for early and differential detection of metastatic melanoma by single photon emission computed tomography," *Artif. Cells, Nanomedicine, Biotechnol.*, vol. 0, no. 0, pp. 1–8, **2018**.

## Abbreviations and Acronyms

<b>AMF</b>	Alternating magnetic field
<b>BET</b>	Brunauer, Emmett and Teller (theory)
<b>BJH</b>	Barrett-Joyner-Halenda (method)
<b>CTAB</b>	Cetyltrimethylammonium bromide
<b>DFT</b>	Density functional theory
<b>DLS</b>	Dynamic light scattering
<b>FTIR</b>	Fourier transform infrared spectroscopy
<b>HAADF</b>	High-angle annular dark-field
<b>HRTEM</b>	High resolution transmission electron microscopy
<b>ILP</b>	Intrinsic loss power
<b>IUPAC</b>	International union of pure and applied chemistry
<b>LCT</b>	Liquid crystal templating
<b>MNPs</b>	Magnetic nanoparticles
<b>MSNs</b>	Mesoporous silica nanoparticles
<b>M-MSNs</b>	Magnetic mesoporous silica nanoparticles
<b>MRI</b>	Magnetic resonance imaging
<b>NLDFT</b>	Non-local density functional theory
<b>PDI</b>	Polydispersity index
<b>PSD</b>	Pore size distribution
<b>(P)XRD</b>	(Powder) X-ray diffraction
<b><i>r</i><sub>1</sub></b>	Longitudinal relaxivity

<b><i>r2</i></b>	Transverse relaxivity
<b><i>SAED</i></b>	Selected area electron diffraction
<b><i>SAR</i></b>	Specific absorption rate
<b><i>SEM</i></b>	Scanning electron microscopy
<b><i>siRNA</i></b>	Small interfering ribonucleic acid
<b><i>SPIONs</i></b>	Superparamagnetic iron oxide nanoparticles
<b><i>T1</i></b>	Longitudinal relaxation time
<b><i>T2</i></b>	Transverse relaxation time
<b><i>TEM</i></b>	Transmission electron microscopy
<b><i>TBOS</i></b>	Tetrabutyl orthosilicate
<b><i>TEOS</i></b>	Tetraethyl orthosilicate
<b><i>TMOS</i></b>	Tetramethyl orthosilicate
<b><i>TPOS</i></b>	Tetrapropyl orthosilicate
<b><i>TGA</i></b>	Thermogravimetric analysis
<b><i>USPIONs</i></b>	Ultrasmall superparamagnetic iron oxide nanoparticles
<b><i>ZFC/FC</i></b>	Zero field cooling/field cooling

# Contents

<b>Chapter 1</b>	
General introduction	1
<b>Chapter 2</b>	
Objectives	15
<b>Chapter 3</b>	
Synthesis and characterization of ultrasmall superparamagnetic iron oxide nanoparticles (USPIONs)	21
<b>Chapter 4</b>	
Design of an optimized synthetic protocol for the preparation of monodisperse core-shell magnetic mesoporous silica nanoparticles	53
<b>Chapter 5</b>	
Structural characterization of core-shell magnetic mesoporous silica nanoparticles	117
<b>Chapter 6</b>	
General conclusions	165

## **Chapter 1:**

### ***General introduction***



## 1.1. Nanoparticles in nanomedicine

Nanomedicine is a multidisciplinary area that applies nanotechnology to solve some of the most challenging problems that medicine is currently facing.<sup>1,2</sup> In a general sense, nanotechnology can be defined as the technology that allows to control and manipulate matter at the nanometer-length scale ( $1 \text{ nm} = 10^{-9} \text{ m}$ ), *i.e.* the size range corresponding to atoms, molecules and supramolecular structures.<sup>1</sup> Nanomaterials are defined as those with at least one of their dimensions in the size range between 1 and 100 nm.<sup>3</sup> Due to their extraordinary small sizes, nanomaterials behave differently than their bulk counterparts, exhibiting unique chemical, physical and biological properties.<sup>2</sup> This has led to the development of innovative nanodevices with promising applications in the field of nanomedicine, including drug delivery, *in vivo* imaging, *in vitro* diagnostics and the design of advanced biomaterials and active implants.<sup>4</sup>

Nanoparticles are probably the most popular type of nanomaterials in the field of nanomedicine. Independently of their shape, nanoparticles are characterized by having all three dimensions in the 1-100 nm range, although the term nanoparticle is also frequently applied to particles with sizes up to a few hundred nanometers.<sup>5</sup> Nanoparticles are in the same size range as biomolecules (siRNA, antibodies, proteins...) and in the case of the larger nanoparticles, they are comparable to viruses (Figure 1). Compared to the size of cells, nanoparticles are still considerably small, which makes them ideal platforms to directly interact with these living systems. This has revolutionized the study of biological processes at the cellular and molecular level, making nanomaterials a promising tool for the treatment and diagnosis of different diseases.

One of the main assets of nanoparticle engineering is the possibility to combine different functional components into a single nanodevice, greatly increasing their potential biomedical applications. Imaging agents such as fluorophores, MRI contrast agents, and PET/SPECT radiotracers,<sup>6,7</sup> stimuli-responsive molecular gates,<sup>8,9</sup> targeting ligands<sup>10</sup> and relevant biomolecules<sup>3,11</sup> are just a few examples of the vast repertoire of functionalities that can be incorporated into engineered nanodevices (Figure 2). From drug delivery applications, to improved diagnosis or

targeted therapies, the possibilities that multi-functional nanoparticles offer hold great promise to revolutionize the medicine of the future.<sup>12,13</sup>

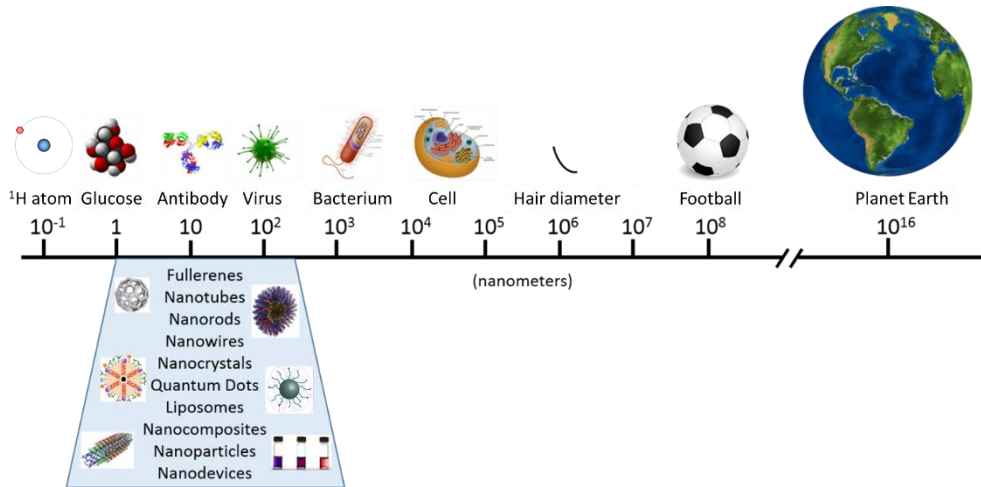


**Figure 1:** Examples of differently-sized structures expressed in nanometers. The size range corresponding to nanomaterials is highlighted, providing several examples.

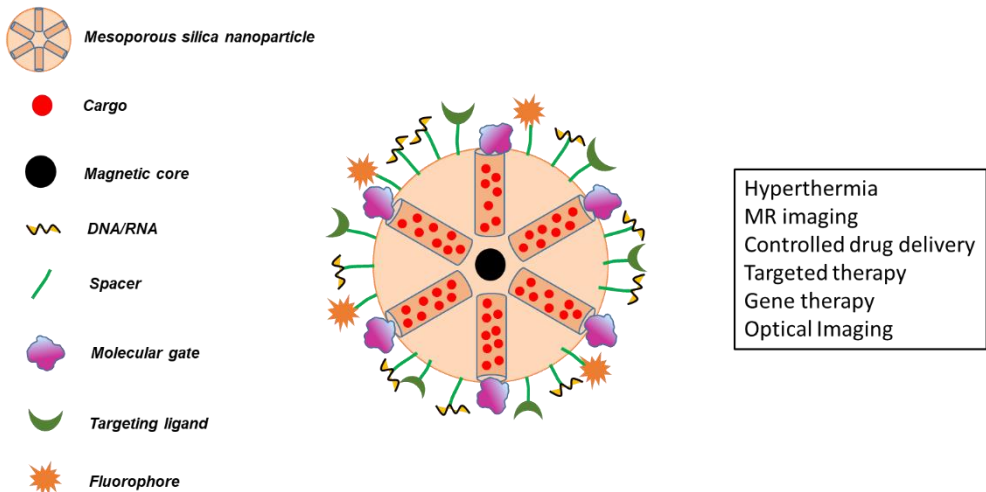


**Figure 2:** Schematic representation of a nanodevice with a core-shell structure and functionalized with several components. Potential biomedical applications are highlighted.



## 1.2. Mesoporous silica nanoparticles

Mesoporous silica nanoparticles (MSNs) have attracted significant attention as multifunctional platforms for the development of biomedical nanodevices. This is mainly due to the unique physico-chemical properties of mesoporous silica, including large surface areas ( $>700 \text{ m}^2/\text{g}$ ) and pore volumes ( $>0.60 \text{ cm}^3/\text{g}$ ), highly uniform and tuneable pore sizes in the mesopore range, ordered periodic structures, ease of functionalization and great thermal and chemical stability.<sup>14,15</sup> Although initially developed as molecular sieves for catalysis and adsorption applications,<sup>16,17</sup> mesoporous silica materials soon attracted attention as drug delivery systems. This application was already suggested back in 2001, when a therapeutic drug, ibuprofen, was successfully encapsulated and released from an ordered mesoporous silica material.<sup>18</sup>

It was also in the early 2000s, when mesoporous silica materials were synthesised for the first time in the form of discrete nanoparticles with sizes below 100 nm.<sup>19–21</sup> The possibility to prepare nanometer-sized particles with drug delivery capabilities opened the door to the development of MSNs for applications within nanomedicine, a research area that keeps continuously growing.<sup>22,23</sup>

### 1.2.1. Gated MSNs as stimuli-responsive nanodevices

An additional level of complexity was achieved when the surface of MSNs was functionalized with organic (bio)molecules and supramolecular structures. The resulting organic-inorganic hybrid materials presented enhanced capabilities arising from the combination of nanomaterials with molecular-based systems.<sup>24</sup> In 2003, Victor Lin and co-workers published a pivotal study that pushed forward the possibilities of MSNs, especially in the field of nanomedicine.<sup>25</sup> In this work, MSNs were first loaded with a drug and then the surface of the nanoparticles was functionalized with cadmium sulphide (CdS) nanocrystals, which blocked the outlets of the pores and entrapped the drug within the mesoporous structure. The great achievement of this work was that the CdS nanocrystal caps could be removed on-command by using different redox stimuli, which triggered the release of the encapsulated cargo. Using a similar approach, the group of Fujiwara employed UV-light to trigger the release of guest molecules encapsulated in

mesoporous silica materials functionalized with a photo-responsive coumarin derivative.<sup>26,27</sup> To control the uptake and release of guests molecules from MSNs opened the door to the development of stimuli-responsive hybrid nanodevices, which have found important applications as smart delivery systems.<sup>23,28</sup> Several reviews can be found in the literature that cover the synthesis and applications of these versatile materials.<sup>9,29</sup>

### **1.2.2. Theranostic MSNs**

The combination of different functional materials into a single nanodevice led to the development of theranostic agents, *i.e.* systems that present both therapeutic and diagnostic capabilities.<sup>30</sup> For example, MSNs can be loaded and functionalized with several types of therapeutic agents and diagnostic markers.<sup>31</sup> MSNs can also be combined with magnetic nanoparticles, a particularly interesting approach for the development of theranostic nanodevices.<sup>32</sup>

Magnetic nanoparticles present multiple biomedical applications such as the local production of heat for therapeutic hyperthermia,<sup>33</sup> generation of image contrast in magnetic resonance imaging (MRI)<sup>34</sup> or magnetic targeting for the delivery of nanodevices.<sup>35</sup> They have been incorporated into mesoporous silica materials using different strategies, leading to magnetic mesoporous silica nanoparticles (M-MSNs) with different structures.<sup>36–38</sup> Figure 3 shows three characteristic examples: A) magnetic nanoparticles embedded within the mesoporous silica framework, B) a core-shell type structure in which the mesoporous silica shell has been grown around a central magnetic core and C) a rattle-type structure in which the magnetic core is not directly bound to the mesoporous silica shell.

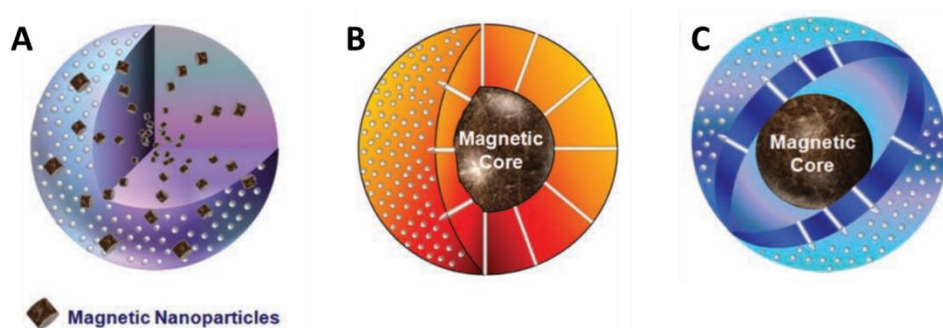


**Figure 3:** Schematic representation of three different types of M-MSNs. Magnetic nanoparticles embedded within the mesoporous silica framework (A), core-shell-type M-MSNs (B) and rattle-type M-MSNs. Reprinted with permission from *Small* 2011, 7 (4), 425–443.

### 1.3. Challenges in clinical translation

Despite the promising biomedical applications of multi-functional nanodevices and the continuously growing number of publications devoted to this research area, the number of approved clinical treatments based on nanomedicine strategies is relatively small, showing a poor translation of results from the lab to the clinic.<sup>39–41</sup> The complexity and sophistication of new nanodevices increases day to day, yet a bottleneck arises when this technology is to be applied in clinical studies. The mismatch between the number of new nanoparticle formulations and the successful translation of this technology to clinical applications was already noted by professor Kinam Park as early as 2003.<sup>42</sup> In this enlightening publication, the author warns about the risks of placing all the efforts on making things smaller, more sophisticated and therefore more complicated, rather than focusing on developing realistic applications that could be transformed into tangible results. In particular, Park stresses that the fever for developing new and innovative nanodevices can just lead to potential applications that would never make a real impact on patient's lives. Three main ideas are presented in order to overcome this situation: proposing realistic goals, identifying the limitations of nanoparticle approaches and maximizing the capabilities of existing nanoparticle systems.

The challenges and limitations that nanomedicine has to face are multiple and have been extensively reviewed by several authors.<sup>4,5,39,40,43,44</sup> However, all these studies agree on a common critical point: the need of overcoming biological barriers in order to reach target sites. Upon administration, nanoparticles encounter several biological barriers at the system, organ and cellular level, which prevent them from reaching the site of action (Figure 4).<sup>40,43,45</sup> Sequestration by the mononuclear phagocyte system (MPS), vascular extravasation into the tumor environment or internalization into target cells are just a few examples. The magnitude of the problem was clearly illustrated by a recent literature survey based on articles published between 2005 and 2015, which found that, on average, only 0.7% of administered nanodevices reach the tumor site.<sup>41</sup> This has direct implications for the clinical translation of nanomedicine, identifying nanoparticle delivery efficiency as the main challenge to address.

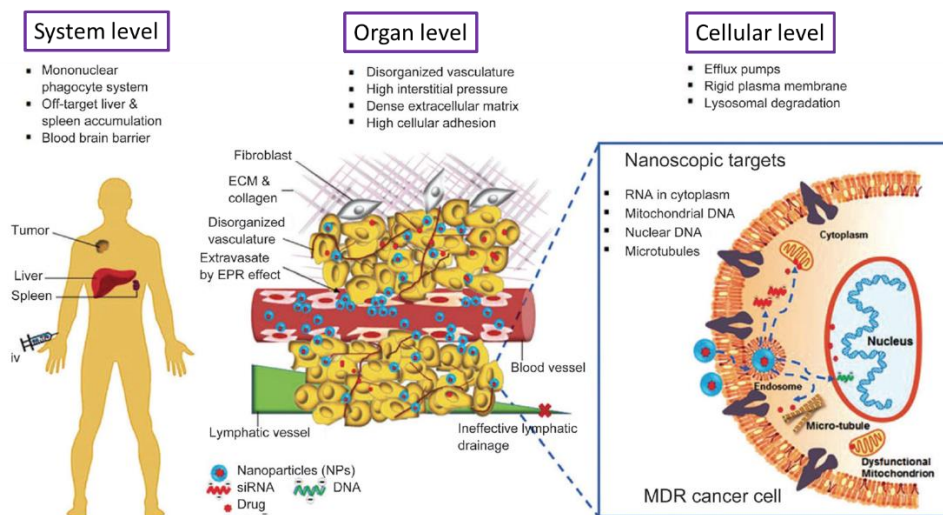


**Figure 4:** Illustration of main biological barriers that engineered nanodevices encounter upon administration. Several examples are provided at the system, organ and cellular level. *Reprinted with permission from Acta Pharmacol. Sin. 2018, 39 (5), 1–20.*

## 1.4. Nanoparticle engineering

Addressing inefficient nanoparticle delivery requires a better understanding of the interactions between engineered nanodevices and biological systems.<sup>5</sup> These interactions are highly influenced by the nanoparticle physico-chemical properties, such as size, shape, composition, charge and surface chemistry (Figure 5).<sup>43,46,47</sup> Thus, the synthesis of nanoparticles with well-defined properties is of crucial importance in order to establish clear structure-activity relationships that could be used as a reference for the rational design of nanodevices.<sup>48</sup> Not surprisingly, optimization of physico-chemical properties has been identified as a fundamental factor for the successful clinical translation of biomedical nanodevices.<sup>5,40</sup>

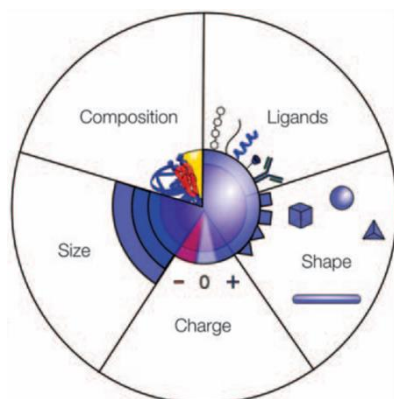


**Figure 5:** Main physico-chemical properties relevant for the design of efficient nanodevices . Reprinted with permission from *RSC Drug Discovery Series*; Braddock, M., Ed.; Royal Society of Chemistry: Cambridge, 2016; pp 1–22.

A second major concern for the clinical translation of engineered nanodevices is related to their biodegradability and clearance from the organism.<sup>48</sup> Once again, the physico-chemical properties of nanoparticles play a fundamental role. To give just an example, control over the degradation of MSNs can be achieved through the tuning of nanoparticle size and morphology, material porosity and degree of aggregation, all directly related to the surface area of the material.<sup>49</sup>

Last but not least, scalable manufacturing has been identified as another important factor to consider in the early development of engineered nanodevices.<sup>5</sup>

Increasing the complexity of nanoparticle formulations usually requires synthetic protocols with multiple steps that pose additional challenges to the scalable manufacturing process. The popular “keep it simple” principle is therefore a useful guideline when developing new nanodevices for biomedical applications.<sup>44</sup>

From the above considerations, it is clear that material sciences and nanoparticle engineering are key to overcome the limitations that nanomedicine is currently facing.

## 1.5. References

- (1) Kewal K, J. *The Handbook of Nanomedicine - Springer*, Third Edit.; Humana Press, **2017**.
- (2) Riehemann, K.; Schneider, S. W.; Luger, T. A.; Godin, B.; Ferrari, M.; Fuchs, H. *Angew. Chemie - Int. Ed.* **2009**, *48* (5), 872–897.
- (3) Conde, J.; Dias, J. T.; Grazú, V.; Moros, M.; Baptista, P. V.; de la Fuente, J. M. *Front. Chem.* **2014**, *2* (July), 48.
- (4) Wagner, V.; Dullaart, A.; Bock, A.-K.; Zweck, A. *Nat. Biotechnol.* **2006**, *24* (10), 1211–1217.
- (5) Shi, J.; Kantoff, P. W. *Med. J. Aust.* **2015**, *203* (5), 20–37.
- (6) Louie, A. *Chem. Rev.* **2010**, *110* (5), 3146–3195.
- (7) Lamb, J.; Holland, J. P. *J. Nucl. Med.* **2018**, *59* (3), 382–389.
- (8) Mura, S.; Nicolas, J.; Couvreur, P. *Nat. Mater.* **2013**, *12* (11), 991–1003.
- (9) Aznar, E.; Oroval, M.; Pascual, L.; Murguía, J. R.; Martínez-Máñez, R.; Sancenón, F. *Chem. Rev.* **2016**, *116*, 561–718.
- (10) Bar-Zeev, M.; Livney, Y. D.; Assaraf, Y. G. *Drug Resist. Updat.* **2017**, *31*, 15–30.
- (11) Conde, J.; Ambrosone, A.; Hernandez, Y.; Tian, F.; McCully, M.; Berry, C. C.; Baptista, P. V.; Tortiglione, C.; De La Fuente, J. M. *Nano Today* **2015**, *10* (4), 421–450.
- (12) Taylor-Pashow, K. M. L.; Della Rocca, J.; Huxford, R. C.; Lin, W. *Chem. Commun. (Camb)*. **2010**, *46* (32), 5832–5849.
- (13) *Multifunctional Nanoparticles for Drug Delivery Applications*; Svenson, S., Prud'homme, R. K., Eds.; Springer US: Boston, MA, **2012**.
- (14) Beck, J. S.; Vartuli, J. C.; Roth, W. J.; Leonowicz, M. E.; Kresge, C. T.; Schmitt, K. D.; Chu, C. T.-W.; Olson, D. H.; Sheppard, E. W.; McCullen, S. B.; Higgins, J. B.; Schlenker, J. L. *J. Am. Chem. Soc.* **1992**, No. 14, 10834–10843.
- (15) Grun, M.; Unger, K. K.; Matsumoto, A.; Tsutsumi, K. *Microporous Mesoporous Mater.* **1999**, *27*, 207–216.
- (16) Zhao, X. S.; Lu, G. Q. M.; Millar, G. J. *Ind. Eng. Chem. Res.* **1996**, *35* (7), 2075–2090.
- (17) Edler, K. J. In *Porous Materials*; Bruce, D. W., O'Hare, D., Walton, R. I., Eds.; Wiley, **2011**; pp 69–145.
- (18) Vallet-Regí, M.; Rámila, A.; P. del Real, R.; Pérez-Pariente, J. *Chem. Mater.* **2001**, No. 13, 308–311.
- (19) Cai, Q.; Luo, Z. S.; Pang, W. Q.; Fan, Y. W.; Chen, X. H.; Cui, F. Z. *Chem. Mater.* **2001**, *13* (2), 258–263.
- (20) Fowler, C. E.; Khushalani, D.; Lebeau, B.; Mann, S. *Adv. Mater.* **2001**, *13* (9), 649–652.
- (21) Nooney, R. I.; Thirunavukkarasu, D.; Yimei, C.; Josephs, R.; Ostafin, A. E.

- Chem. Mater.* **2002**, *14* (11), 4721–4728.
- (22) Rosenholm, J. M.; Sahlgren, C.; Lindén, M. *Nanoscale* **2010**, *2* (10), 1870–1883.
- (23) Li, Z.; Barnes, J. C.; Bosoy, A.; Stoddart, J. F.; Zink, J. I. *Chem. Soc. Rev.* **2012**, *41* (7), 2590.
- (24) B. Descalzo, A.; Martínez-Mañez, R.; Sancenón, F.; Hoffmann, K.; Rurack, K. *Angew. Chem. Int. Ed.* **2006**, *45*, 5924–5948.
- (25) Lai, C. Y.; Trewyn, B. G.; Jeftinija, D. M.; Jeftinija, K.; Xu, S.; Jeftinija, S.; Lin, V. S. Y. *J. Am. Chem. Soc.* **2003**, *125* (15), 4451–4459.
- (26) Mal, N. K.; Fujiwara, M.; Tanaka, Y.; Taguchi, T.; Matsukata, M. *Chem. Mater.* **2003**, *15* (17), 3385–3394.
- (27) Kishor Mal, N.; Fujiwara, M.; Tanaka, Y. *Nature* **2003**, *421* (January), 350–353.
- (28) Colilla, M.; González, B.; Vallet-Regí, M. *Biomater. Sci.* **2013**, *1* (2), 114–134.
- (29) Sancenón, F.; Pascual, L.; Oroval, M.; Aznar, E.; Martínez-Mañez, R. *ChemistryOpen* **2015**, *4* (4), 418–437.
- (30) Ma, X.; Zhao, Y.; Liang, X.-J. *Acc. Chem. Res.* **2011**, *44* (10), 1114–1122.
- (31) Ambrogio, M. W.; Thomas, C. R.; Zhao, Y.-L.; Zink, J. I.; Stoddart, J. F. *Acc. Chem. Res.* **2011**, *44* (10), 903–913.
- (32) Lee, J. E.; Lee, N.; Kim, T.; Kim, J.; Hyeon, T. *Acc. Chem. Res.* **2011**, *44* (10), 893–902.
- (33) Lee, J.-H.; Jang, J.; Choi, J.; Moon, S. H.; Noh, S.; Kim, J.; Kim, J.-G.; Kim, I.-S.; Park, K. I.; Cheon, J. *Nat. Nanotechnol.* **2011**, *6* (7), 418–422.
- (34) Gallo, J.; Long, N. J.; Aboagye, E. O. *Chem. Soc. Rev.* **2013**, *42* (19), 7816–7833.
- (35) Hauser, A. K.; Wydra, R. J.; Stocke, N. A.; Anderson, W.; Hilt, J. Z. *J. Control. Release* **2015**, *219* (10), 76–94.
- (36) Liu, J.; Qiao, S. Z.; Hu, Q. H.; Lu, G. Q. *Small* **2011**, *7* (4), 425–443.
- (37) Deng, Y.; Cai, Y.; Sun, Z.; Zhao, D. *Chem. Phys. Lett.* **2011**, *510* (1–3), 1–13.
- (38) Wang, Y.; Gu, H. *Adv. Mater.* **2014**, 1–10.
- (39) Hare, J. I.; Lammers, T.; Ashford, M. B.; Puri, S.; Storm, G.; Barry, S. T. *Adv. Drug Deliv. Rev.* **2017**, *108*, 25–38.
- (40) Zhang, R. X.; Li, J.; Zhang, T.; Amini, M. A.; He, C.; Lu, B.; Ahmed, T.; Lip, H.; Rauth, A. M.; Wu, X. Y. *Acta Pharmacol. Sin.* **2018**, *39* (5), 1–20.
- (41) Wilhelm, S.; Tavares, A. J.; Dai, Q.; Ohta, S.; Audet, J.; Dvorak, H. F.; Chan, W. C. W. *Nat. Rev. Mater.* **2016**, *1* (5), 1–12.
- (42) Park, K. *ACS Nano* **2013**, *7* (9), 7442–7447.
- (43) Petros, R. a; DeSimone, J. M. *Nat. Rev. Drug Discov.* **2010**, *9* (8), 615–627.
- (44) Duncan, R.; Gaspar, R. *Mol. Pharm.* **2011**, *8* (6), 2101–2141.
- (45) Blanco, E.; Shen, H.; Ferrari, M. *Nat. Biotechnol.* **2015**, *33* (9), 941–951.
- (46) Sanhai, W. R.; Sakamoto, J. H.; Canady, R.; Ferrari, M. *Nat. Nanotechnol.*



- 2008**, 3 (5), 242–244.
- (47) J.M., A.; J.-A., C.; K., N. In *RSC Drug Discovery Series*; Braddock, M., Ed.; Royal Society of Chemistry: Cambridge, **2016**; pp 1–22.
- (48) Dogra, P.; Adolphi, N. L.; Wang, Z.; Lin, Y. S.; Butler, K. S.; Durfee, P. N.; Croissant, J. G.; Noureddine, A.; Coker, E. N.; Bearer, E. L.; Cristini, V.; Brinker, C. J. *Nat. Commun.* **2018**, 9 (1), 1–14.
- (49) Croissant, J. G.; Brinker, C. J. *Biodegradable Silica-Based Nanoparticles: Dissolution Kinetics and Selective Bond Cleavage*, First Ed.; Elsevier Inc., **2018**; Vol. 43.



## **Chapter 2: Objectives**



## 2.1. Scope of the project

The scope of this PhD project is the design and fabrication of multi-functional nanodevices with application in the field of nanomedicine. Being aware of the limitations and challenges that nanomedicine is currently facing, the focus was not placed on increasing the complexity of current nanodevices. Instead, we were interested in having a better understanding of existing nanoparticle systems that already present promising biomedical applications. The novelty of our approach is to reevaluate how they are produced and synthesized with the objective of obtaining high-quality nanomaterials that could be translated into the clinic more efficiently.

Having this goal in mind, we decided to focus on two fundamental issues: the lack of reproducibility and the lack of control over the physico-chemical properties of engineered nanomaterials. As a result, three main priorities have been established, being used as a guideline across this project:

- The development of robust synthetic protocols for the reproducible preparation of target nanodevices. Reproducibility is critical in order to obtain high-quality nanomaterials with well-defined physico-chemical properties.
- Identifying the effect that specific reaction parameters have on the developed reactions in order to precisely control the physico-chemical properties of the obtained nanomaterials and design versatile nanodevices that can adapt to different needs.
- Conducting a full characterization of the obtained nanomaterials in order to maximize their potential applications and predict their behavior in biologically-relevant scenarios.

## 2.2. Specific objectives

As already mentioned, core-shell M-MSNs combine the multiple biomedical applications of magnetic nanoparticles with the versatility of mesoporous silica materials, representing a fantastic multi-functional platform for the development of theranostic nanodevices. The specific goal of this project is to provide a comprehensive study about the synthesis and characterization of this type of materials.

The present work has been structured into two main sections: a first part devoted to the preparation of magnetic iron oxide nanoparticles and a second part corresponding to the fabrication of the core-shell M-MSNs.

Specific objectives (chapter 3):

- To prepare stable and monodisperse ultrasmall superparamagnetic iron oxide nanoparticles (USPIONS) through a simple synthetic methodology using mild-reaction conditions.
- To fully characterize the magnetic properties of the USPIONS and evaluate their heating efficiency for hyperthermia applications together with their performance as dual  $T1/T2$  MRI contrast agents.
- To evaluate the chemical and physical stability of the obtained USPIONS. This is essential in order to use them as magnetic cores for the preparation of core-shell M-MSNs in section II.

Specific objectives (chapter 4 and 5):

- To analyze the synthesis of surfactant-templated materials in general and the synthesis of core-shell M-MSNs in particular.
- To develop a reproducible synthetic protocol for the preparation of monodisperse core-shell M-MSNs with a uniform size.
- To identify key reaction parameters in order to adjust specific nanoparticle properties, including nanoparticle size, porosity and degree of aggregation.
- To investigate the processes involved in the formation of core-shell M-MSNs and apply a mechanistic model in order to rationalize the

optimization of the synthesis and predict the effect of specific reaction parameters.

- To conduct a comprehensive characterization study in order to determine key structural parameters such as the size and distribution of mesoporous channels, the loading capacity of the material.





## **Chapter 3\***

# ***Synthesis and characterization of ultrasmall superparamagnetic iron oxide nanoparticles (USPIONS)***

**\*The content of this chapter has been published as:**

Sánchez-Cabezas, S.; Montes-Robles, R.; Gallo, J.; Sancenón, F. and Martínez-Mañez, R. *Combining magnetic hyperthermia and dual T1/ T2 MR imaging using highly versatile iron oxide nanoparticles. Reprinted with permission from Dalt. Trans.* **2019**, *48* (12), 3883–3892.



### 3.1. Introduction

Magnetic nanoparticles (MNPs) present unique physico-chemical properties that make them very attractive for different biomedical applications, including magnetic hyperthermia,<sup>1</sup> drug delivery,<sup>2</sup> gene magnetofection<sup>3</sup> and magnetic resonance imaging (MRI).<sup>4</sup> In particular, iron oxide nanoparticles in the form of magnetite and maghemite are, without doubt, the most studied MNPs for clinical applications, having been used as MRI contrast agents for decades.<sup>5</sup> Iron oxide nanoparticles are usually classified based on their size. Superparamagnetic iron oxide nanoparticles (SPIONs) have a colloidal nanoparticle size above 50 nm and are easily sequestered by the mononuclear phagocyte system (MPS), which makes them ideal to image and diagnose liver disorders.<sup>6</sup> However, their short blood circulation time limits their clinical applications and some formulations have been removed from the market due to their limited scope.<sup>7</sup> On the other hand, ultrasmall superparamagnetic iron oxide nanoparticles (USPIONs) have longer blood half-life due to their reduced size (hydrodynamic diameter below 50 nm) and a surge of interest has emerged for the development of a new generation of MRI contrast agents based on these type of nanoparticles.<sup>7</sup>

MRI contrast agents are able to reduce the relaxation times of surrounding water protons under the influence of an external magnetic field. Reduction of longitudinal relaxation times,  $T1$ , results into positive contrast (brighter images, signal enhancement), whereas reduction of transverse relaxations times,  $T2$ , leads to a negative contrast (darker images, signal destruction).<sup>8</sup> Although both processes occur simultaneously, conventional contrast agents are classified as  $T1$  or  $T2$  depending on the relaxation time that experiences a major reduction in the presence of the contrast agent.<sup>9</sup> On the other hand, dual-mode contrast agents have the advantage of providing good contrast in both  $T1$  and  $T2$ -weighted images, offering unequivocal detection and facilitating the clinical diagnosis of diseases.<sup>10</sup> In the case of iron oxide nanoparticles, their contribution to  $T1$  and  $T2$  relaxation processes

can be modulated by adjusting the nanoparticle size.<sup>11</sup> Accordingly, SPIONS have been traditionally used as  $T_2$  contrast enhancers, whereas smaller USPIOs with crystal sizes below 10 nm and hydrodynamic diameters under 50 nm, have shown great potential as  $T_1$  and dual  $T_1/T_2$  contrast agents.<sup>12–14</sup>

Iron oxide nanoparticles are also efficient therapeutic agents used in magnetic hyperthermia. Under the influence of an alternating magnetic field (AMF), MNPs can transform magnetic energy into heat. The localized generation of heat has been exploited as a therapy for the treatment of tumors, since cancer cells are more sensitive to changes of temperature.<sup>15</sup> Mild hyperthermia (41–46 °C) is used to induce apoptosis in cancer cells while preserving healthy tissues. This therapy is commonly used in combination with radiation or chemotherapy, which results in a synergistic effect that kills cancer cells more efficiently.<sup>16</sup>

Combining magnetic hyperthermia and dual  $T_1/T_2$  MR imaging into a single platform would therefore be especially useful for the development of new theranostic applications, *i.e.* the combination of therapy and diagnosis. However, this is a challenging undertaking because of the inherent physical limitations of magnetic nanoparticles. Large iron oxide nanoparticles present high magnetic moments, which contribute to a better heating efficiency and increased  $T_2$ -signal enhancement. In contrast, their high magnetism impairs their performance as  $T_1$  contrast agents due to the perturbation of  $T_1$  relaxation processes.<sup>11</sup> On the other hand,  $T_1$  relaxation is favoured in small iron oxide nanoparticles but their small size promotes energy dissipation through Néel's relaxation, limiting greatly heat production and thus any potential application for hyperthermia.<sup>17</sup> Accordingly, most research groups have focused on either increasing the heating efficiency and  $T_2$  contrast of the nanoparticles or reducing their size in order to achieve better  $T_1$  contrast. In an attempt to obtain versatile nanoparticles for both hyperthermia and dual  $T_1/T_2$  applications, we decided to investigate the magnetic response of USPIOs with a balanced distribution of nanoparticle sizes.

In this work, we report the preparation of USPIOs using a simple cost-effective synthetic method and evaluate their potential use for both hyperthermia and dual MRI applications. The size of the final nanoparticles was adjusted through a post-synthetic purification strategy, which led to highly-stable USPIOs with a balanced distribution of sizes centered around 10 nm. Magnetic characterization studies revealed that the nanoparticles present high saturation magnetization, being able to produce temperatures in the range of moderate hyperthermia. Interestingly, the nanoparticles also showed dual  $T1/T2$  signal enhancement in MRI experiments using typical clinical magnetic fields of 1.4 and 3.0 T.

## **3.2. Materials and methods**

### **3.2.1. Reagents**

$\text{FeCl}_3 \cdot 6\text{H}_2\text{O}$ ,  $\text{FeCl}_2 \cdot 4\text{H}_2\text{O}$ , oleic acid and cetyltrimethylammonium bromide (CTAB) were purchased from Sigma-Aldrich. Chloroform was purchased from Acros Organics. Ammonia (32%) and ethanol were purchased from Scharlau. 1000 ppm iron solution in nitric acid (single element solution for A.A.S.) was purchased from Fisher Chemical. Reactions were conducted using distilled water.

### **3.2.2. Nanoparticle synthesis**

USPIONS composed of oleate-coated  $\text{Fe}_3\text{O}_4$  magnetite nanocrystals were obtained by a modified coprecipitation method.<sup>18</sup> The reaction was conducted under argon atmosphere with mechanical stirring. In a typical procedure, 50 ml of distilled water were deoxygenated by bubbling argon through the solution. Then, temperature was increased up to 80 °C followed by the addition of 12 g of  $\text{FeCl}_3 \cdot 6\text{H}_2\text{O}$  and 4.9 g of  $\text{FeCl}_2 \cdot 4\text{H}_2\text{O}$ . Ammonia 32% (19.53 ml) was added to the reaction mixture and iron oxide nanoparticles rapidly formed. Oleic acid (2.13 ml) was added after 30 min and the reaction was left stirring for another 90 min at 80 °C. The reaction was allowed to cool to room temperature and centrifuged at 12108 *g* (10 min) in order to precipitate the nanoparticles. Successive cycles of washing and centrifugation (12108 *g*, 10 min) were conducted using distilled water (3 cycles) and ethanol (3 cycles). The resulting black material was dried under vacuum overnight. Finally, the nanoparticles were resuspended in chloroform and centrifuged at 13400 *g* (20 min) in order to discard large aggregates and adjust the size of the final nanoparticles.

### **3.2.3. Water-phase transfer**

In a typical procedure, 1 ml of oleate-coated USPIONS suspended in chloroform (6 mg/ml) was added to a 10 mg/ml solution of CTAB in water. Then, both solutions were thoroughly mixed with a probe sonicator (450 sonifier, Branson Ultrasonics Corporations) giving a homogenous oil-in-water

microemulsion. The mixture was heated at 65 °C with continuous stirring until chloroform was completely evaporated, giving a clear suspension of nanoparticles in water.

### **3.2.4. Material characterization**

#### 3.2.4.1. Standard characterization techniques

Powder X-ray diffraction (PXRD) measurements were conducted using a Bruker AXS D8 Advance diffractometer equipped with CuK $\alpha$  radiation and working at 40 kV/40 mA. The diffraction pattern of iron oxide nanoparticles was recorded in the  $2\theta$  range between 25 and 65°.

TEM analysis was performed on a 100 kV JEOL JEM-1010 transmission electronic microscope operated with AMT image capture engine software. SAED images were obtained using a 200 kV JEM-2100F transmission electronic microscope. Samples were prepared by dropping 10  $\mu$ l of nanoparticles suspended in chloroform onto carbon-coated copper grids, which were left at room temperature until chloroform was completely evaporated. The size of nanoparticles was measured using TEM analysis imaging software. SAED images were analyzed using the Digital Micrograph Software (version 3.7.4).

Dynamic light scattering (DLS) experiments were conducted with a Zetasizer Nano ZS (Malvern Instruments) equipped with a laser of 633 nm and collecting the signal at 173°. Hydrodynamic size distributions were measured three times, from which the average PDI and Z-average values were obtained.

Fourier transform infrared spectroscopy (FTIR) was performed between 4000 and 400  $\text{cm}^{-1}$  in absorbance mode using a Tensor 27 FTIR spectrometer (Bruker).

Thermogravimetric analysis (TGA) was conducted on a TGA/SDTA 851e balance from Mettler Toledo. The analysis was performed using a range of temperatures from 25 to 1000 °C and applying a heating rate of 10 °C/min under a flow of nitrogen.

Atomic absorption spectroscopy (AAS) measurements were conducted on a Perkin Elmer AAnalyst-100 flame atomic absorption spectrometer. Samples were prepared by digesting a 10 mg/ml water suspension of magnetic nanoparticles with nitric acid (1 M) at 55 °C for 48 h. The standard calibration curve was prepared using a 1000 ppm iron solution in nitric acid (single element solution for A.A.S.). The final iron concentration of each sample was obtained as the average value from three independent aliquots, which were digested separately.

Magnetic characterization was conducted on a Quantum Design (USA) MPMS-XL magnetometer. 50 µl of nanoparticles dispersed in chloroform were placed inside a polycarbonate capsule and sealed with vacuum grease. Field dependent magnetization was recorded at 250 K under decreasing field starting from 5 T, in the field range between -5 T and 5 T. In the temperature dependent measurements, the sample was first cooled down to 5 K in zero magnetic field (zero field cooling, ZFC). Then, a magnetic field of 10 mT was applied and the magnetic moment of the sample was measured with increasing temperature. After reaching 270 K, the magnetic moment was measured with decreasing temperature under the presence of a magnetic field of 10 mT (field cooling, FC).

#### 3.2.4.2. Magnetic hyperthermia

Calorimetric experiments to determine the heating efficiency of the nanoparticles were conducted using a custom-made magnetic inductor that generates a stable magnetic field of 15.92 mT at 200 kHz. The magnetic field was generated inside an induction coil composed of a copper pipe, which was refrigerated using a bath circulator (Isotemp, R28 from Fisherband). The different experiments were performed at maximum power. On the centre of the solenoid, the maximum field was estimated using the following equation:

$$B_{max} = \frac{i_{max} \cdot \mu_0 \cdot N}{2 \cdot \sqrt{r^2 \cdot \left(\frac{l}{2}\right)^2}} \quad (1)$$



where  $B_{max}$  represents the maximum field,  $i_{max}$  the maximum current circulating in the inductor,  $\mu_0$  is the permeability of free space,  $N$  is the number of loops,  $l$  is the length of the inductor and  $r$  is the radius. The intensity current was estimated using the Ohm law, registering the voltage in the capacitor. As a result, the estimated maximum field intensity generated by the magnetic inductor was 15.92 mT.

Magnetic induction was applied inside a thermostatic chamber, which was kept at 37 °C for hyperthermia experiments. Samples were measured on disposable plastic cuvettes, which were placed inside an isolating holder at the center of the induction coil. Temperature of the samples was recorded using a fiber optic temperature sensor. The nanoparticles were also characterized using a commercial magnetic hyperthermia equipment (DM 100 system from nB nanoScale Biomagnetics).

#### 3.2.4.3. Relaxivity measurements

Relaxation rates ( $R$ ) were determined at 1.4 T using a minispec mq60 spectrometer from Bruker. Samples from 0 to 125 mM Fe were pre-heated at 37 °C and kept at this temperature during the experiments.  $T_1$  and  $T_2$  relaxation times were measured using standard saturation recovery and cpmg (Carr-Purcell-Meiboom-Gill) sequences respectively. The final relaxivities were obtained from the slope of the linear fit of the inverse of the relaxation times (relaxation rates) against the millimolar concentration of Fe.

MR imaging was performed in a 3.0 T horizontal bore MR Solutions Benchtop MRI system equipped with 48 G/cm actively shielded gradients. To image the samples, a 56-mm diameter quadrature birdcage coil was used in transmit/receive mode. Samples (from 0 to 100 mM Fe) were placed on a custom printed PLA wellplate (300  $\mu$ L) which was then placed in the center of the scanner. Longitudinal relaxation times were measured from  $T_1$  maps acquired using MPRAGE sequences ( $T_I = 12$  values (0.025, 0.05, 0.075, 0.125, 0.225, 0.425, 0.825, 1.625, 3.225, 6.425, 12.825, 23.525 s),  $T_E = 5$  ms,  $T_R = 24$  s,  $A_T = 50$  m 40 s), while transversal relaxation times were measured from  $T_2$  maps acquired through MEMS sequences ( $T_E = 10$  values (0.015 0.03 0.045

0.06 0.075 0.09 0.105 0.120.135 0.15 s),  $T_R = 1400$  ms,  $N_A = 5$  and  $A_T = 32$  m 00 s).  $T_1$  and  $T_2$  maps were reconstructed using ImageJ software (<http://imagej.nih.gov/ij>). As before, the final relaxivities ( $r1/r2$ ) were calculated from the slope of the linear fit of the relaxation rates versus the Fe concentration.

### 3.3. Results and discussion

#### 3.3.1. Nanoparticle synthesis and purification

Regarding the preparation of MNPs, Corot *et al.*<sup>19</sup> highlighted the importance of simple and reliable synthetic methods to obtain high-quality MNPs that do not require complex purification steps. In this work, USPIONS were prepared using a one-step reaction based on the coprecipitation of iron salts in a basic aqueous media under argon atmosphere.<sup>18</sup> Conducting the reaction in water facilitates the scale-up of the reaction and offers an economic and green synthetic route to produce high-quality nanoparticles for biomedical applications. Oleic acid was added to the reaction in order to control the growth of crystals and to stabilize the final nanoparticles, preventing their aggregation.<sup>20</sup> This is critical in order to obtain stable colloidal suspensions of monodisperse nanoparticles. Finally, the obtained nanoparticles were dispersed in chloroform in order to prevent their oxidation, giving a stable magnetic colloidal fluid or ferrofluid (Figure 1).

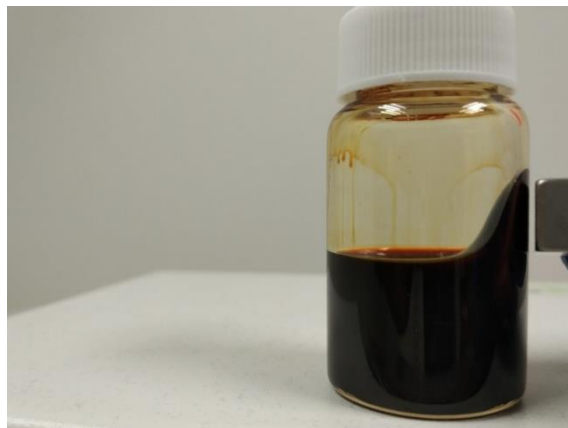


**Figure 1:** Magnetic colloidal fluid (ferrofluid) of oleate-coated USPIONS suspended in chloroform, showing the attractive interaction with a neodymium magnet.

### 3.3.2. Nanoparticle characterization

The mild reaction conditions used in coprecipitation methods usually lead to nanoparticles with a broad size distribution, which is considered the main limitation of this methodology.<sup>21</sup> In an attempt to separate discrete nanoparticles from aggregates and nanoparticles that were not efficiently coated, a post-synthetic purification strategy was implemented. By carefully selecting the time and speed of centrifugation (20 min at 13400 *g*), stable nanoparticles were efficiently separated from aggregates and large nanoparticles.

The size distribution of the nanoparticles during the precipitation procedure was monitored using dynamic light scattering (DLS). As can be seen in Figure 2.A, the initial ferrofluid presented a wide distribution of nanoparticle sizes, which was significantly reduced after the precipitation procedure. The polydispersity index (PDI), a dimensionless parameter used to quantify the size distribution broadness, shifted from 0.25 to 0.11 and the Z-average diameter of the nanoparticles decreased from 57.7 to 25.5 nm. With this simple and reproducible strategy, the initial wide distribution of nanoparticles was adjusted to a population with an average hydrodynamic diameter below 50 nm, the size range assigned to USPIONS.

The size and morphology of the nanoparticles were also assessed using transmission electron microscopy (TEM). The size obtained by TEM analysis refers only to the nanoparticle crystal core, in contrast to the previously obtained hydrodynamic diameter, which considers the size of the whole nanoparticle (core plus organic coating) and the diffuse double-layer of solvent molecules around it. The analysis of 300 measurements from several TEM micrographs revealed that the obtained USPIONS are formed by irregularly shaped crystals, with sizes ranging from 4 to 26 nm (Figure 2.B). This size corresponds to the measurement of the nanoparticles along their major axis, giving an average size of  $10.3 \pm 3.80$  nm. As can be seen in Figure 2.C, the nanoparticle sizes are log-normally distributed. This type of distribution is characteristic of magnetic nanoparticles that have been

obtained through a crystal-growth mechanism, in agreement with previous observations.<sup>22</sup>

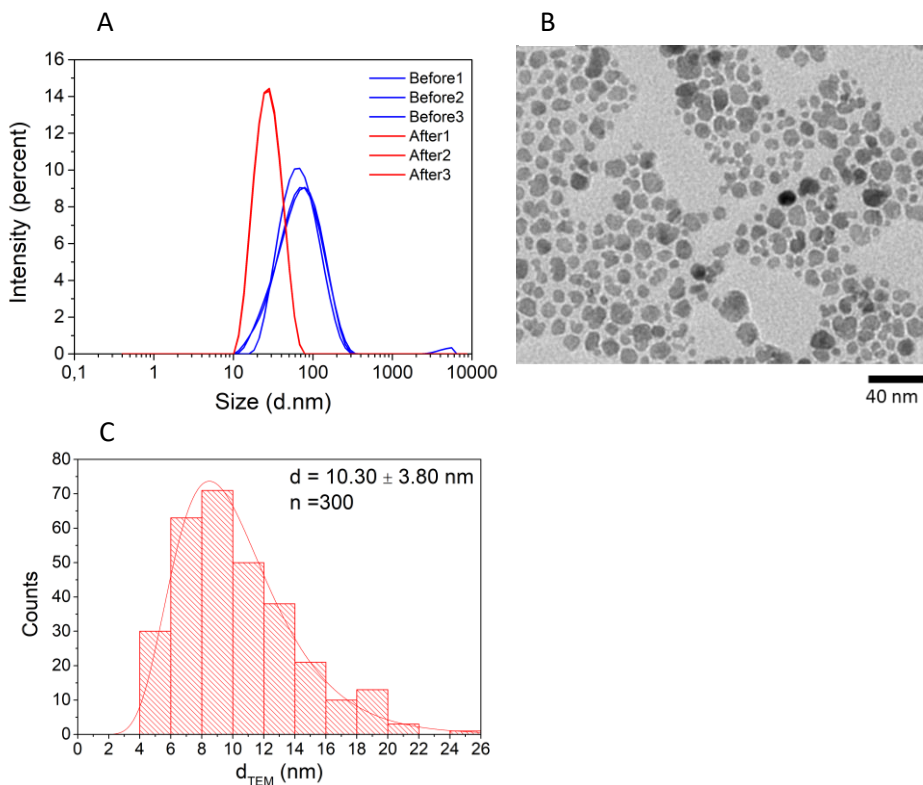


**Figure 2:** Size distribution characterization. (A) Intensity-weighted nanoparticle hydrodynamic size distribution before and after the precipitation procedure. Each measurement was repeated three times. (B) Overview TEM micrograph of oleate-coated USPIOs after separation. (C) Size distribution of oleate-coated USPIOs after separation fitted to a log-normal distribution.

X-ray diffraction studies showed that the obtained USPIOs are highly crystalline, presenting sharp diffraction peaks with  $2\theta$  values of 30.21, 35.63, 43.25, 53.68, 57.28 and 62.89 (Figure 3.A). The values and relative intensities of the peaks are in agreement with the Bragg reflections of magnetite (JCPDS file no. 19-0629), which were indexed as (2 2 0), (3 1 1), (4 0 0), (4 2 2), (5 1 1) and (4 4 0).<sup>23</sup>

Fourier transform infrared spectroscopy (FTIR) was used to study the coating of USPIOs with oleic acid. Oleic acid strongly interacts with the surface of iron oxide nanoparticles through the coordination of the

carboxylate group to the  $\text{Fe}^{2+}/\text{Fe}^{3+}$  atoms.<sup>24</sup> As can be seen in Figure 3.B, the symmetric and asymmetric stretching vibration of C-H bonds in the 2800-3000  $\text{cm}^{-1}$  region are present in the spectrum of both oleic acid and oleate-coated USPIOs but not in the uncoated nanoparticles. In the spectrum of pure oleic acid, the characteristic peak of the carboxylic C=O stretch can be found around 1700  $\text{cm}^{-1}$ . This band is not present in the case of oleate-coated USPIOs, which exhibit two bands at 1516 and 1410  $\text{cm}^{-1}$  that were assigned to the symmetric and asymmetric stretching of carboxylate groups, in agreement with previous studies.<sup>25,26</sup> This result confirms that oleic acid is

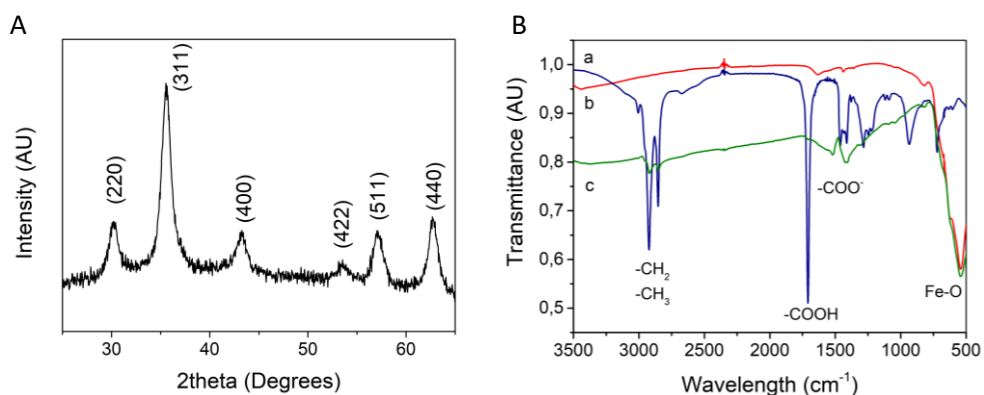


**Figure 3:** Nanoparticle characterization. (A) X-ray diffraction pattern of oleate-coated USPIOs; (B) FTIR spectrum of pure oleic acid (a), uncoated USPIOs (b) and oleate-coated USPIOs (c)

effectively adsorbed on the surface of the nanoparticles as a carboxylate. Finally, the peak at 540  $\text{cm}^{-1}$  was assigned to the Fe-O stretching vibration of the magnetite nanoparticles.

#### 3.3.2.1. Ligand density calculations

The amount of oleate adsorbed on the surface of the nanoparticles was quantified using thermogravimetric analysis (TGA). A sample of pure oleic acid was first analysed in order to determine the temperature range in which oleic acid burns. Complete degradation was observed between 150 and 600 °C, with two main losses around 260 and 360 °C (Figure 4.A). TGA of the oleate-coated SPIONs showed a similar profile, with a 20.5% weight loss corresponding to the degradation of the oleate coating (Figure 4.B). No

further transitions were observed above 600 °C, which indicates that the obtained iron oxide nanoparticles present good thermal stability.

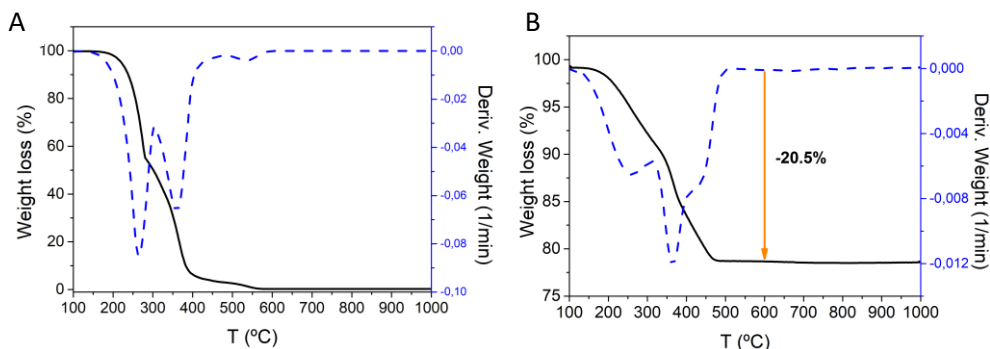


**Figure 4:** TGA and DGT analysis of (A) pure oleic acid and (B) oleate-coated USPIOs.

From the TGA analysis, the amount of oleate molecules in each nanoparticle was estimated according to the following calculations:

- The average volume of a single magnetite nanoparticle ( $V_{NP} = 572.15 \text{ nm}^3$ ) was obtained from equation (2) assuming a spherical shape, where  $R$  is the average nanoparticle radius obtained from TEM image analysis ( $R = 5.15 \text{ nm}$ ):

$$V_{NP} = \frac{4}{3} \pi R^3 \quad (2)$$

- The average mass of a single magnetite nanoparticle ( $m_{NP} = 2.96 \cdot 10^{-18} \text{ g}$ ) was calculated from equation (3), where  $d$  is the density of magnetite ( $d = 5.18 \text{ g/cm}^3$ ):

$$m_{NP} = d \cdot V_{NP} \quad (3)$$

- If we consider 1 g of oleate-coated USPIOs, the amount of oleate ( $m_0$ ) and magnetite ( $m_{USPIOs}$ ) can be estimated using the results from the TGA analysis: 20.5 % (w/w). The ligand density ( $l_d = 1635$  oleate molecules/nanoparticle), can be obtained from equation (4) using the

molecular weight of oleate ( $M_w = 281.46$  g/mol) and the Avogadro's number ( $N_A = 6.022 \cdot 10^{23}$ ):

$$l_d = \frac{\left(\frac{m_o}{M_w}\right) \cdot N_A}{m_{USPIONS}/m_{NP}} \quad (4)$$

The obtained ligand density (1635 oleate molecules/nanoparticle) corresponds to 4.9 oleate molecules/nm<sup>2</sup>. The surface area occupied by the polar head of an oleate molecule is around 21 Å<sup>2</sup>,<sup>27</sup> which means that nearly 5 molecules could be accommodated in a vertical position in 1 nm<sup>2</sup>. This is the ligand density obtained for our oleate-coated USPIONS, which indicates that the surface of the nanoparticles is completely covered by a monolayer of highly-packed oleate molecules. Oleate molecules are most likely arranged in a vertical position with the carboxylate groups interacting with the surface of the nanoparticles and the hydrophobic tails exposed to the outside. This explains the high colloidal stability of the obtained oleate-coated USPIONS in non-polar organic solvents such as chloroform and hexane.

#### 3.3.2.2. Stability study

The colloidal stability of the ferrofluid, which was stored in the fridge for several months, was evaluated by DLS analysis. Measurements were taken at 6 and 8 months after the preparation of the magnetic ferrofluid, showing that the size distribution had not changed with time (Figure 5.A). The absence of aggregation in the ferrofluid is an indicator of the good coverage and strong interaction of the oleate molecules with the surface of the nanoparticles. The chemical integrity of the nanoparticles was also investigated 8 months after the preparation of the ferrofluid using selected area electron diffraction (SAED). The obtained ring diffraction patterns were consistent with the crystal structure of magnetite, indicating that the nanoparticles had not experienced any significant structural modification with time (Figure 5.B). All these results confirmed that the oleate-coated USPIONS are highly stable and can be stored for extended periods of time.

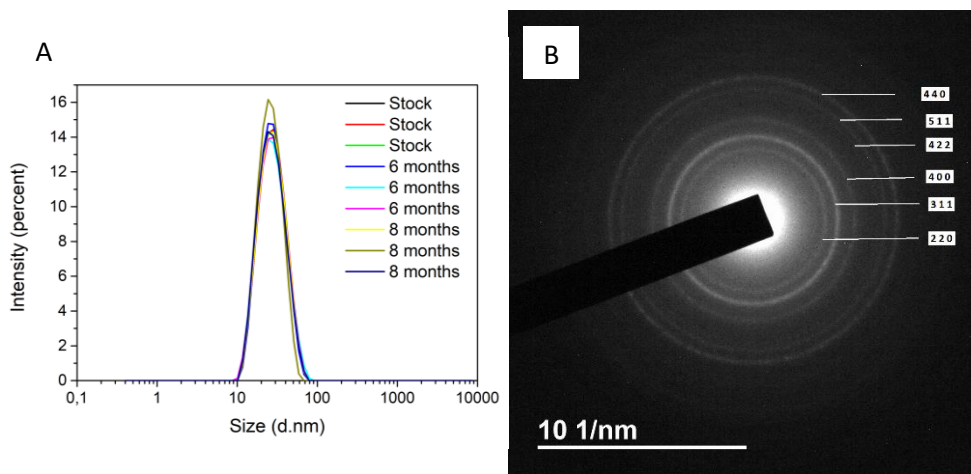


**Figure 5:** (A) Intensity-weighted hydrodynamic size distributions of the ferrofluid over time. Each measurement was repeated three times. (B) SAED image of oleate-coated USPIOs taken 8 months after the preparation of the ferrofluid, showing the diffraction rings of magnetite (JCPDS file no. 19-0629).

The hydrophobicity of the oleate-coated SPIONs is not compatible with most biomedical applications, thus a water-phase transfer was conducted in order to obtain nanoparticles colloiddally stable in aqueous solutions. We employed a water-phase transfer strategy based on the use of a secondary alkylammonium salt surfactant. The hydrophobic tail of the surfactant intercalates between the oleic acid molecules through hydrophobic Van der Waals interactions, leading to the formation of a hybrid bilayer around the magnetic nanoparticles as shown in Figure 6.A.<sup>28,29</sup> In a typical procedure, an aqueous solution of cetyltrimethylammonium bromide (CTAB) was mixed with the ferrofluid using a probe sonicator. The resulting oil-in-water microemulsion was heated at 65 °C under continuous stirring in order to evaporate the chloroform. In contrast to the oleate-coated nanoparticles, the resulting CTAB-stabilized USPIOs are highly stable in water, as shown in Figure 6.B.



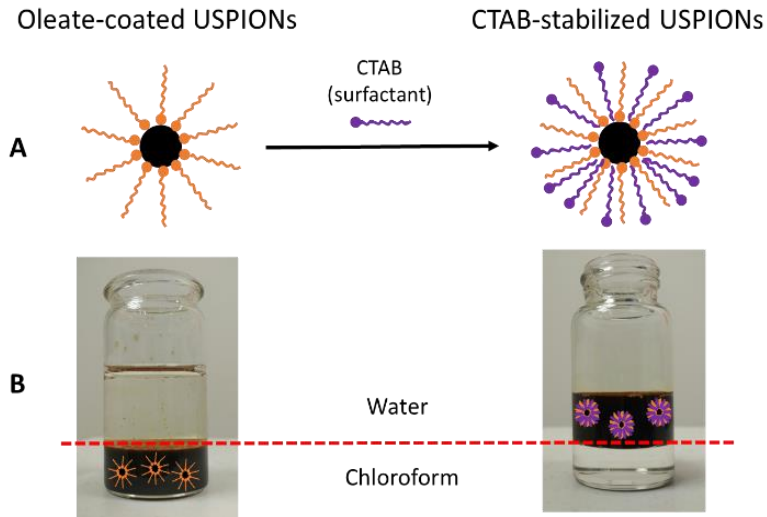


**Figure 6:** (A) Interaction of CTAB with oleate molecules on the surface of USPIOs and (B) USPIOs suspended in a mixture of water-chloroform before and after the water-phase transfer.

### 3.3.2.3. Magnetic characterization

It is well known that below a critical nanoparticle size, the magnetic moments of all the atoms within the nanoparticle tend to align in the same direction, forming a single magnetic domain.<sup>30</sup> These single-domain nanoparticles behave like small permanent magnets and therefore their magnetic moments will interact with each other and with any external magnetic field. However, if single-domain nanoparticles are small enough, their individual magnetic moments will be randomized by thermal energy, leading to a system with no net magnetization.<sup>11</sup> This unique phenomenon is known as superparamagnetism.<sup>31</sup> Thus, in the absence of an external magnetic field, the system presents no net magnetization. When an external magnetic field is applied, the individual magnetic moments of each nanoparticle align with the field and the system becomes rapidly magnetized, reaching the saturation magnetization (Figure 7.A). After removal of the magnetic field, the magnetic moment of the nanoparticles returns to a

random distribution and the material is quickly demagnetized, a very attractive property for biomedical applications.

The magnetic properties of the obtained CTAB-stabilized USPIOs was thoroughly investigated. For field-dependent magnetization experiments, the nanoparticles were dispersed in water and kept frozen at 250 K in order to prevent nanoparticle agglomeration, which could lead to misleading results. The magnetization curves showed a small hysteresis together with negligible remanence and coercivity, confirming the superparamagnetic behaviour of the obtained nanoparticles (Figure 7.B). The nanoparticles presented high saturation magnetization ( $M_s=74$  emu/g), close to the  $M_s$  value of bulk  $\text{Fe}_3\text{O}_4$  (92 emu/g).<sup>32</sup> This reduced magnetization compared to the bulk state is commonly observed in small ferrite nanoparticles,<sup>30,33</sup> being generally attributed to a phenomenon known as spin canting. Spin canting was first described as a non-uniform distribution of spins, which implies that the spins of the atoms within the nanoparticle are not completely aligned.<sup>34</sup> This distortion of spin alignment is expected to be more pronounced at the surface of nanoparticles, leading to a higher reduction of saturation magnetization in smaller nanoparticles (high surface-to-volume-ratio).<sup>35</sup> Additionally, it has been observed that the organic coating commonly used in the synthesis of iron oxide nanoparticles can induce the appearance of spin canting effects and a reduction of saturation magnetization.<sup>36</sup> However, internal structural disorder has also been suggested as a source of spin canting and cannot be excluded.<sup>37</sup> Finally, zero-field cooled/field cooled (ZFC/FC) magnetization curves revealed that the CTAB-stabilized USPIOs exhibit a superparamagnetic behaviour above 100 K (Figure 7.C).

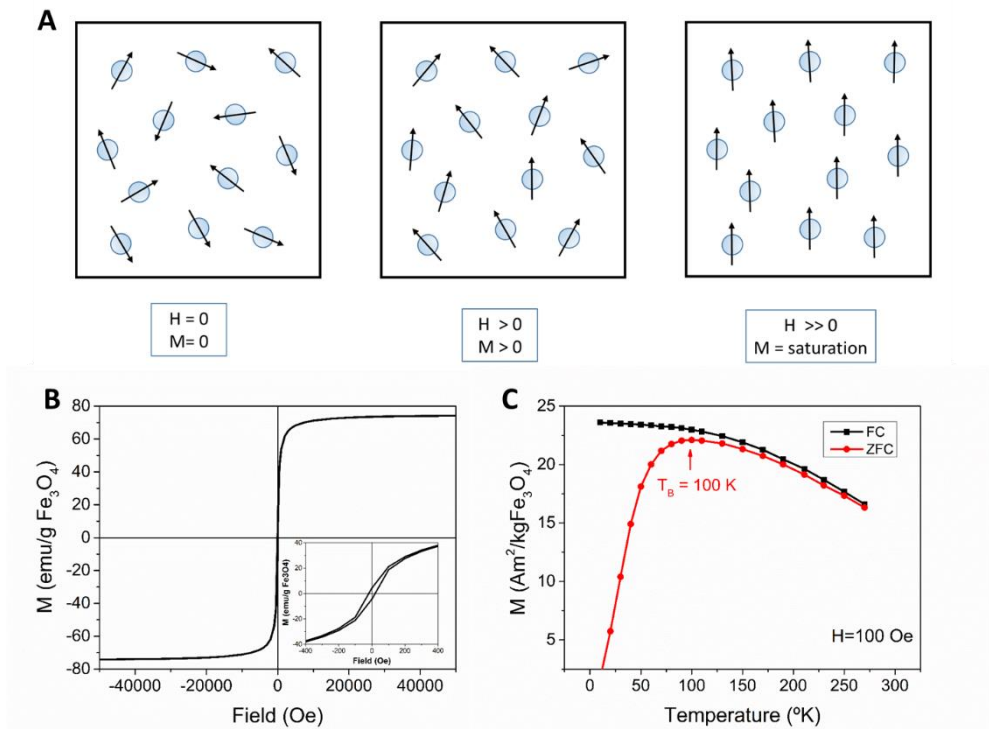


**Figure 7:** (A) Alignment of individual nanoparticle magnetic moments upon the application of an external magnetic field; (B) Field-dependent magnetization curves of CTAB-stabilized USPIOs at 250 K and (C) ZFC/FC curves measured at 100 Oe.

## 3.4. Applications

### 3.4.1. Magnetic Hyperthermia

The generation of heat produced by single-domain magnetic nanoparticles under the influence of an alternating magnetic field (AMF) can be explained by two mechanisms: Néel and Brownian relaxation. The first process is related to the rearrangement of the spins of the atoms in the nanoparticle, which orientate towards the same direction of the external magnetic field.<sup>38</sup> On the other hand, the external magnetic field can induce a physical rotation of the nanoparticle itself in a process known as Brownian relaxation. Although both relaxation processes occur simultaneously, the relative contribution of each of them depends on the hydrodynamic properties of both the nanoparticles and the medium where they are dispersed.<sup>39</sup> The heat losses produced by these relaxation mechanisms can be determined experimentally by measuring the temperature change produced by magnetic nanoparticles under the effect of an AMF.

Calorimetric experiments were conducted using a custom-made magnetic inductor that generates a stable magnetic field of 15.92 mT at 200 kHz. The strength and frequency of the magnetic field were chosen in order to meet the criteria for safe clinical applications, in which the product  $H \cdot f$  should be below the threshold value of  $5.0 \times 10^9 \text{ A m}^{-1}\text{s}^{-1}$ .<sup>40</sup> A refrigerated copper induction coil was used to prevent the transfer of heat from the inductor to the sample, which was placed at the center of the coil inside an insulating holder (Figure 8). The sample and coil were placed inside a thermostatic chamber, in which the temperature could be adjusted to simulate the body temperature and to control the initial temperature of each experiment.

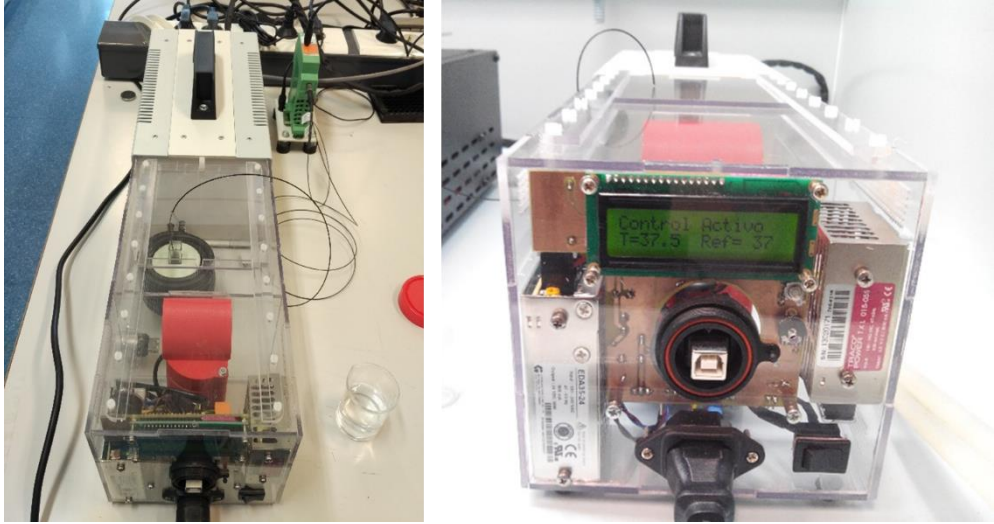


**Figure 8:** Experimental setup for hyperthermia calorimetric experiments (left). Both the sample and the magnetic induction coil were placed inside a thermostatic chamber with an automated temperature regulator (right).

Three samples (denoted as *a*, *b* and *c*) of increasing concentrations of nanoparticles (3.8, 5.7 and 7.6 mg/ml respectively) were measured in the custom-made magnetic inductor. The samples were pre-heated to 37 °C before the application of the AMF and the temperature of the liquid circulating inside the coil inductor was also set to 37 °C. The AMF was applied for 20 min to each sample, recording the increase of temperature every 10 seconds. As can be seen in Figure 9, a steady increase of temperature was registered in all cases, indicating that the colloid suspensions are stable under the experimental conditions applied. The increase of temperature was directly proportional to the concentration of magnetic nanoparticles, reaching temperatures within the mild hyperthermia regime. Only the sample with a higher concentration of nanoparticles (sample *c*) reached temperatures above 46 °C after 20 minutes of AMF induction. It is important to note that the concentration of nanoparticles in all the samples is below the common concentration of magnetic nanoparticles used for intratumoral injections (10 mg/ml).<sup>41</sup> Finally, the change of temperature in a control water sample under 20 minutes of induction was below 1 degree, which indicates

that the increase of temperature is mainly produced by the magnetic nanoparticles.

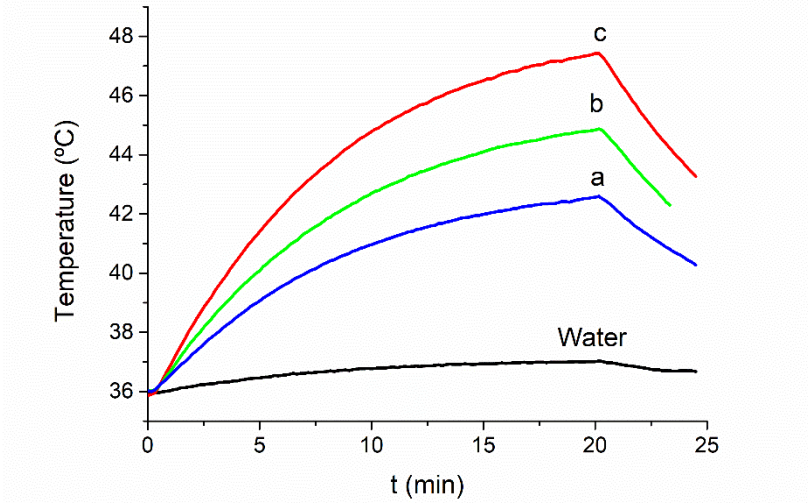


**Figure 9:** Heating curves of samples *a*, *b* and *c* (3.8, 5.7 and 7.6 mg NPs/ml respectively) after 20 minutes of AMF induction ( $H=15.72$  mT,  $f=200$  kHz). Water was used as control.

The specific absorption rate (SAR, in W/g) is the preferred parameter used to measure the heating efficiency of magnetic nanoparticles and can be calculated using the following equation:<sup>42</sup>

$$SAR = C_f \frac{m_f}{m_{NPs}} \cdot \frac{dT}{dt} \quad (5)$$

where  $m_f$  represents the mass of the tested ferrofluid,  $m_{NPs}$  corresponds to the mass of magnetic nanoparticles and  $dT/dt$  represents the rate of temperature increase.  $C_f$  is the heat capacity of the ferrofluid, which can be assumed equal to that of water ( $4.18 \text{ J g}^{-1} \text{ K}^{-1}$ ) when the amount of nanoparticles in the colloid is small compared to the amount of fluid.

The heat losses of magnetic nanoparticles increase with the frequency ( $f$ ) and the strength of the magnetic field ( $H$ ).<sup>43</sup> In order to better compare the heating efficiency of magnetic nanoparticles in different experimental setups, an additional parameter known as intrinsic loss power (ILP) is commonly used:<sup>44</sup>

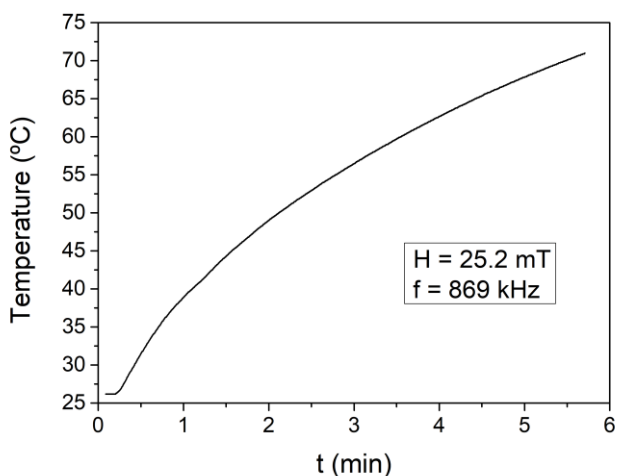
$$ILP = \frac{SAR}{fH^2} \quad (6)$$

SAR and ILP values of the synthesised nanoparticles were determined using equation 5 and 6. The rate of temperature increase was obtained from the heating curves at the initial time, since the temperature response is not linear in non-adiabatic systems due to heat losses to the environment.<sup>45</sup> For comparison purposes, the SAR and ILP values are referred to the mass of magnetite ( $\text{Fe}_3\text{O}_4$ ) in each sample, which was determined using atomic absorption spectroscopy (AAS). Calculated SAR and ILP values are presented in Table 1. The obtained values for samples *a*, *b* and *c* are very similar independently of the concentration of nanoparticles, as expected for experiments conducted at the same frequency and field strength.<sup>46</sup> These results also indicate that the nanoparticles are highly stable under the effect of an external magnetic field, since the appearance of agglomeration would have resulted in varying SAR and ILP values.<sup>17</sup>

In order to validate the performance of the custom-made magnetic inductor, a fourth sample (sample *d*) with a concentration of  $\text{Fe}_3\text{O}_4$  similar to sample *a*, was measured in a commercial magnetic hyperthermia equipment. The SAR and ILP values obtained in the commercial equipment at 15 mT and 268 kHz are comparable to those obtained in the custom-made magnetic inductor, validating its applicability for hyperthermia experiments. Finally, the heating efficiency of sample *d* was evaluated using the highest field and frequency available in the commercial equipment ( $H = 25.2$  mT and  $f = 869$  kHz). A rapid increase of temperature was registered in the sample, which reached 70 °C within 5 minutes of AMF induction (Figure 10). Accordingly, a significantly higher SAR value was obtained (323.22 W/g), demonstrating the great heating potential of the developed USPIOs at high fields and frequencies.

**Table 1** Tested samples, experimental conditions applied (H and f) and calculated values of SAR and ILP (referred to the mass of magnetite in each sample).

Sample	a	b	c	d
[NPs] (mg/ml)	3.8	5.7	7.6	4.5
[Fe <sub>3</sub> O <sub>4</sub> ] (mg/ml)	3.04	4.56	6.08	3.55
H (mT)	15.92	15.92	15.92	15.00
f (kHz)	200	200	200	268
SAR (W/g)	17.90	17.45	17.22	18.58
ILP (nH m <sup>2</sup> /kg)	0.55	0.54	0.53	0.48

**Figure 10:** Heating curve of sample d (4.5 mg NPs/ml) measured in the commercial hyperthermia equipment at H=25.2 mT and f=869 kHz.

### 3.4.2. Relaxivity measurements

MRI contrast agents are able to reduce the longitudinal and transverse relaxation times ( $T_1$  and  $T_2$ ) of surrounding water protons under the influence of an external magnetic field. Relaxation rates are defined as the inverse of relaxation times ( $R_i = 1/T_i$ ), thus an effective MRI contrast agent will produce an increase of water relaxation rates. However, this effect depends on the concentration of contrast agent and an additional parameter is needed in order to compare the efficiency of different MRI contrast agents.



Longitudinal and transverse relaxivities,  $r_1$  and  $r_2$ , are defined as the change of water relaxation rates normalized to the concentration of contrast agent,<sup>47</sup> in this case the concentration of iron expressed in mM:

$$r_{1,2} = \frac{\Delta R_{1,2}}{[Fe]} \quad (7)$$

Contrast agent relaxivities are also affected by the strength of the applied magnetic field. Although the use of ultra-high field MRI (7.0 T or higher) is slowly becoming a reality for clinical applications,<sup>48</sup> standard clinical MRI scanners still operate at low and intermediate field strengths (from 0.5 T to 3.0 T).  $T_1$  and  $T_2$  water relaxation times in the presence and absence of the CTAB-stabilized USPIOs were measured using a 1.4 T relaxometer and a preclinical MRI scan working at 3.0 T. Relaxations rates ( $R_1$  and  $R_2$ ) were plotted against the concentration of Fe, and relaxivities were obtained from the slope of the resulting curve as shown in Figure 11. The longitudinal and transverse relaxivities obtained at 1.4 T and 3.0 T along with the corresponding  $r_2/r_1$  ratios are presented in Table 2.

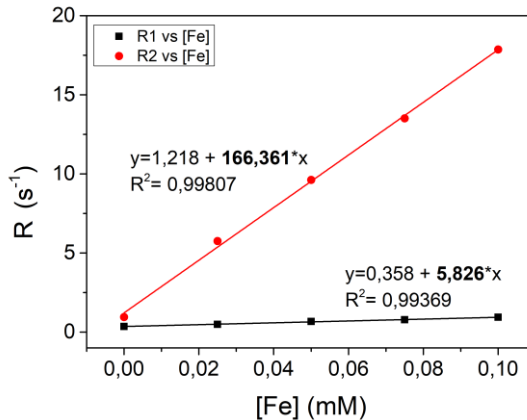


**Figure 11:** Dependence of longitudinal ( $R_1$ ) and transverse ( $R_2$ ) relaxation rates with the concentration of Fe.

**Table 2** Experimental relaxivity values obtained at 1.4 and 3.0 T, together with reported relaxivities for the commercial formulations Feraheme® and Combidex®.<sup>21</sup>

Sample	Field (T)	$r_1$ (mM <sup>-1</sup> s <sup>-1</sup> )	$r_2$ (mM <sup>-1</sup> s <sup>-1</sup> )	$r_2/r_1$
USPIONS	1.4	20.5	157	7.7
USPIONS	3.0	5.8	166	28.6
Feraheme®	1.5	15.0 <sup>a</sup>	89 <sup>a</sup>	5.9
Combidex®	1.5	9.9 <sup>a</sup>	65 <sup>a</sup>	6.6

<sup>a</sup>Values reported at 1.5T and 37 °C

The nanoparticles presented relatively high  $r_2$  relaxivity at the two working fields tested. The obtained  $r_2$  values are similar, consistent with the magnetic saturation exhibited by the nanoparticles above 1.0 T (see Figure 7.B). Impressively, the nanoparticles also showed a considerably high  $r_1$  relaxivity at 1.4 T (20.5 s<sup>-1</sup>mM<sup>-1</sup>), whereas a lower value was obtained at 3.0 T (5.8 s<sup>-1</sup>mM<sup>-1</sup>). The field dependence of longitudinal relaxation is complex due to the contribution of different mechanisms,<sup>29</sup> but in the case of iron oxide nanoparticles a reduction of  $r_1$  relaxivity is usually observed when the magnetic field is increased.<sup>49,50</sup>

Contrast agents are commonly classified based on their  $r_2/r_1$  ratio. A high  $r_2/r_1$  value indicates a dominant  $T_2$  effect and dark contrast will be obtained in  $T_2$ -weighted images. On the other hand, materials with a high  $r_1$  relaxivity and a relatively low  $r_2/r_1$  (~1) will be efficient  $T_1$  contrast agents.<sup>51</sup> At low fields, our USPIONS showed an intermediate  $r_2/r_1$  value of 7.7, characteristic of  $T_1/T_2$  dual contrast agents.<sup>51,52</sup> When the field was increased to 3.0 T, a higher  $r_2/r_1$  value was obtained due to the reduction of  $r_1$ . However, the dual behavior of the nanoparticles was still evident, as demonstrated by the images obtained in the preclinical MRI scan (Figure 12). When fast spin echo (FSE)  $T_2$ -weighted sequences were applied, a negative contrast was observed. However, upon the application of  $T_1$ -weighted sequences, the characteristic bright contrast produced by  $T_1$  agents was detected.

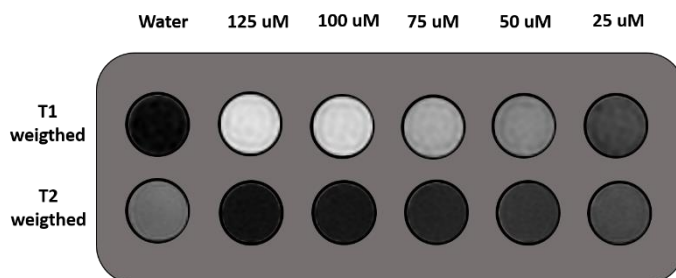


**Figure 12:** *T1* and *T2*-weighted images showing the dual behavior of CTAB-stabilized USPIOs. Measurements were conducted at 3.0 T.

As shown in Table 2,  $r1$  and  $r2$  relaxivity values at 1.4 T are higher than those reported for the USPIOs formulation Combidex<sup>®</sup>, currently under clinical development in Europe for the detection of lymph node metastases,<sup>53</sup> or the values obtained for the FDA-approved supplement Feraheme<sup>®</sup>. Interestingly, relaxivities are also higher than those reported for USPIOs synthesized using more complex high-temperature procedures,<sup>12,54</sup> and are even comparable to those reported for sophisticated hybrid nanodevices that combine different types of *T1* and *T2* contrast materials.<sup>55,56</sup> A balanced distribution of nanoparticle sizes ranging from 4 nm to 26 nm but with an average nanoparticle size of 10.3 nm, could be responsible for the good performance of the obtained USPIOs as dual *T1/T2* contrast agents.

### 3.5. Conclusions

In this work, highly-stable USPIONS were prepared through a one-step coprecipitation method. With this simple methodology, gram-scale quantities of nanoparticles were obtained using mild reaction conditions, in contrast to other sophisticated strategies that require the use of organic solvents and high reaction temperatures. The obtained nanoparticles are coated with a highly-packed monolayer of oleate molecules, which provides increased dispersibility in organic solvents and long-term stability. They can be readily transferred to water using CTAB, although it would be desirable to explore alternative phase-transfer agents for future biomedical applications. The developed USPIONS are superparamagnetic at room temperature and show high saturation magnetization close to that of the bulk material. These two features contribute to their improved heating efficiency, which proved successful in generating temperatures within the mild hyperthermia regime. The effect of the nanoparticles on water relaxation rates was also evaluated, showing  $r_1$  and  $r_2$  relaxivities higher than those reported for clinically used MRI contrast agents. Overall, the developed USPIONS appear as a versatile system that combines both magnetic hyperthermia and dual  $T_1/T_2$  MRI capabilities with great potential for the development of new theranostic nanodevices.

### 3.6. References

- (1) J.-H. Lee, J. Jang, J. Choi, S. H. Moon, S. Noh, J. Kim, J.-G. Kim, I.-S. Kim, K. I. Park and J. Cheon, *Nat. Nanotechnol.*, **2011**, 6, 418–422.
- (2) A. K. Hauser, R. J. Wydra, N. A. Stocke, W. Anderson and J. Z. Hilt, *J. Control. Release*, **2015**, 219, 76–94.
- (3) J. M. Chem, B. Gonz, E. Ruiz-Hernández, C. Ram and T. Portol, *J. Mater. Chem.*, **2011**, 21, 4598–4604.
- (4) J. Gallo, N. J. Long and E. O. Aboagye, *Chem. Soc. Rev.*, **2013**, 42, 7816–33.
- (5) C. Boyer, M. R. Whittaker, V. Bulmus, J. Liu and T. P. Davis, *NPG Asia Mater.*, **2010**, 2, 23–30.
- (6) Y.-X. J. Wang, *Quant. Imaging Med. Surg.*, **2011**, 1, 35–40.
- (7) Y. X. J. Wáng and J.-M. Idée, *Quant. Imaging Med. Surg.*, **2017**, 7, 88–122.
- (8) C. Blanco-Andujar, A. Walter, G. Cotin, C. Bordeianu, D. Mertz, D. Felder-Flesch and S. Begin-Colin, *Nanomedicine*, **2016**, 11, 1889–1910.
- (9) T. Shin, Y. Choi, S. Kim and J. Cheon, *Chem. Soc. Rev.*, 2015, 44, 4501–4516.
- (10) M. A. Busquets, J. Estelrich and M. J. Sánchez-Martín, *Int. J. Nanomedicine*, **2015**, 10, 1727–1741.
- (11) N. Lee and T. Hyeon, *Chem. Soc. Rev.*, **2012**, 41, 2575–2589.
- (12) G. Wang, X. Zhang, A. Skallberg, Y. Liu, Z. Hu, X. Mei and K. Uvdal, *Nanoscale*, **2014**, 6, 2953.
- (13) B. H. Kim, N. Lee, H. Kim, K. An, Y. Il Park, Y. Choi, K. Shin, Y. Lee, S. G. Kwon, H. Bin Na, J. G. Park, T. Y. Ahn, Y. W. Kim, W. K. Moon, S. H. Choi and T. Hyeon, *J. Am. Chem. Soc.*, **2011**, 133, 12624–12631.
- (14) A. H. Negussie, P. S. Yarmolenko, A. Partanen, A. Ranjan, G. Jacobs, D. Woods, H. Bryant, D. Thomasson, M. W. Dewhurst, B. J. Wood and M. R. Dreher, *Int. J. Hyperthermia*, **2011**, 27, 140–55.
- (15) A. Hervault and N. Thi Kim Thanh, *Nanoscale*, **2014**, 6, 11553–11573.
- (16) C. S. S. R. Kumar and F. Mohammad, *Adv. Drug Deliv. Rev.*, **2011**, 63, 789–808.
- (17) A. E. Deatsch and B. a. Evans, *J. Magn. Magn. Mater.*, **2014**, 354, 163–172.
- (18) J. Zhang, X. Li, J. M. Rosenholm and H. Gu, *J. Colloid Interface Sci.*, **2011**, 361, 16–24.
- (19) C. Corot, P. Robert, J. M. Idée and M. Port, *Adv. Drug Deliv. Rev.*, **2006**, 58, 1471–1504.
- (20) M. Gonzales, L. M. Mitsumori, J. V. Kushleika, M. E. Rosenfeld and K. M. Krishnan, *Contrast Media Mol. Imaging*, **2010**, 5, 286–293.
- (21) S. Laurent, D. Forge, M. Port, A. Roch, C. Robic, L. Vander Elst and R. N. Muller, *Chem. Rev.*, **2008**, 108, 2064–110.
- (22) L. B. Kiss, J. Söderlund, G. A. Niklasson and C. G. Granqvist, *Nanotechnology*, **1999**, 10, 25–28.

- (23) H. E. Swanson, H. F. McMurdie, M. C. Morris and E. H. Evans, *Natl. Bur. Stand.*, **1967**, 25, 31.
- (24) R. De Palma, S. Peeters, M. J. Van Bael, H. Van Den Rul, K. Bonroy, W. Laureyn, J. Mullens, G. Borghs and G. Maes, *Chem. Mater.*, **2007**, 19, 1821–1831.
- (25) P. Roonasi and A. Holmgren, *Appl. Surf. Sci.*, **2009**, 255, 5891–5895.
- (26) K. Yan, H. Li, X. Wang, C. Yi, Q. Zhang, Z. Xu, H. Xu and A. K. Whittaker, *J. Mater. Chem. B*, **2014**, 2, 546–555.
- (27) E. R. Garland, E. P. Rosen, L. I. Clarke and T. Baer, *Phys. Chem. Chem. Phys.*, **2008**, 10, 3156.
- (28) H. Fan, K. Yang, D. M. Boye, T. Sigmon, K. J. Malloy, H. Xu, G. P. López and C. J. Brinker, *Sci. Reports*, **2004**, 304, 567–571.
- (29) E. D. Smolensky, H. Y. E. Park, Y. Zhou, G. A. Rolla, M. Marjańska, M. Botta and V. C. Pierre, *J. Mater. Chem. B*, **2013**, 1, 2818–2828.
- (30) R. H. Kodama, *J. Magn. Magn. Mater.*, **1999**, 200, 359–372.
- (31) C. P. Bean and J. D. Livingston, *J. Appl. Phys.*, **1959**, 30, S120–S129.
- (32) Q. Li, C. W. Kartikowati, S. Horie, T. Ogi, T. Iwaki and K. Okuyama, *Sci. Rep.*, **2017**, 7, 9894.
- (33) A. G. Roca, M. P. Morales, K. O’Grady and C. J. Serna, *Nanotechnology*, **2006**, 17, 2783–2788.
- (34) J. M. D. Coey, *Phys. Rev. Lett.*, **1971**, 27, 1140–1142.
- (35) S. Linderoth, P. V. Hendriksen, F. Bødker, S. Wells, K. Davies, S. W. Charles and S. Mørup, *J. Appl. Phys.*, **1994**, 75, 6583–6585.
- (36) T. J. Daou, J. M. Grenèche, G. Pourroy, S. Buathong, A. Derory, C. Ulhaq-Bouillet, B. Donnio, D. Guillon and S. Begin-Colin, *Chem. Mater.*, **2008**, 20, 5869–5875.
- (37) C. J. Serna, F. Bødker, S. Mørup, M. P. Morales, F. Sandiumenge and S. Veintemillas-Verdaguer, *Solid State Commun.*, **2001**, 118, 437–440.
- (38) S. Laurent, S. Dutz, U. O. Häfeli and M. Mahmoudi, *Adv. Colloid Interface Sci.*, **2011**, 166, 8–23.
- (39) N. T. Thanh, *Magnetic Nanoparticles From Fabrication to Clinical Applications*, CRC Press, Boca Raton, **2012**.
- (40) R. Hergt and S. Dutz, *J. Magn. Magn. Mater.*, 2007, 311, 187–192.
- (41) R. Hergt, S. Dutz, R. Müller and M. Zeisberger, *J. Phys. Condens. Matter*, **2006**, 18, S2919–S2934.
- (42) D.-H. K. D.-H. Kim, Y. T. Thai, D. E. Nikles and C. S. Brazel, *IEEE Trans. Magn.*, **2009**, 45, 64–70.
- (43) R. E. E. Rosensweig, *J. Magn. Magn. Mater.*, **2002**, 252, 370–374.
- (44) D. Ortega and Q. A. Pankhurst, in *Nanoscience: Volume 1: Nanostructures through Chemistry*, ed. P. O’Brien, The Royal Society of Chemistry, Cambridge, **2013**, vol. 1, pp. 60–88.

- 
- (45) R. R. Wildeboer, P. Southern and Q. A. Pankhurst, *J. Phys. D. Appl. Phys.*, **2014**, 47, 495003.
- (46) C. Guibert, V. Dupuis, V. Peyre and J. Fresnais, *J. Phys. Chem. C*, **2015**, 119, 28148–28154.
- (47) C. Henoumont, S. Laurent and L. Vander Elst, *Contrast Media Mol. Imaging*, **2009**, 4, 312–321.
- (48) T. N. Parac-Vogt, S. Biju, J. Gallo, M. Bañobre-López, B. Manshian, S. Soenen, U. Himmelreich and L. Vander Elst, *Chem. Eur. J.*, **2018**, 24, 7388–7397.
- (49) M. Rohrer, H. Bauer, J. Mintorovitch, M. Requardt and H. J. Weinmann, *Invest. Radiol.*, **2005**, 40, 715–724.
- (50) Y. Gossuin, P. Gillis, A. Hocq, Q. L. Vuong and A. Roch, *Wiley Interdiscip. Rev. Nanomedicine Nanobiotechnology*, **2009**, 1, 299–310.
- (51) N. Guldris, B. Argibay, Y. V. Kolen'ko, E. Carbó-Argibay, T. Sobrino, F. Campos, L. M. Salonen, M. Bañobre-López, J. Castillo and J. Rivas, *J. Colloid Interface Sci.*, **2016**, 472, 229–236.
- (52) F. Hu and Y. S. Zhao, *Nanoscale*, **2012**, 4, 6235–43.
- (53) H. E. Daldrup-Link, *Radiology*, **2017**, 284, 616–629.
- (54) F. Hu, Q. Jia, Y. Li and M. Gao, *Nanotechnology*, **2011**, 22, 245604.
- (55) T. Tegafaw, W. Xu, M. W. Ahmad, J. S. Baeck, Y. Chang, J. E. Bae, K. S. Chae, T. J. Kim and G. H. Lee, *Nanotechnology*, **2015**, 26, 365102.
- (56) G. H. Im, S. M. Kim, D. G. Lee, W. J. Lee, J. H. Lee and I. S. Lee, *Biomaterials*, **2013**, 34, 2069–2076.





## **Chapter 4:**

***Design of an optimized synthetic protocol for the preparation of monodisperse core-shell magnetic mesoporous silica nanoparticles***



## 4.1. Introduction

### 4.1.1. Surfactant-templated mesoporous silica materials

According to the IUPAC, porous materials can be classified into three different categories, as shown in Figure 1. Microporous materials are those with pore sizes below 2 nm, mesoporous materials present pore sizes between 2 and 50 nm and macroporous materials present pores with diameters above 50 nm.<sup>1</sup> In the context of this PhD project, we are focusing on materials with pore sizes in the mesopore range.

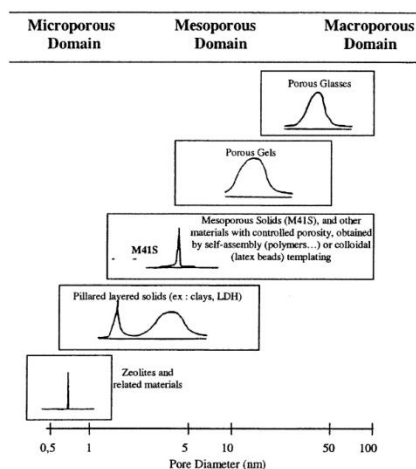


**Figure 1:** Examples of micro-, meso-, and macroporous materials, showing pore size domains and typical pore size distribution. *Reprinted with permission from Chem. Rev. 102, 4093–4138 (2002).*

In the early 1990s, Mobil scientists reported the synthesis of a new type of mesoporous silica materials known as the M41S family.<sup>2,3</sup> These materials presented long-range order and uniformly-sized pores, comparable to those reported for zeolitic materials. However, unlike microporous zeolites, the pore size of these new materials could be tailored within the mesopore range.

The key to obtain this highly-ordered mesoporous materials was to catalyse the condensation of silica in the presence of a surfactant, which acted as a template for the formation of the mesoporous silica framework.<sup>2,3</sup> Interestingly, surfactants had already been used in the 1970s for the synthesis of “low-density silica”, a material that happened to be identical to one of the M41S materials reported 20 years later.<sup>4</sup>

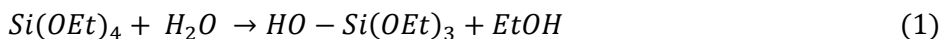
However, it was the discovery of the M41S materials that popularized the synthesis of surfactant-templated materials, leading to an exponential increase of publications related to this area.<sup>5</sup>

#### 4.1.1.1. Synthesis of mesoporous silica materials

The synthesis of mesoporous silica materials requires four basic reagents: a silica source, a catalyst for the condensation of silica, a surfactant template and the solvent. The synthesis of the core-shell M-MSNs presented in this project are conducted in water using ammonia as a catalyst. Tetraethyl orthosilicate (TEOS) is used as the silica source, whereas the cationic surfactant hexadecyltrimethylammonium bromide (CTAB) was selected as a template. A brief description about these two reagents is presented in this section in order to understand their role in the synthesis of mesoporous silica materials.

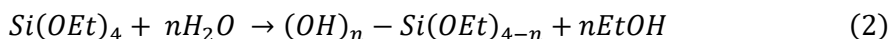
- Silica source

TEOS is a silicon alkoxide commonly used as a silica precursor since it is rapidly hydrolyzed in water. The reaction of hydrolysis involves the replacement of an alkoxide group by a hydroxyl group according to the following reaction:



Depending on the amount of water and the presence of a catalyst, TEOS can be partially or completely hydrolyzed:

- *Partial hydrolysis of TEOS ( $n < 4$ ):*

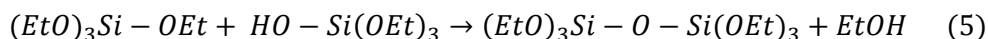
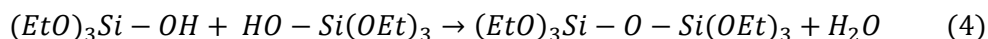


- *Complete hydrolysis of TEOS:*



The complete hydrolysis of TEOS generates monomeric orthosilicic acid,  $Si(OH)_4$ , the smallest water-soluble form of silica ( $SiO_2$ ). Silicic acid is a highly reactive molecule that rapidly condenses to form a wide variety of oligomers and polymers, so it can only be detected in water at very low concentrations. In fact, it was not until 2017 that orthosilicic acid could be isolated and its crystallographic structure determined using a non-aqueous selective synthesis.<sup>6</sup>

After hydrolysis is initiated, the condensation between (partially or completely) hydrolysed species leads to the formation of siloxane bonds (Si-O-Si). Depending on which is the leaving group during the condensation reaction, water or ethanol will be generated as by-products:



Each silica monomer can form up to 4 siloxane bonds through successive condensation reactions, leading to the formation of linear, cyclic and polycyclic oligomers.<sup>7,8</sup> Silica can also form 3-dimensional structures in which each silicon atom is bound to 4 oxygens, configuring a tetrahedral  $[SiO_4]^{4-}$  unit that represents the basic building block of silica materials.<sup>9</sup> In crystalline silica materials, the  $[SiO_4]^{4-}$  units are perfectly packed forming a periodic pattern, as shown in Figure 2.A. Crystalline silica is found in nature in different polymorphic forms such as quartz, tridymite and cristobalite. In the case of amorphous silica materials, the repeating  $[SiO_4]^{4-}$  unit is randomly distributed forming a non-periodic 3-dimensional structure, as shown in Figure 2.B. Surfactant-templated mesoporous silica materials belong to this class of amorphous silica, *i.e.* they do not present ordered structures at the atomic level. However, order can be found at the mesoscale level as a result of the periodic arrangement of mesoporous structures, hence their classification as ordered mesostructured materials.<sup>10</sup>

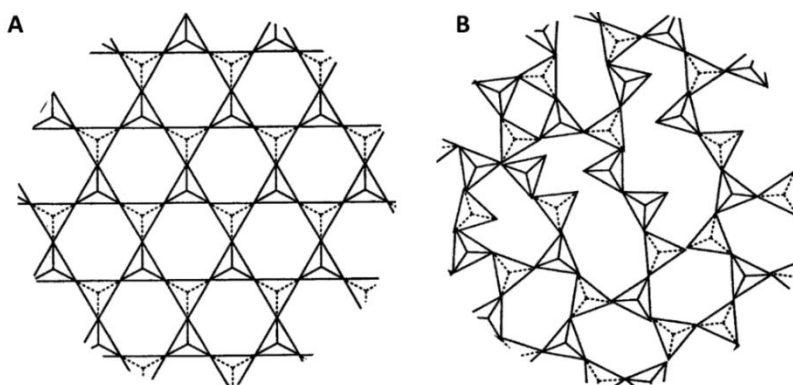


**Figure 2:** Two-dimensional representation of regular versus random packing of  $[SiO_4]^{4-}$  tetrahedral units in crystalline (A) and amorphous silica (B). Adapted from *Advances in Chemistry Series 234*, 19, (1994).

- Surfactant

Due to their amphiphilic nature, surfactants assemble in solution into different micellar and supramicellar structures, minimizing the contact of their hydrophobic tails with water. For a comprehensive analysis about the self-assembly of amphiphilic molecules see the monographic study by Israelachvili.<sup>11</sup>

Hexadecyltrimethylammonium bromide (CTAB) is a common cationic surfactant used in the synthesis of mesoporous silica materials. Figure 3 shows the phase diagram of CTAB in which liquid crystal phases with different geometries are formed under specific conditions.<sup>12</sup> Interestingly, it was found that M41S materials exhibited the same type of hexagonal, cubic and lamellar structures observed in pure surfactant solutions (Figure 4),<sup>13</sup> which suggested that surfactants had an important structure-directing role in the formation of mesoporous silica materials. This led to the proposal of a liquid crystal templating (LCT) mechanism in which surfactant supramolecular assemblies would act as a template for the condensation of the silica precursor, determining the geometry of the resulting porous silica framework.<sup>2,3</sup>

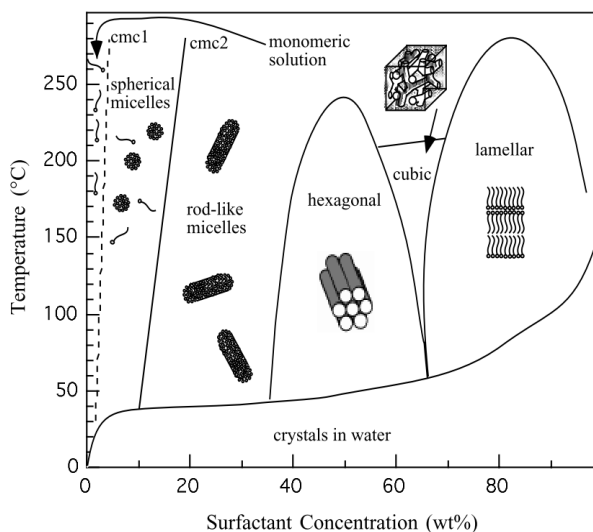


**Figure 3:** Phase diagram and schematics of the corresponding surfactant liquid crystal phases of the surfactant CTAB in water. CMC1 is the critical micelle concentration for the formation of spherical micelles, which has been exaggerated to higher concentrations for the purposes of the illustration. CMC2 is the critical micelle concentration for the formation of rod-like micelles. *Reprinted with permission from Chem. Mater. 10, 311–321 (1998).*

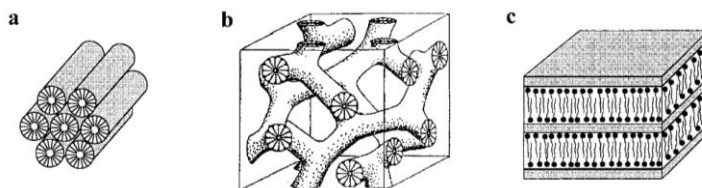


**Figure 4:** The three characteristic structures identified in the formation of M41S materials: (a) hexagonal; (b) cubic bicontinuous, Ia3d; and (c) lamellar. *Reprinted with permission from Chem. Mater.* 10, 311–321 (1998).

Mesoporous materials with different pore sizes could be prepared by using surfactants with hydrophobic chains of different lengths, which gave additional support to the theory of a surfactant templating mechanism.<sup>2,3</sup> Variation of other reactions parameters such as the silica precursor, surfactant/silica ratio, pH, temperature or the presence of co-solvents, were also found to influence the phase behaviour of the surfactant template and the corresponding mesoporous structure of the obtained materials.<sup>14,15</sup>

After the formation of the silica-surfactant mesophase, the organic template is removed in order to empty the mesoporous cavities. This is usually conducted by calcination of the material at temperatures between 500–600 °C, a temperature range at which the mesoporous structure of inorganic material matrixes is usually stable.<sup>16</sup> It is important to note that the application of heating treatments has an important effect on the degree of hydroxylation of the silica structure, inducing the condensation of silanol groups and the elimination of water.<sup>17</sup> In the case of organosilicas, *i.e.* silica materials that incorporate organic groups, an alternative method based on solvent extraction is used in order to remove the template while keeping the organic functionalities of the material.

### 4.1.2. Spherical mesoporous silica particles

Surfactant-templating resulted a successful strategy not only to control the properties of the mesostructure but also to control the morphology of the resulting mesoporous materials. Initially, M41S materials were prepared in the form of fine powders composed of particles of different shapes. However, it was found that variation of reaction conditions could lead to surfactant-templated materials with a whole range of well-defined particulate shapes, as shown in Figure 5.<sup>18</sup>

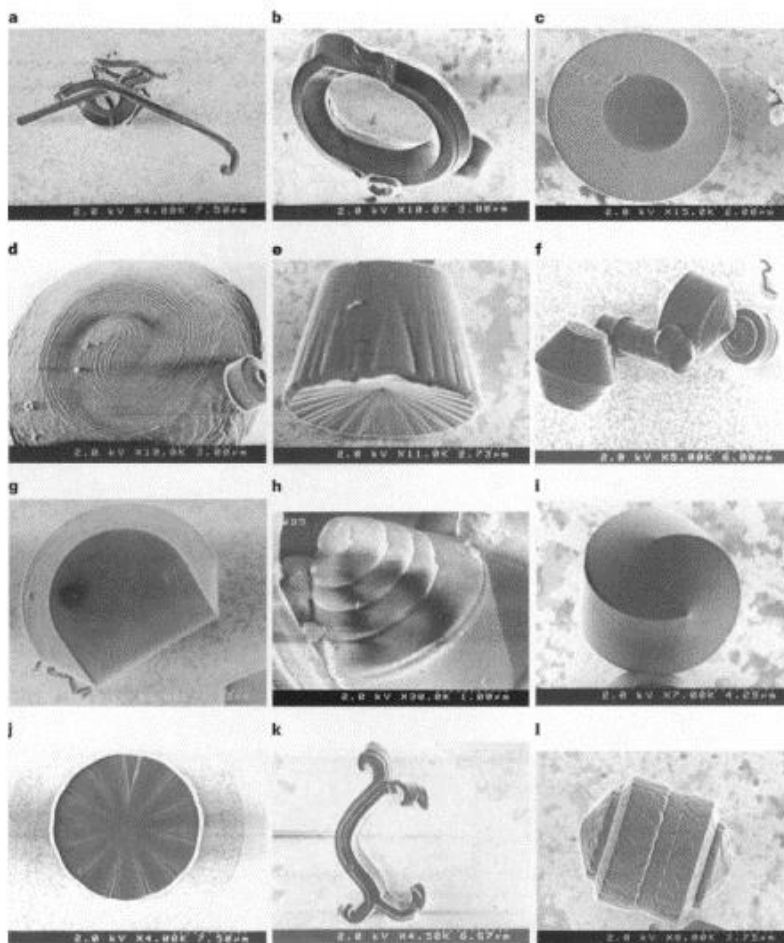


**Figure 5:** Examples of mesoporous silica particles with different shapes and surface patterns: (a) rope; (b) toroid; (c) discoid; (d) pinwheel; (e) wheel; (f) gyroid; (g) bagel; (h) shell; (i) knot; (j) clock; (k) eccentric 1; and (l) eccentric 2. Reprinted with permission from *Nature* 386, 692–695 (1997).



The synthesis of spherical mesoporous silica materials with uniform sizes was initially motivated due to their application as sorbents for chromatographic separation.<sup>19</sup> Some of the first attempts to prepare this type of particles were based on modifications of the famous Stober method. The Stober method was developed in the late 1960s for the synthesis of spherical nonporous silica particles with uniform sizes.<sup>20</sup> The synthesis is based on a sol-gel reaction in which tetraalkyl orthosilicate species are hydrolysed and condensed in an ethanolic/aqueous solution using ammonia as a catalyst.

Unger and co-workers were probably the first group to combine the Stober method with a surfactant templating approach, leading to the formation of spherical silica particles with a mesoporous structure (Figure 6.A).<sup>21–23</sup> The addition of a surfactant as a structure-directing agent provides control over the mesostructure whereas the incorporation of short-chain alcohols modulates the macroscopic morphology of the obtained particles (Figure 6.B).<sup>24</sup> Since then, similar variations of the Stober method have been successfully applied for the synthesis of spherical mesoporous silica particles.<sup>24–32</sup>

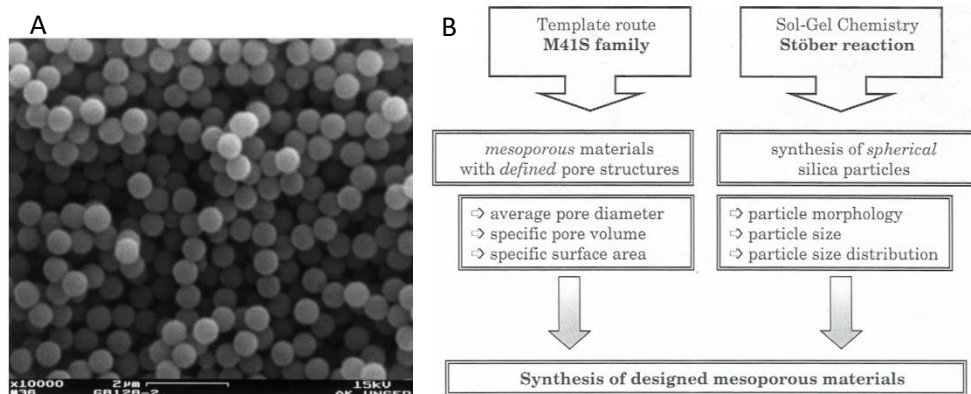


**Figure 6:** (A) SEM micrograph of spherical mesoporous silica nanoparticles and (B) synthetic strategy used to design spherical mesoporous particles with defined pore structures. Reprinted with permission from *Microporous Mesoporous Mater.* 27, 207–216 (1999) and from *Stud. Surf. Sci. Catal.* 128, 155–165 (2000).

## 4.1.2.1. Mesoporous silica nanoparticles (MSNs)

The works described above allowed the preparation of mesoporous silica spheres in the micrometer to sub-micrometer size range. However, the preparation of MSNs with sizes below 100 nm was especially appealing for the development of different technological and biomedical applications.<sup>33</sup> In the early 2000s, the groups of Cai, Mann and Ostafin independently developed synthetic strategies for the fabrication of MSNs, achieving a certain control over the size and shape of the final nanometer-sized particles, as shown in Figure 7.<sup>34–36</sup>

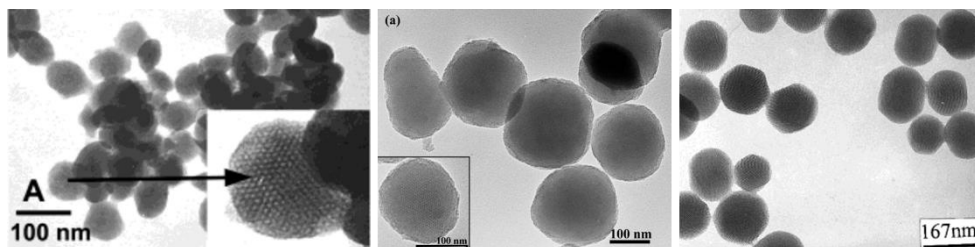


**Figure 7:** First examples of silica particles with ordered mesoporous interiors and sizes in the 100-200 nm range. Reprinted with permission from *Chem. Mater.* 13, 258–263 (2001), *J. Mater. Chem.* 13, 1023–1029 (2003) and *Chem. Mater.* 14, 4721–4728 (2002).

Cai and co-workers used high dilution conditions and explored the effect of the catalyst on the reaction.<sup>34</sup> Under their reaction conditions, sodium hydroxide yielded 70 nm spherical particles whereas the use of ammonia led to micrometer-sized hexagonal crystals or submicrometer-sized rods, depending on the dilution applied. Mann *et al.* used a different strategy based on two subsequent dilution/neutralization steps in order to obtain well-dispersed nanoparticles. By adjusting the delay between both processes, the size of the resulting MSNs was tuned between 20 and 100 nm.<sup>33</sup> Ostafin and co-workers tested a whole set of parameters such as the concentration of reagents, the presence of ethanol as a cosolvent, or the use of cationic vs neutral surfactants.<sup>36</sup> Their experiments showed that the initial amount of TEOS and CTAB had a major contribution on the size of the final MSNs, which was adjusted between 65 and 740 nm.

What these early works had in common was the use of high dilutions for the preparation of MSNs. However, they also revealed that the size and shape of the resulting nanoparticles was also highly influenced by other reaction parameters,

which should be accurately optimized in order to obtain monodisperse nanoparticles with uniform sizes.

#### 4.1.2.2. Core-shell MSNs

The search for new multi-functional nanodevices led to the combination of MSNs with other types of functional nanoparticles. The first examples consisted on gold, silver and metallic oxide nanoparticles which were embedded or directly grown within the cavities of the mesoporous silica structure.<sup>37-39</sup>

A more sophisticated approach involved the formation of MSNs in the presence of colloidal particles, leading to MSNs with a core-shell structure. Gold nanoparticles were one of the first colloidal suspensions to be investigated as cores for the preparation of core-shell MSNs.<sup>40,41</sup> A seeded-growth mechanism was proposed to explain the formation of this type of nanoparticles, in which the pre-formed colloidal particles would act as seeds for the growth of the mesoporous silica shell (see section 4.1.3. about formation mechanisms).

#### 4.1.2.3. Core-shell magnetic mesoporous silica nanoparticles (M-MSNs)

In 2008, Hyeon and co-workers used a similar seeded-growth strategy for the preparation of core-shell M-MSNs using  $\text{Fe}_3\text{O}_4$  nanoparticles as seeds.<sup>42</sup> This seminal work, presented the synthesis of monodisperse core-shell M-MSNs with a magnetic core composed of a single iron oxide crystal. More importantly, the size of the obtained nanoparticles could be precisely adjusted between 45 and 100 nm, showing the high precision that this synthetic strategy offered. Moreover, the reaction was successfully applied to grow a mesoporous silica shell around nanoparticles with different composition and shapes, reflecting the general applicability of this synthetic procedure (Figure 8). However, this apparently simple strategy requires the optimization of multiple reaction parameters in order to obtain nanoparticles with well-defined physico-chemical properties in a reproducible way, as we will show in the following sections.

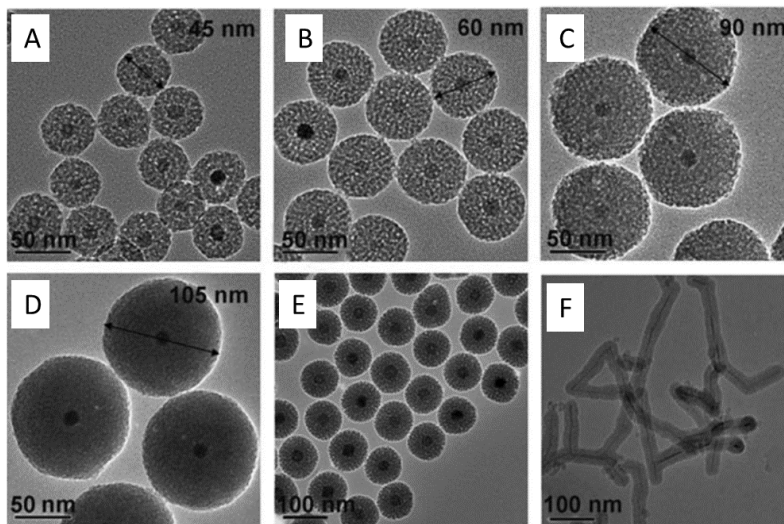


**Figure 8:** Different sized core-shell M-MSNs with 15 nm  $\text{Fe}_3\text{O}_4$  cores (A-D). Core-shell MSNs with MnO cores (E) and  $\alpha\text{-FeOOH}$  nanotubes coated with a shell of silica (F). Adapted from *Angew. Chem. Int. Ed.* 47, 8438–8441 (2008)

#### 4.1.3. Formation mechanisms in surfactant-templated materials

The development of a general and reproducible strategy for the synthesis of core-shell M-MSNs relies on a proper understanding of the processes involved in the reaction. This is fundamental in order to identify which reaction parameters are likely to have a major influence on the outcome of the reaction. In order to do this, we have revised the main formation mechanisms proposed for the synthesis of surfactant-templated materials, focusing on the formation of spherical MSNs and core-shell M-MSNs.

##### 4.1.3.1. Liquid crystal templating

Soon after the discovery of the M41S family of materials, several mechanisms were proposed in an attempt to explain the formation of ordered surfactant-templated materials. As already mentioned, a liquid crystal templating (LCT) mechanism was originally proposed based on the similarities between the mesoporous structure of M41S materials and known surfactant liquid crystal phases.<sup>2,3</sup> In the case of MCM-41 materials, which are characterized by a hexagonal

arrangement of cylindrical mesoporous channels, two alternative pathways based on the LCT mechanism were proposed.<sup>3</sup> The first pathway was a true liquid crystal templating mechanism in which surfactant molecules would assemble into a hexagonal array of rod-like micelles prior to the addition of the silicate species, as shown in the pathway (I) of Figure 9. As an alternative route, the formation of negatively charged silicate species during the hydrolysis of the silica precursor would induce the assembly of the positively-charged surfactant micelles into an

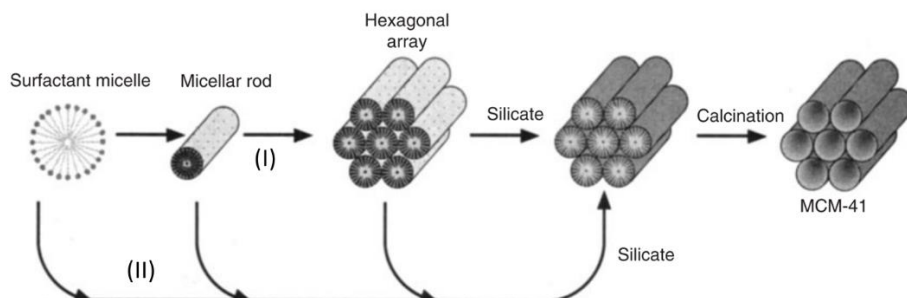


**Figure 9:** First mechanistic model proposed for the formation of MCM-41 materials. (I) Liquid crystal phase initiated and (II) silicate anion initiated. *Adapted from J. Am. Chem. Soc. 10834–10843 (1992)*

ordered hexagonal array, as shown in pathway (II).

Subsequent investigations revealed that pathway (I) was unlikely to occur when using diluted solutions of surfactants (as it was the case in most reported synthesis), since the concentration of surfactant was far below the concentration required for the formation of liquid crystal phases.<sup>43–45</sup> As a result, the pathway (II), also known as the cooperative assembly model, gained popularity and became the most common model to explain the formation of surfactant-templated materials.<sup>46</sup>

#### 4.1.3.2. Cooperative assembly model

The cooperative assembly model was extensively investigated by Stucky and co-workers, which laid the foundations of this particular formation mechanism.<sup>47,48</sup> In this model, it was proposed that the strong electrostatic interactions between positively charged surfactant molecules and anionic silicate species, would be responsible for the formation of silica/surfactant composite mesophases at surfactant concentrations below those required for a true liquid templating route.

Three main interrelated processes were identified to dominate this cooperative assembly mechanism:<sup>47</sup>

- (I) Polysilicate species would act as multidentate ligands, binding with high affinity to the positively charged surfactant micelles and creating an organic-inorganic interface.
- (II) The high concentration of silicate species in close proximity would favor the preferential polymerization of silica at the interface region.
- (III) The existence of an interfacial charge-density matching between the positively-charged head groups of the surfactant molecules and the anionic silica framework would be a fundamental structure directing factor, ultimately defining the structure of the final silica/surfactant mesophase.

Figure 10 illustrates the main steps involved in the formation of silica/surfactant mesophases according to the cooperative assembly model. An initial precursor solution of surfactant micelles is reacted with a precursor solution of oligomeric silicate species. Then, the ion-exchange of silicate species with surfactant counterions leads to silica-coated micelles that can adopt different morphologies. The strong interaction between surfactant molecules and silica species significantly screens the electrostatic repulsion between the positively-charged micelles, facilitating the self-assembly of silica-coated micelles in a dynamic and cooperative way. Finally, the resulting silica/surfactant mesophase can undergo phase transitions driven by the changing interfacial charge-density until the silica framework is completely polymerized, “freezing” the structure of the final mesoporous material.<sup>48</sup>

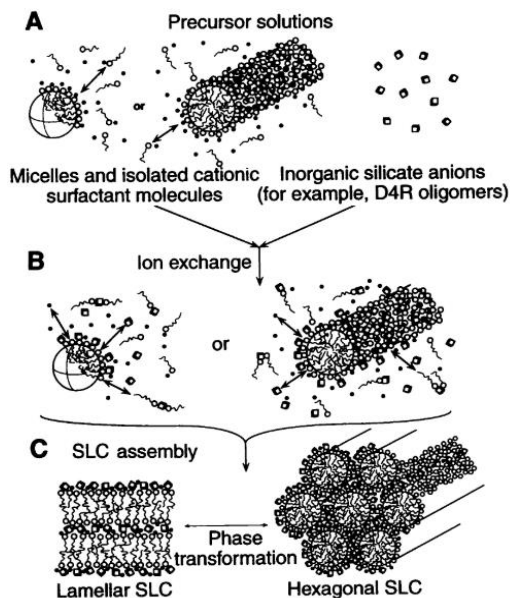


**Figure 10:** Schematic diagram of the cooperative organization of silicate-surfactant mesophases. (A) Mixture of surfactant and silicate species in the precursor solution, (B) formation of silica-coated micelles and (C) self-assembly of silica/surfactant mesophases. *Adapted from Science (80). 267, 1138–1143 (1995)*

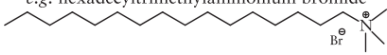
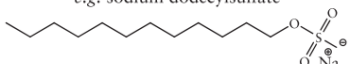
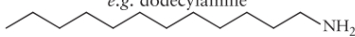
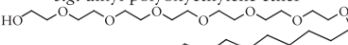
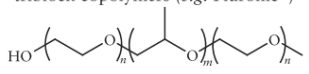
Formation of silica/surfactant mesophases has been reported even under reaction conditions in which silica condensation does not occur, which reflects the strong cooperative effect of both surfactant micelles and oligomer silica species.<sup>48</sup> This has also been observed by *in situ* small-angle XRD experiments, which showed that in a typical alkaline synthesis at room temperature, formation of an ordered silica/surfactant mesophase can be completed in just a few minutes after mixing the surfactant with the silica precursor.<sup>49</sup>

Phase transitions can occur after the assembly of the silica-coated micelles, suggesting the formation of an intermediate silica/surfactant mesophase with a certain degree of flexibility, which has been attributed to an incomplete polymerization of the silica framework.<sup>14,49,50</sup> This flexibility was experimentally observed in the synthesis of MCM-41 materials by combining a siloxane-based probe with electron paramagnetic resonance analysis, showing that the silica layer that coats the surfactant micelles was highly fluid and loosely crosslinked.<sup>51</sup> Phase transitions have been explained based on the charge-density matching between

surfactant molecules and silica species across the interface.<sup>47</sup> As the silica oligomers start to polymerize, the charge density of the silica framework decreases, inducing the rearrangement of the organic phase into a more stable mesophase configuration.

#### 4.1.3.3. Generalized cooperative assembly model

The cooperative assembly model, which was initially developed for positively charged surfactant molecules and anionic silicate species, was further extended and adapted to other surfactant/inorganic systems, leading to a generalized formation mechanism for surfactant-templated materials.<sup>52,53</sup> The different types of interactions identified between the surfactant template (S) and the inorganic species (I) are summarized in Figure 11.

Surfactant	Templating conditions	Interaction
Cationic <i>e.g.</i> hexadecyltrimethylammonium bromide 	Alkaline	$S^+I^-$
	Acidic	$S^+X^-I^+$
Anionic <i>e.g.</i> sodium dodecylsulfate 	Alkaline	$S^-X^+I^-$
	Acidic	$S^-I^+$
Neutral <i>e.g.</i> dodecylamine 	Neutral	$S^0I^0$
Nonionic <i>e.g.</i> alkyl polyoxyethylene ether  triblock copolymers ( <i>e.g.</i> Pluronic®) 	Acidic	$S^0H^+X^-I^+$
	Neutral	$S^0I^0$

**Figure 11:** Surfactants used for templating, conditions under which mesoporous silicas have been formed, and the interaction between surfactant (S) and inorganic species (I), from the charge-density matching model. Note, X is the surfactant counterion and H is a hydrogen ion. *Reprinted with permission from Porous Materials (eds. Bruce, D. W., O'Hare, D. & Walton, R. I.) 69–145 (Wiley, 2011).*

The general ideas postulated in the cooperative assembly model (*i.e.* strong electrostatic interactions between surfactant molecules and silica species, self-assembly of silica-coated micelles and charge-density driven formation of ordered silica/surfactant mesophases) are useful to understand the main processes involved



in the formation of this type of materials. However, they do not predict by themselves fundamental parameters such as the size and shape of the primary silica-coated micelles, the way these building blocks interact and assemble or how they rearrange in order to produce a specific silica/surfactant mesophase. All these processes depend on the specific reaction conditions applied in each case and are difficult to determine due to the highly dynamic nature of the involved reacting species and the short timescales at which these processes occur.<sup>54</sup> As a result, multiple mechanistic models and interpretations can be found in the literature, which are usually hypothesized based on the structural properties of the final mesoporous materials rather than *in situ* observations conducted during the reaction.<sup>46</sup>

To give just an example, Cai *et al.* prepared mesoporous particles of different sizes and morphologies through the variation of different reaction parameters.<sup>34</sup> Based on the hexagonal arrangement of channels observed in the resulting materials, the authors proposed that the particles would be formed by the assembly of silica-coated rod-like micelles whose length would be determined by the type of catalyst used in the reaction ( $\text{NH}_4\text{OH}$  or  $\text{NaOH}$ ). As a result, it was proposed that the different morphologies obtained would be produced by the different assembly combinations of these silica-coated micelles, as shown in Figure 12.

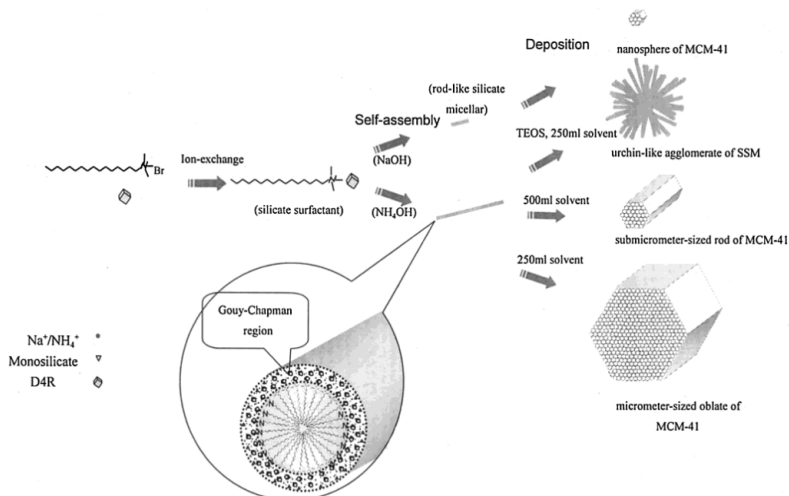


**Figure 12:** Scheme of the formation mechanism proposed by Cai *et al.* for the preparation of mesoporous silica particles of different sizes and morphologies. Reprinted with permission from *Chem. Mater.* 13, 258–263 (2001).

#### **4.1.4. Mesoporous silica nanoparticles (MSNs) and the nucleation-growth mechanism**

The preparation of mesoporous materials in the form of monodispersed nanoparticles was achieved through the combination of surfactant templating strategies and nucleation-growth processes. It is well known that a rapid homogeneous nucleation followed by a controlled particle growth are fundamental in order to obtain uniformly-sized nanoparticles.<sup>55-57</sup> In an attempt to separate both processes, Mann and co-workers implemented a quenching procedure of dilution and neutralization after the initial mixing of CTAB and TEOS under alkaline conditions, leading to monodisperse MSNs under 100 nm.<sup>33</sup> High dilutions were also used by Ostafin *et al.* in order to prepare MSNs with controlled particle sizes.<sup>36</sup> In particular, the formation of spherical MSNs with radially-aligned channels clearly indicated that a nucleation-growth mechanism was involved in the formation of these type of nanoparticles. However, this type of structure also raised new questions about the formation mechanism involved, which could not be explained simply based on the assembly of cylindrical micelles, as it was the case in MCM-41-type materials.

In these cases, it was proposed that the monodisperse MSNs would form due to the aggregation of primary silica-coated micelles around nucleation sites, which would form at the early stages of the reaction. However, the exact composition of the nucleation sites and the way the silica-coated micelles would assemble to produce the final mesostructures was mainly speculative, as can be seen in the formation mechanisms proposed by Ostafin (Figure 13).<sup>36</sup>

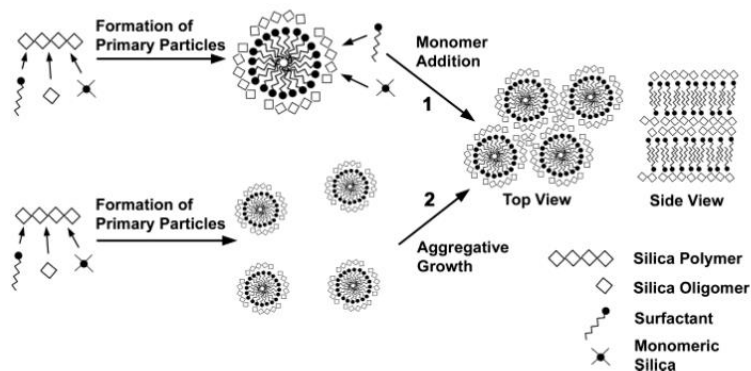


**Figure 13:** Scheme of two possible mechanisms proposed by Ostafin and co-workers for the formation of ordered mesoporous silica nanoparticles. In all cases silica polymers form initially via conventional silica chemistry. The upper pathway (1) corresponds to the monomeric addition of silica to primary particles. The lower pathway corresponds to mechanism 2, in which primary particles directionally aggregate to form particles with an ordered mesopore morphology. Nondirectional aggregative growth, mechanism 3 (not shown) would proceed in a fashion similar to mechanism 2, but the final material would have a disordered mesopore structure. *Reprinted with permission from Chem. Mater.* 14, 4721–4728 (2002).

#### 4.1.5. Core-shell MSNs and the seeded-growth method

In the case of core-shell MSNs, the aggregation of silica-coated species occurs around pre-existing colloidal nanoparticles that act as nucleation sites for the assembly of the surfactant/silica structure.<sup>40,41</sup> The main challenges that this surfactant templated seeded-growth method presents are to control the number of seeds per nanoparticle, to avoid the formation of particles without cores (secondary particles) and to prevent the aggregation between particles.

Ostafin and co-workers synthesized core-shell MSNs using gold nanoparticles as seeds and investigated the effect of different reaction parameters on the properties of the resulting nanoparticles.<sup>40,41</sup> It was observed that increasing the CTAB/silica ratio significantly reduced multinucleation, *i.e.*, the appearance of gold clusters within the mesoporous silica shell (Figure 14.A). This was attributed to a higher availability of surfactant/silica primary particles at the beginning of the reaction, facilitating a rapid and efficient coating around single gold nanoparticles. However, increasing the amount of CTAB led to the formation of secondary nanoparticles and higher degree of fusion between particles (Figure 14.B and 14.C).

This indicated that increasing the surfactant/silica ratio also favored self-nucleation processes, leading to the formation of secondary nanoparticles without cores. This could be prevented by reducing the concentration of reactants at a fixed CTAB/silica ratio, leading to monodisperse core-shell MSNs with a single gold crystal (Figure 14.D).

Overall, these results indicate that the efficient synthesis of monodisperse core-shell MSNs with uniform sizes relies on both the concentration of reagents and a proper balance between the number of seeds and the availability of surfactant/silica species.

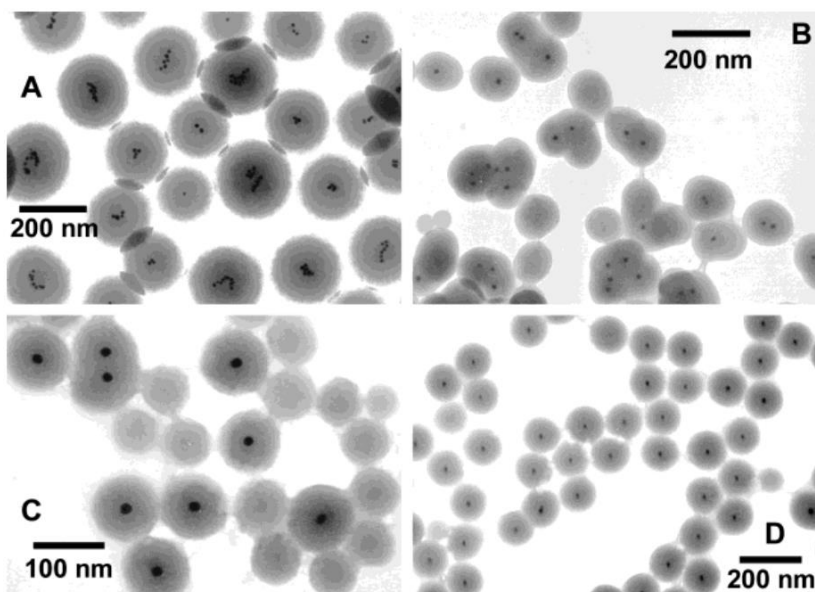


**Figure 14:** TEM micrographs showing different effects observed in the synthesis of gold core-shell MSNs. Samples A-C were synthesised with increasing CTAB/TEOS ratios, leading to a reduction of multinucleation and an increase of aggregation/formation of secondary nanoparticles. (D) Optimized CTAB/TEOS ratio together with adjustment of dilution conditions. *Adapted from Langmuir 19, 7628–7637 (2003).*

#### 4.1.5.1. Core-shell M-MSNs

Among the different types of magnetic nanoparticles, the iron oxide phases of maghemite ( $\text{Fe}_2\text{O}_3$ ) and magnetite ( $\text{Fe}_3\text{O}_4$ ) are the most widely used materials for the preparation of core-shell M-MSNs.<sup>58</sup> The coating of these iron oxide nanoparticles with a shell of silica has the additional advantage of preventing their

aggregation and increasing their stability against oxidation.

Synthetic iron oxide nanoparticles are usually prepared in the presence of oleic acid and other stabilizing surfactants in order to control their size and prevent their aggregation, which makes them hydrophobic. Accordingly, they cannot be directly used in an aqueous solution as seeds for the growth of the mesoporous silica shell. In the pioneering work of *Hyeon et al.*, a phase-transfer to water was implemented previous to the growth of the mesoporous silica shell, as shown in Figure 15.<sup>42</sup> The surfactant CTAB was used as the phase-transfer agent, which had a double role in the reaction: stabilizing the magnetic nanoparticles in water and acting as a template for the formation of the mesoporous silica shell.<sup>59</sup>

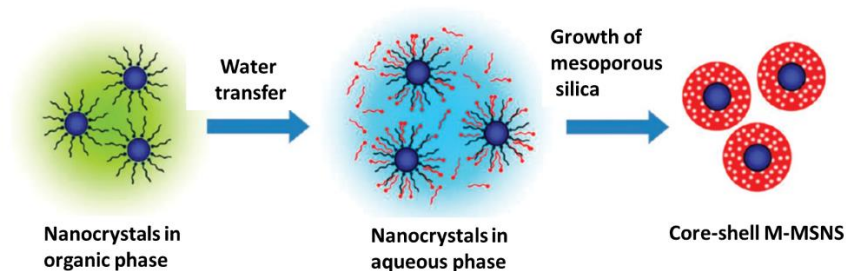


**Figure 15:** Synthetic procedure for encapsulation of hydrophobic nanoparticles within a mesoporous silica shell. *Reprinted with permission from Acc. Chem. Res. 44, 893–902 (2011).*

The great achievement of this work was the possibility to produce monodisperse core-shell M-MSNs with sizes under 100 nm. Moreover the size of the resulting nanoparticles was highly uniform and could be precisely adjusted through the variation of the initial amount of magnetic seeds used in the reaction.

Since the appearance of this pioneering work, many research groups have tried to obtain monodisperse core-shell M-MSNs with uniform sizes. However, to obtain similar nanoparticles with such a high control and precision has resulted extremely challenging, judging by the multiple variations of the original synthetic procedure that have been developed.<sup>60–65</sup> To tune the size of the core-shell M-MSNs on command was even more challenging and, to the best of our knowledge, only the group of *Ye et al.* has been able to obtain discrete nanoparticles of different sizes

comparable to those reported by Kim.<sup>66</sup> However, the approach of Ye and co-workers involved the optimization of a whole set of reaction parameters for each nanoparticle size, including the ratio between  $\text{Fe}_3\text{O}_4$ , CTAB, TEOS, NaOH and  $\text{H}_2\text{O}$ . All these results suggest that the preparation of core-shell M-MSNs with well-defined physico-chemical properties requires a precise optimization of multiple reaction parameters. Identifying those parameters and understanding their role in the reaction is therefore fundamental in order to develop a reproducible synthetic protocol for the preparation of core-shell M-MSNs.

The aim of this project was to understand the processes involved in the synthesis of this type of nanoparticles in order to determine which reaction parameters have a major influence on the reaction and establish a reproducible synthetic strategy. In this chapter we present a general synthetic strategy for the preparation of monodisperse core-shell M-MSNs with uniform sizes, analysing the effect that different reaction parameters have on the reaction in order to adjust specific structural properties such as the nanoparticle size, porosity and degree of aggregation.

## 4.2. Materials and methods

### 4.2.1. Reagents

I  $\text{FeCl}_3 \cdot 6\text{H}_2\text{O}$ ,  $\text{FeCl}_2 \cdot 4\text{H}_2\text{O}$ , oleic acid, hexadecyltrimethylammonium bromide (CTAB) and tetraethyl orthosilicate (TEOS) were purchased from Sigma. Ammonia solution (32%), ethanol and ethyl acetate were purchased from Scharlau. Chloroform was obtained from Acros Organics. Milli-Q water was used in all reactions.

### 4.2.2. Synthesis of oleate-coated USPIONS

The synthesis and purification of the oleate-coated USPIONS was conducted following the synthetic method reported in Chapter 3. A stock of oleate-coated USPIONS suspended in chloroform was prepared with an iron concentration of 3.6 mg Fe/ml determined by inductively coupled plasma mass spectrometry (ICP-MS).

### 4.2.3. Synthesis of core-shell M-MSNs (general reaction protocol)

In a typical procedure, 100 mg of CTAB were dissolved in 10 ml of milli-Q water, followed by addition of 0.58 ml of the oleate-coated USPIONS suspended in chloroform. The mixture was placed in a probe sonicator (Branson 450 Sonifier) for 2 min, giving an oil-in-water microemulsion. Then, the mixture was heated to 65 °C to evaporate the chloroform and achieve an effective phase transfer from chloroform to water. The resulting aqueous suspension of magnetic nanoparticles was transferred to a 100 ml round-bottom flask that contained 30 ml of milli-Q water and 0.547 ml of ammonia (32%). The temperature of the reaction mixture was increased to 75 °C while stirring the reaction at 400 rpm with a rugby-type stirring bar. Then, 0.5 ml of tetraethyl orthosilicate (TEOS) was added dropwise followed by addition of 3 ml of ethyl acetate. The reaction was stirred at 850 rpm for 2 minutes and then it was left stirring at 350 rpm and 75 °C during 3 h. Finally, the reaction was placed on an ice bath and the nanoparticles were collected by centrifugation (9500 rpm, 10 min). The obtained material was washed three times with 40 ml of ethanol and dried under vacuum overnight. The surfactant template was removed by calcination in air at 550 °C during 5 h.

#### **4.2.4. Characterization techniques**

Iron determination was conducted on an ICP-MS equipment from Agilent (model 7900). The oleate-coated USPIOs were digested with nitric acid (1 M) using a microwave oven operating at 200 °C.

TEM analysis was performed on a 100 kV JEOL JEM-1010 transmission electronic microscope operated with AMT image capture engine software. The core-shell M-MSNs samples were prepared by dropping 10 µl of nanoparticles suspended in ethanol onto carbon-coated copper grids.

Dynamic light scattering (DLS) experiments were conducted with a Zetasizer Nano ZS (Malvern Instruments) equipped with a laser of 633 nm and collecting the signal at 173°. Hydrodynamic size distributions were measured three times, from which the average PDI and Z-average values were obtained using Zetasizer Software (version 7.10).



## 4.3. Results

### 4.3.1. General reaction protocol

Inspired by the previous works of Kim *et al.*<sup>42</sup> and Gu *et al.*<sup>61</sup>, we developed a similar synthetic strategy using mild reaction conditions and applying a surfactant templated seeded-growth methodology. Due to their great stability and ease of preparation, the oleate-coated USPIOs developed in the first part of this project were used as seeds for the synthesis of the core-shell M-MSNs.

In a typical procedure, the hydrophobic oleate-coated USPIOs are first transferred to water using the cationic surfactant CTAB. A probe sonicator is used in order to mix the aqueous CTAB solution with the ferrofluid and facilitate an efficient interaction between the surfactant molecules and the magnetic nanoparticles. The resulting homogeneous oil-in-water-microemulsion is heated in order to evaporate the organic phase, leading to a clear brown aqueous suspension of magnetic nanoparticles, as shown in Figure 16. After the phase-transfer to water, the resulting CTAB-stabilized USPIOs can be readily used for the preparation of the core-shell M-MSNs.

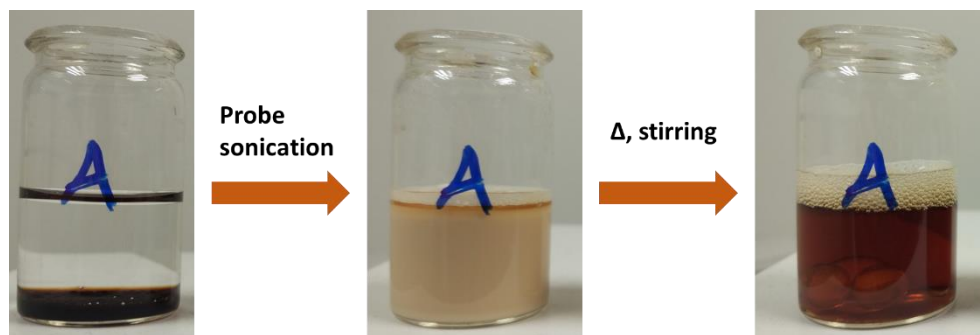


**Figure 16:** Phase transfer to water of the oleate-coated USPIOs. Initially suspended in chloroform (left), microemulsion formed after mixing with the CTAB-solution (middle) and resulting CTAB-stabilized USPIOs suspended in water (right).

The second part of the reaction involves the formation of the mesoporous silica shell around the magnetic seeds. To do this, the colloidal suspension of magnetic nanoparticles is transferred into a round-bottom flask in which the total volume of water is adjusted to 40 ml. Ammonia is then added to increase the pH to 11.5, acting

as a catalyst for the hydrolysis and condensation of the silica precursor. The temperature is increased to 75 °C previous to the addition of the silica precursor (TEOS), which is slowly added under continuous stirring. Finally, ethyl acetate is added and the reaction is stirred vigorously for a few minutes. Then, the stirring rate is reduced and a reflux condenser is attached to the flask in order to prevent the solution evaporation. The reaction is left stirring at 75 °C for 3 h.

During the first hour, the solution remains more or less transparent and then becomes turbid until a slightly orange material precipitates out. The obtained solid is washed, dried under vacuum and finally calcined in order to remove the organic template, as described in section 4.2.3 of materials and methods.

Figure 17 shows the TEM micrographs from two representative samples prepared using the described reaction protocol. The obtained nanoparticles are spherical and present a core-shell structure with at least one magnetic crystal per nanoparticle. Moreover, the size of the core-shell M-MSNs is highly homogeneous with sizes below 100 nm. Regarding the structure of the mesoporous silica shell, the nanoparticles present wormhole-like channels that seem to be arranged perpendicular to the nanoparticle surface, in agreement with a surfactant templated seeded-growth reaction.<sup>42,61</sup>

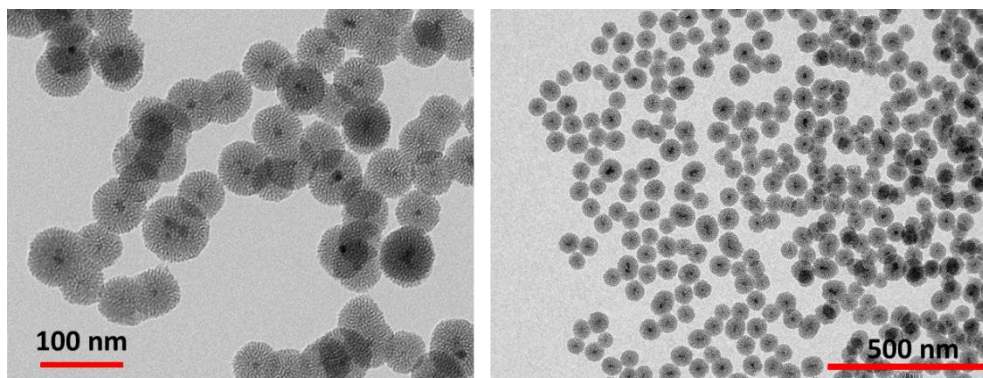


**Figure 17:** Core-shell M-MSNs obtained using the general synthetic protocol developed.

The developed synthetic protocol represented a promising starting point for the preparation of high-quality core-shell M-MSNs, becoming the reference protocol used in this project. However, reproducibility was a main issue in these preliminary trials and variations of key nanoparticle properties such as the size and

shape of the nanoparticles, the structure of the mesoporous silica shell or the degree of aggregation between the particles were observed. In an attempt to control these factors, different reaction parameters were modified, including the stirring rate and the initial amount seeds used in the reaction. However, unsuccessful results were obtained, leading to core-shell M-MSNs with different shapes and structures, as shown in Figure 18.

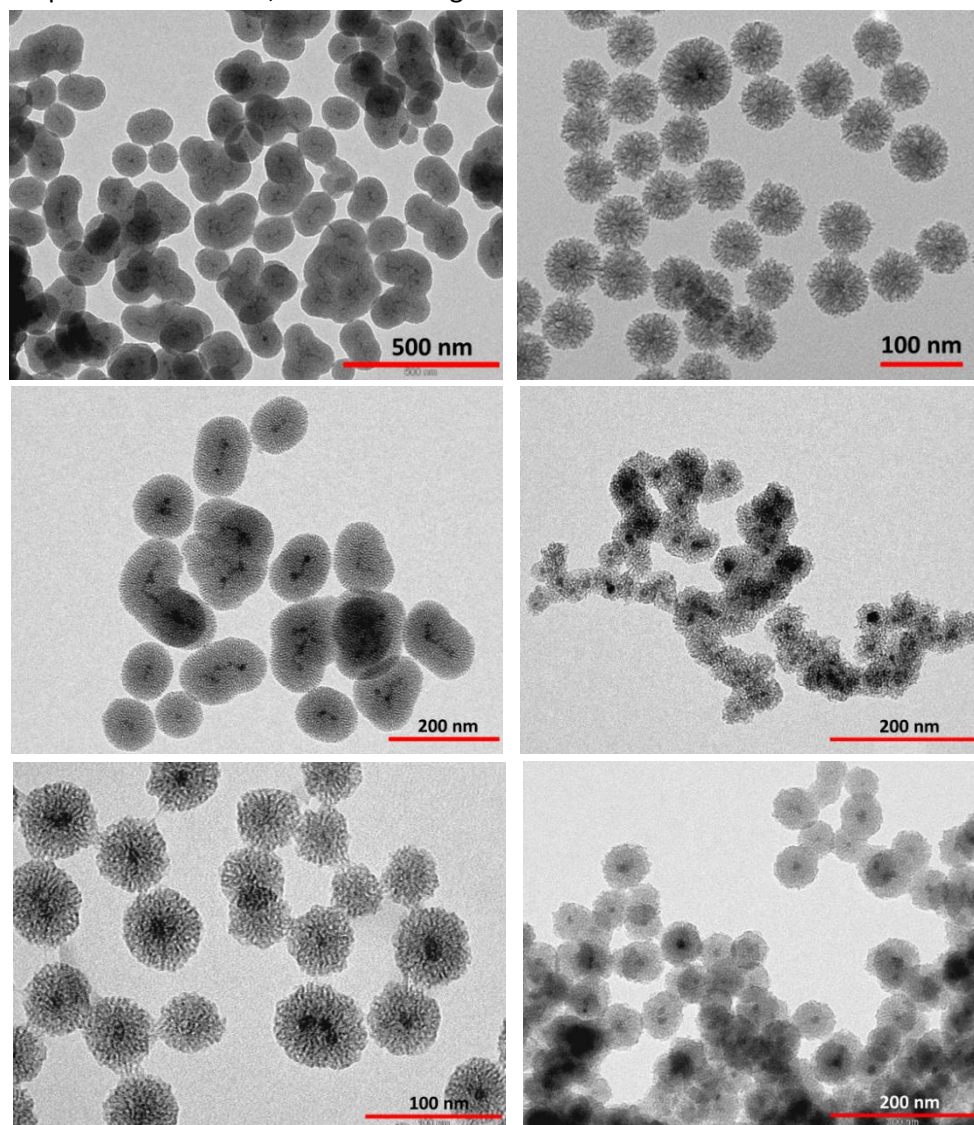


**Figure 18:** Representative TEM micrographs of core-shell M-MSNs showing the diversity of shapes and structures observed upon variation of the stirring rate or the initial amount of seeds.

All these preliminary trials confirmed that the synthesis of core-shell M-MSNs was a complex reaction in which multiple processes and factors were involved. In order to understand the rationale behind the observed effects, we decided to conduct a systematic analysis of the reaction parameters that were likely to influence the synthesis of this type of nanoparticles.

### 4.3.2. Assessment of reaction parameters

Through an extensive survey of the literature and based on the mechanistic models presented before, 11 reaction parameters were identified to be relevant for the preparation of the core-shell M-MSNs:

- Magnetic nanoparticles (type). The size, shape and ligand coating of the magnetic seeds used in the reaction may influence the formation of the core-shell M-MSNs. The oleate-coated USPIONS used in this project are irregularly shaped and present sizes between 4 and 26 nm, as already shown in the previous chapter. Moreover, they are coated with a monolayer of highly-packed oleate molecules that makes them highly stable in organic solvents. This is a fundamental requirement for an efficient phase transfer to water and the preparation of discrete magnetic seeds.<sup>67</sup>
- Magnetic nanoparticles (amount). As already discussed, the magnetic nanoparticles are used as seeds for the growth of the mesoporous silica shell. Accordingly, the initial amount of seeds used in the synthesis is expected to influence the size and polydispersity of the final nanoparticles.<sup>68</sup> The survey of several synthetic protocols for the preparation of core-shell M-MSNs showed that the concentration of  $\text{Fe}_3\text{O}_4$  seeds is usually adjusted in order to have a final iron concentration between 1.0 and 1.6 mM.<sup>42,60,61,66</sup> For the optimization of the initial amount of magnetic seeds see section 4.3.4.2.
- Surfactant. The type of surfactant is directly related to the geometry of the resulting mesoporous silica structure and the size of the mesoporous channels.<sup>2,3</sup> CTAB is probably the most common surfactant used in the

preparation of surfactant templated materials, being characterized by an ammonium polar head and a 16 carbon-long hydrocarbon tail.

CTAB is a cationic surfactant that can assemble into different types of configurations, going from more or less spherical micelles or ellipsoids,<sup>69</sup> to cylindrical-rodlike micelles,<sup>70</sup> to definitely tubular micelles and large supramicellar assemblies.<sup>71</sup> The shape and size of these surfactant micelles and supramicellar assemblies strongly depends on the surfactant concentration,<sup>45</sup> temperature,<sup>72</sup> the ionic strength (presence of salts),<sup>73,74</sup> and the polarity of the medium (e.g. alcohol content of the aqueous solution).<sup>75</sup> Accordingly, all these factors are also expected to influence the formation of the core-shell M-MSNs.

The concentration of CTAB used in our synthetic protocol (6.86 mM) is above the critical micellar concentration of CTAB (~ 1 mM at 300 °K).<sup>70,76</sup> Structural studies about CTAB micellar systems have shown that the micellar properties of CTAB are largely constant in the concentration range between 1 mM and 10 mM, being characterized by more or less spherical micelles with sizes around 5 nm.<sup>71,76</sup> Accordingly, previously to the addition of the silica precursor, we expected to find this type of spherical/ellipsoidal small CTAB micelles.

- Silica source. The most common silica sources used in the synthesis of mesoporous materials are monomolecular forms of silica, such as silicic acid or tetraalkoxysilane species with the formula  $\text{Si}(\text{OR})_4$ .<sup>16</sup> The organic group (-R) of these alkoxy silane species determines the rate of hydrolysis and the corresponding formation of soluble forms of silica. In alkaline conditions, the rate of hydrolysis is directly related to the length of the alkyl chain, following the trend:  $\text{TMOS} > \text{TEOS} > \text{TPOS} > \text{TBOS}$ .<sup>20,41</sup> This is an important factor to consider since it has been suggested that the rate of hydrolysis of the precursor is the limiting step for the growth of the silica particles.<sup>69,77</sup>

The rate at which the silica precursor is added into the solution also determines the availability of soluble silica. A particularly interesting

example was provided by Knezevic and co-workers, who observed that the rate of addition of TEOS could determine the structure of the resulting M-MSNs, leading to radial mesoporous channels when added dropwise (Figure 19.A) in contrast to the hexagonal arrangement of channels observed when the silica precursor was rapidly injected (Figure 19.B).<sup>78</sup>

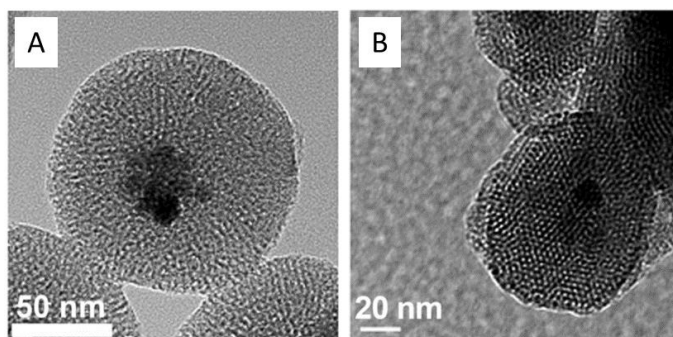


**Figure 19:** TEM micrographs showing the structural variation observed in core-shell M-MSNs when A) the silica precursor was added dropwise (radially aligned mesoporous channels) and B) the silica precursor was rapidly injected (hexagonally arranged mesoporous channels). *Adapted from Chem Plus Chem 77, 48–55 (2012).*

- CTAB/TEOS ratio. The ratio between the surfactant and the silica precursor has also been shown to affect both the morphology and the internal mesoporous structure of the MSNs.<sup>32</sup> In the case of core-shell M-MSNs, Toprak *et al.* modified different reaction parameters (including the CTAB/TEOS ratio) in order to control the size of the resulting nanoparticles.<sup>66</sup> However, this seems a complicated strategy in order to develop a reproducible synthetic protocol. As a result, in this project all the reactions are conducted at a fixed CTAB/TEOS ratio of 1:8, which was selected based on the ratio reported by Kim *et al.*<sup>42</sup>
- pH and type of catalyst. The hydrolysis and condensation of tetraalkoxysilanes in water is catalyzed both under alkaline and acidic conditions.<sup>79</sup> This again is fundamental in order to control the rate of hydrolysis of the silica precursor and the dynamics between the hydrolysis condensation processes, which can influence important structural factors

such as the ordering within the mesoporous silica structure or the size and shape of the resulting nanoparticles.<sup>80</sup>

The preparation of core-shell M-MSNs is usually conducted under alkaline conditions using ammonia or sodium hydroxide as catalysts of the reaction. In this project, ammonia is added previous to the addition of the silica precursor, providing an initial reaction pH of 11.5.

- Solvent and dilution. Although the condensation of silica can be conducted in organic solvents, the assembly of micellar structures for the synthesis of mesoporous structures is usually conducted in aqueous solutions. Pure ion exchanged water was used in this project in order to avoid the presence of unwanted ionic species that could interfere in the assembly of the surfactant/silica mesophases.

As already mentioned in the introduction, controlling the dilution of the initial reaction components is fundamental for the preparation of mesoporous materials in the form of nano-sized particles.<sup>34-36</sup> In the case of core-shell M-MSNs, the initial magnetic nanoparticles have to be well dispersed in order to facilitate the growth of the mesoporous silica shell around single nucleation sites.

- Co-solvents. Co-solvents have been traditionally incorporated into the synthesis of surfactant templated materials in order to control the phase behaviour of the surfactant template and the formation of the resulting silica/surfactant mesophase.<sup>15</sup>

Alcohols are also used as homogenizing agents for the solubilisation of alkoxy silanes in water.<sup>81</sup> The Stober method is a classical example, in which different alcohols are used in order to prepare monodisperse spherical silica particles.<sup>20</sup> Similarly, addition of alcohols to the synthesis of mesoporous silica particles has shown to affect the morphology of the resulting nanoparticles and to facilitate the formation of spherical MSNs.<sup>22,36</sup>

On the other hand, other co-solvents such as ethyl acetate or ethylene glycol can be found on different synthetic protocols.<sup>42,61,62,66</sup> It has been

suggested that the use of ethyl acetate prevents the formation of interconnected particles,<sup>82</sup> which may be related to its effect on the control of the pH of the reaction. The progressive hydrolysis of ethyl acetate into ethanol and acetic acid, lowers the pH of the reaction, reducing the polymerization and condensation rate of silica.<sup>83</sup>

In this project, ethyl acetate is used as a co-solvent following the synthetic protocol developed by Kim *et al.*<sup>42</sup> Although ethanol is not directly added as a reagent, it is important to note that it will be produced during the hydrolysis and condensation of TEOS and also during the hydrolysis of ethyl acetate, representing up to the 5% of the total volume of reaction.

- Stirring. Although it may not seem as a very important reaction parameter, stirring plays a fundamental role in the synthesis of the core-shell M-MSNs. Surfactant templated materials are synthesised in a complex and heterogeneous reaction mixture where the distribution of the different reagents and the interplay between them determines the outcome of the reaction.<sup>19</sup>

In the case of core-shell M-MSNs, the initial reaction mixture is composed of a large number of colloidal nanoparticles (CTAB-stabilized USPIONs) and highly-dynamic CTAB micelles. The subsequent addition of the silica precursor (TEOS) leads to the formation of an oil-in-water emulsion due to the immiscibility of TEOS in water. As a result, the stirring conditions applied play a fundamental role in the formation of the emulsion, facilitating the fragmentation of the droplets of TEOS into smaller emulsion droplets and their association with CTAB. The smaller the oily droplets, the higher the interfacial area, which ultimately determines the rate of hydrolysis and solubilisation of TEOS. For this reason, the stirring conditions applied, including the stirring rate, shape of reaction vessel and shape of stirring bar, are expected to be critical in the synthesis of the core-shell M-MSNs.

In this project, a sequential stirring procedure is applied, in which stirring is increased after the addition of the silica precursor in order to



homogenize the reaction mixture, followed by a reduction of the stirring rate (see section 4.3.4.1 for optimization of stirring conditions).

- **Temperature.** Temperature is another factor that controls the rate of hydrolysis and condensation of silica. Although the formation of mesoporous silica structures has been reported to occur at room temperature,<sup>84–86</sup> temperatures between 60–100 °C are usually employed in order to facilitate a complete condensation of the mesoporous silica framework.<sup>16</sup> In this project, a reaction temperature of 75 °C was selected.

Increasing the temperature of reaction has also been reported to accelerate the growth of MSNs,<sup>69</sup> affecting the size of the resulting nanoparticles. Although higher nanoparticle sizes are usually reported with higher temperatures,<sup>27,69,87</sup> the opposite effect has also been observed under certain conditions.<sup>29</sup> This again reflects that the different reaction parameters are interconnected, making difficult to predict the outcome of the reaction without considering the whole set of parameters involved.

The temperature of reaction has also been found to play an important role on the aggregation of the obtained MSNs.<sup>88</sup> Figure 20 shows the difference of aggregation observed when TEOS was added to the initial reaction mixture at room temperature (A) vs the addition of TEOS at a reaction mixture heated to 60 °C (B).

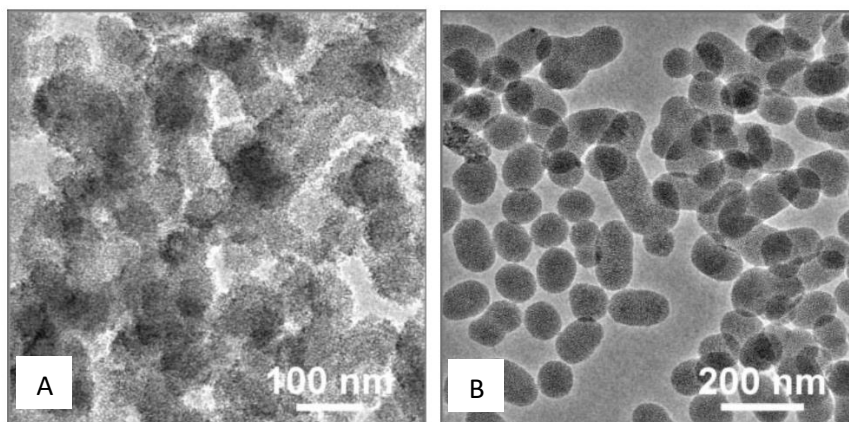


**Figure 20:** TEM micrographs showing the different aggregation observed in the preparation of MSNs when the silica precursor was added to a reaction mixture at (A) room temperature or (B) 60 °C. Adapted from *Adv. Funct. Mater.* **17**, 605–612 (2007).

- **Reaction time.** The total time used for the formation of surfactant templated materials is probably one of the most varying reaction parameters found in the literature.

The use of *in situ* characterization techniques has revealed that under alkaline conditions and reaction temperatures of 30 °C, mesophase structures can be observed just a few minutes after the mixing of the silica precursor with the surfactant template.<sup>49,89</sup> In the case of MSNs, similar results have been reported in which spherical MSNs can form in a matter of minutes.<sup>33,62</sup> However, the complete polymerization of the silica framework can take several hours and sometimes aging times of several days are reported in order to prepare mesoporous materials that are stable to calcination.<sup>90</sup>

In the case of core-shell M-MSNs, reaction times of several hours are usually reported. In this project a reaction time of 3 h was initially selected based on previous synthetic protocols.<sup>42,60,61,66</sup> For the optimization of reaction times see section 4.3.4.4.

#### 4.3.2.1. Summary of reaction parameters selected for the preparation of the core-shell M-MSNs (general synthetic protocol)

<b>Magnetic nanoparticles (type)</b>	<b>Oleate-coated USPIOs (Fe<sub>3</sub>O<sub>4</sub>)</b>
<b>Magnetic nanoparticles (amount)</b>	12.5 μmol (Fe <sub>3</sub> O <sub>4</sub> )
<b>Surfactant</b>	CTAB (0.27 mmol)
<b>Silica source</b>	TEOS (2.24 mmol)
<b>CTAB/TEOS ratio</b>	1:8
<b>Catalyst and pH</b>	NH <sub>3</sub> (7.52 mmol), pH = 11.5
<b>Solvent</b>	Water (2222 mmol)
<b>Co-solvent</b>	AcOEt (30.7 mmol)
<b>Stirring</b>	850 rpm /350 rpm
<b>Temperature</b>	75 °C
<b>Reaction time</b>	3 h

### 4.3.3. Semi-empirical model

The multiple parameters involved in the synthesis of core-shell M-MSNs together with the variability of reaction conditions found in the literature represented a complex scenario for the optimization of the reaction conditions. In order to introduce some rationale into the formation of this type of nanoparticles, a semi-empirical model was used as a reference during the optimization stage. The aim of this model was to predict (or at least provide a general framework to explain) the different effects produced in the reaction when one or more parameters are modified.

The semi-empirical model was kindly developed by Dr Vicent Esteve Moya. It was built based on the existing mechanistic knowledge about the synthesis of core-shell M-MSNs and the reaction parameters established in our general synthetic protocol. Combining the ideas of the cooperative assembly model and the seeded-growth method, it was hypothesized that spheroidal silica-coated micelles are the fundamental building blocks for the formation of the mesoporous silica shell that grows around the magnetic nanoparticle seeds. Accordingly, the way these silicated micelles self-assemble and the connectivity between them will determine the structure (and porosity) of the final nanoparticles.

Figure 21 shows a first approximation to the assembly of spherical silica-coated micelles of 5 nm around a 10 nm spherical magnetic core, which is believed to initiate the growth of the mesoporous silica shell. Whether the silica-coated micelles are spherical,<sup>87,91</sup> cylindrical,<sup>92,93</sup> or of an undetermined shape,<sup>94</sup> is still a matter of dispute in the mechanistic models found in the literature.

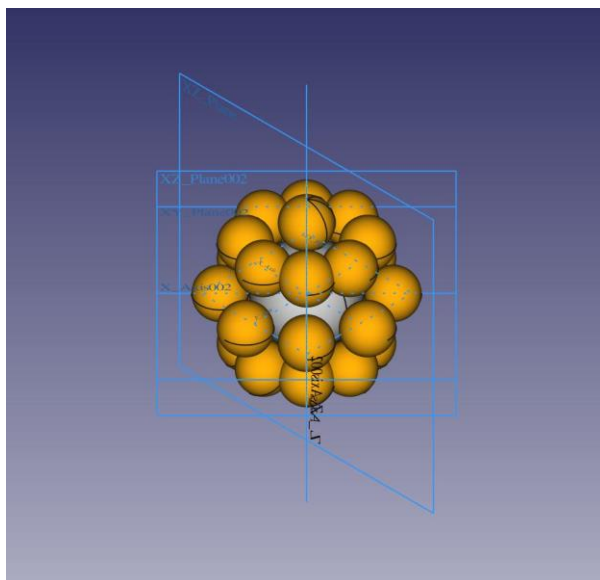


**Figure 21:** Schematic representation of the assembly of spherical spheres of 5 nm around a central spherical core of 10 nm.

This seeded-growth mechanism was in agreement with the results obtained in the preliminary experiments conducted in this project. On the one hand, the absence of secondary nanoparticles without magnetic cores evidences a preferential assembly of the silica-coated micelles around the magnetic seeds. On the other hand, the spherical shape of the particles with the magnetic cores placed at the center, suggests an isotropic growth of the mesoporous silica shell from the core to the outer part of the particles.

Once the magnetic cores are covered by a first layer of silica-coated micelles, it is expected that additional layers will assemble until eventually all the silica-coated micelles present in the reaction mixture are consumed. According to this hypothesis, the availability of surfactant micelles during the reaction would be critical for the growth of the silica shell. The dependence between the amount of surfactant used in the synthesis and the thickness of the mesoporous silica shell has been already reported in several studies in which mesoporous silica nanoparticles are obtained through a seeded-growth mechanism.<sup>66,91</sup>

Finally, the fusion of spheroidal micelles within the different layers assembled around the core would lead to elongated micellar structures that will eventually

develop into a network of radially aligned wormhole-like channels. The fusion of spheroidal micelles into elongated wormhole-like structures is a common phase transition found in aqueous micellar solutions.<sup>95</sup> The transition is greatly favoured by the presence of electrolytes, which decrease the repulsion between the head-groups of the surfactant molecules and favour the formation of micellar structures with reduced curvature, as shown in Figure 22.<sup>73,96</sup> As a result, the presence of anionic silica species is expected to play a double role during the formation of the silica/surfactant mesophase: triggering a transformation of the micelle's morphology itself (intramicellar rearrangement of surfactant molecules) and facilitating the assembly of the micelles around the magnetic core (screening intermicellar repulsive interactions). This hypothesis is supported by computational simulations, in which the interactions between anionic silica species and cationic surfactant molecules are identified as the main driving force for the fusion of spherical micelles into wormhole-like channels.<sup>97</sup>

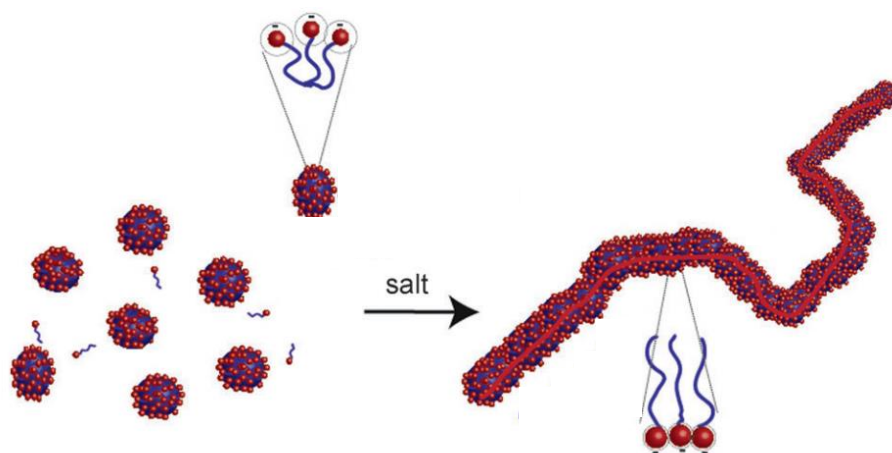


**Figure 22:** Schematic representation of the transition from globular to long flexible cylindrical (worm-like) micelles upon addition of electrolytes. Adapted from *Angew. Chemie - Int. Ed.* 53, 11524–11528 (2014).

The semi-empirical model was conceived as a quantitative approach to establish relationships between the different factors involved in the reaction and resulted a useful tool in order to estimate and predict basic parameters such as the final size of the core-shell M-MSNs, the surface area of the material or the yield of

the reaction. In order to predict these values, the model takes into account all the reagents that participate in the reaction and evaluates the approximate balances of the components into the different compartments (phases) of the system: solution, emulsion, magnetic nanoparticle surface, micelle surface, micelle interior and core-shell M-MSNs.

Incorporation of the different reaction components into a unified model was also fundamental for the optimization of reaction conditions, showing the relationships between multiple parameters and their overall effect on the reaction. In particular, the effect that different amounts of seeds have on the size of the resulting nanoparticles has been evaluated with the model, providing a reference value for the preparation of core-shell M-MSNs with a precise nanoparticle size.

### **4.3.4. Optimization of reaction parameters**

#### 4.3.4.1. Initial reaction mixture

As a first step for the optimization of the reaction, the initial reaction mixture was analysed previous to the addition of the silica precursor. Following the developed synthetic protocol, 100 mg of CTAB were dissolved in 10 ml of milli-Q water and mixed with 0.58 ml of oleate-coated USPIONs (3.6 mg Fe/ml). After sonication and evaporation of chloroform, the resulting aqueous suspension of CTAB-stabilized nanoparticles was added to 30 ml of milli-Q water with 0.547 ml of ammonia (32%). After mixing, an aliquot was taken and analysed by DLS in order to assess the colloidal stability of the CTAB-stabilized USPIONs under the initial reaction conditions. As can be seen in Figure 23, a major population with an intensity-weighted average size of 31 nm was identified, consistent with the hydrodynamic size expected for the CTAB-stabilized USPIONs.<sup>61</sup> A smaller population with an average size above 100 nm was also identified, which could be attributed to the presence of large and dynamic surfactant supramicellar assemblies.

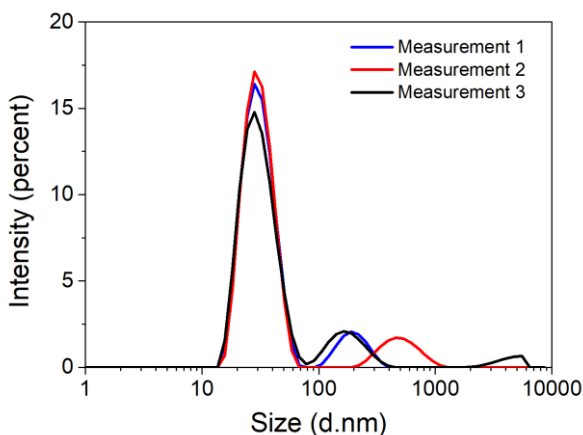


**Figure 23:** Intensity-weighted hydrodynamic size distribution of CTAB-stabilized USPIOs in the initial reaction mixture for the synthesis of core-shell M-MSNs.

It is important to note that the surfactant used in the synthesis of the core-shell M-MSNs has a double role in the reaction, acting as a phase-transfer agent and as the organic template for the formation of the mesoporous silica structure. Accordingly, an excess of surfactant is used for the phase transfer to water of the hydrophobic oleate-coated USPIOs, leading to a mixture of magnetic nanoparticles and surfactant micellar structures in the initial reaction mixture. However, the large sizes obtained in the DLS experiment (above 100 nm) were in marked contrast with the 5 nm CTAB micelles expected to be present under the reaction conditions applied.<sup>71,76</sup> Moreover, the presence of small CTAB micelles was also one of the assumptions used to develop the semi-empirical model, since they are considered the basic building blocks for the formation of the mesoporous silica shell.

In order to get a better insight into the potential micellar structures present in our initial reaction mixture, a second sample with the same CTAB concentration and pH conditions used in the synthesis of the core-shell M-MSNs but without magnetic nanoparticles was prepared and analysed by DLS. The measurements again showed two distinctive populations, as shown in Figure 24.A. However, in this case the main population presented an intensity-weighted average size of 4.5 nm, in perfect agreement with the size of spherical/micellar CTAB micelles.<sup>71,76</sup> The

second population presented sizes over 100 nm, similarly to what was observed in the sample with the magnetic nanoparticles. This confirmed that formation of large supramicellar assemblies was possible under the reaction conditions applied. However, the proportion of these supramicellar assemblies was negligible compared to the number of small CTAB micelles, as suggested by the number-weighted distribution of sizes (Figure 24.B).

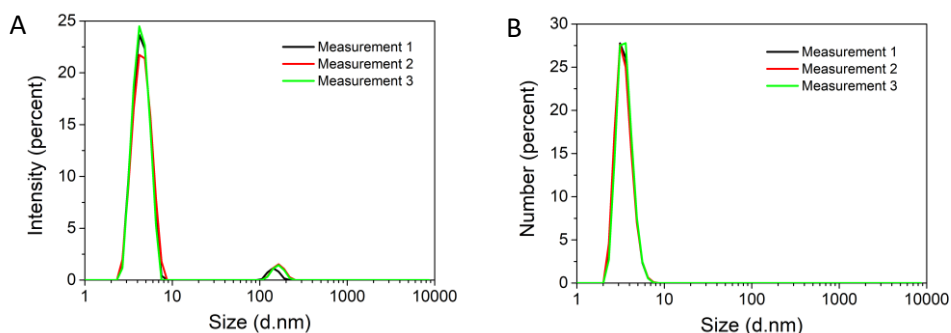


**Figure 24:** Hydrodynamic size distribution of CTAB micelles in the initial reaction mixture for the synthesis of core-shell M-MSNs. (A) Intensity-weighted distribution and (B) Number-weighted distribution.

Interestingly, these small CTAB micelles could not be detected in the initial reaction mixture when the CTAB-stabilized USPIOs were also present. This could be explained based on the different nature of both types of particles. The intensity of scattered light depends on the sixth power of the radius of the scattering particle,<sup>98</sup> therefore the amount light scattered by the large and solid magnetic nanoparticles is much larger than the light scattered by the small and dynamic surfactant micelles. The different behavior between these two systems was clearly reflected in the laser power applied by the DLS equipment, which is automatically attenuated depending on the intensity of light scattered by the sample. When only CTAB micelles were present, the equipment used an attenuator index of 11 (no attenuation), which is applied when a small amount of light reaches the detector due to poor scattering. On the other hand, in the case of the mixture of magnetic nanoparticles and surfactant micelles, the attenuator index was automatically set to 9, which corresponds to 90% laser attenuation. This indicates that most of the



light that reaches the detector corresponds to the solid nanoparticles, making difficult to detect the smaller surfactant micelles.

#### 4.3.4.2. Stirring conditions

As already shown, the synthesis of core-shell M-MSNs is a multi-component reaction in which the interactions between colloidal nanoparticles (CTAB-stabilized USPIONS), surfactant micelles and emulsion droplets of TEOS are critical. At the nanometric domain almost all kinds of forces are involved. Aside of forces present in the molecular domain, macroscopic-like forces are also present and thus inertial forces grow in importance. As a result, the stirring conditions applied are expected to have profound effects on the outcome of the reaction. Surprisingly, this key reaction parameter is usually overlooked in most reaction protocols regarding the synthesis of core-shell M-MSNs. In fact, it is hard to find clear indications about the stirring conditions applied in each case, which are usually reduced to vague descriptions about the stirring rate used. “Gentle stirring” and “vigorous stirring” are common examples found in the literature.

A detailed description of the stirring conditions applied is not simple since many factors are involved, including the shape and size of the reaction vessel, type of stirring (mechanical, magnetic...), size and shape of stirring bar/blades and the stirring rate applied. For this reason, the limited or non-existent description of stirring conditions applied, makes difficult to reproduce the experimental results obtained in different synthetic protocols. The lack of standardized stirring protocols makes also difficult to differentiate the effect that stirring conditions have on the morphology and structure of the final nanoparticles compared to the effect of other reaction parameters. For all these reasons, we decided to establish a clear stirring protocol that could be used to investigate the effect of stirring in the synthesis of core-shell M-MSNs.

#### Magnetic stirring vs mechanical stirring

The first factor to be investigated was how to stir the reaction mixture. When working with magnetic nanoparticles, it is important to bear in mind that their permanent magnetic moment can interact with the magnetic field produced by

magnetic stirring bars. This would generate a concentration gradient of magnetic nanoparticles around the stirring bar and, in the case of a strong magnetic interactions, the number of available nanoparticles could be significantly reduced.

As an alternative to magnetic stirring, we decided to investigate the applicability of mechanical stirring in the synthesis of core-shell M-MSNs. With mechanical stirring, non-magnetic stirring blades (Teflon) are immersed into the reaction mixture and the stirring rate is controlled through a mechanical stirring motor. Application of mechanical stirring to the general synthetic protocol developed led to a heterogeneous mixture of nanoparticles with different sizes, as shown in Figure 25. Nanoparticles with multiple magnetic cores were identified together with a large amount of nanoparticles without magnetic core. Interestingly, a few large nanoparticles with sizes above 400 nm were also observed. These results showed that stirring was a critical parameter in the reaction and indicated that excessive turbulence and the likely appearance of microvortices and microcavitation processes generated by the sharp stirring blades,<sup>99</sup> was detrimental for an even distribution of the reaction components, leading to higher nanoparticle heterogeneity.

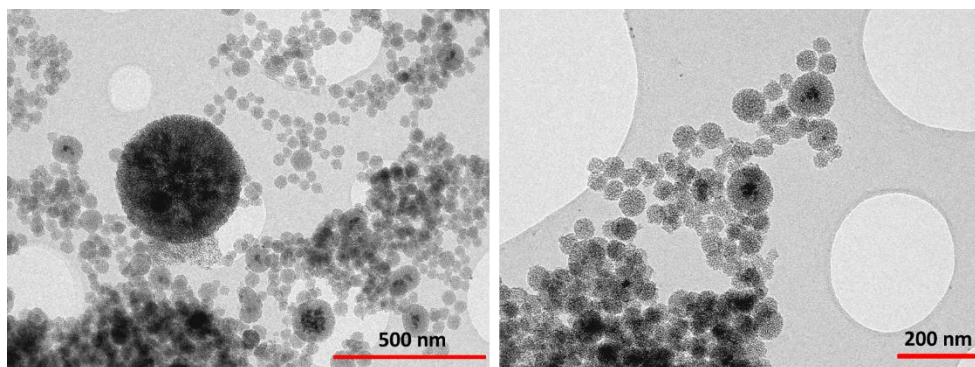


**Figure 25:** Representative TEM micrographs of the core-shell M-MSNs obtained using the general synthetic protocol developed and mechanical stirring.

Although mechanical stirring is a powerful alternative when large volumes or viscous solutions have to be stirred, the precision at which the stirring rate can be adjusted is much limited than with magnetic stirring. This determined our choice for magnetic stirring in order to prepare uniform core-shell M-MSNs. We observed

that, under the reaction conditions developed, the immersion of a rugby-type stirring bar of 2 cm into the initial reaction mixture did not perturb the homogeneity of the colloidal suspension of magnetic nanoparticles. Regarding the reaction vessel, a 100 ml round-bottom flask was used in all the reactions described in this work.

### Stirring rate

Regarding the stirring rate, it was important to achieve two different goals. First, to guarantee a homogeneous distribution of the reaction components for an efficient interaction between them. Second, to avoid the generation of turbulences and concentration gradients that would favour the formation of a heterogeneous mixture of nanoparticles.

When the reaction was conducted at a stirring rate of 550 rpm (3 h), single core-shell M-MSNs together with dimers and trimers were obtained, as shown in Figure 26.A. Conversely, when a higher stirring rate was applied (850 rpm, 3 h), the resulting particles were discrete and predominantly single-core (Figure 26.B). The stirring rate applied not only influenced the fusion of nanoparticles but also the structure of the final mesoporous silica shell. Whereas the nanoparticles obtained at 550 ppm presented a uniform silica shell with well-defined edges, the nanoparticles obtained at 850 rpm presented a less ordered mesoporous structure.

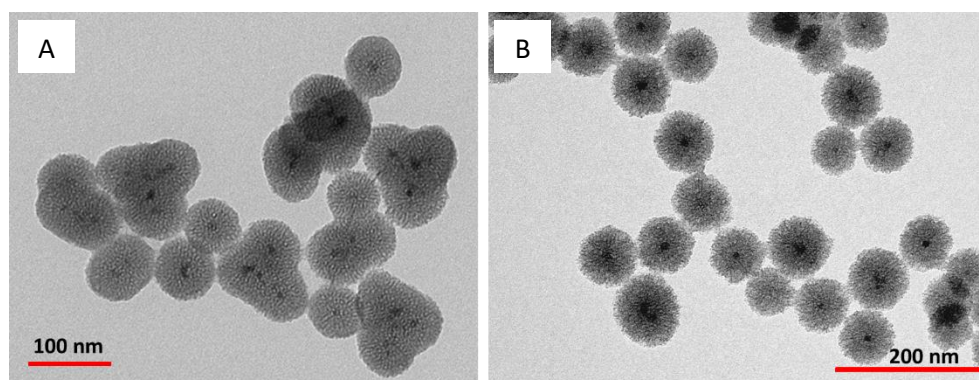


**Figure 26:** Representative TEM micrographs of the core-shell M-MSNs obtained when the reaction was conducted at (A) 550 rpm (3 h) and (B) 850 rpm (3 h).

These results can be explained based on the preferential assembly of silica-coated micelles around the pre-existing magnetic seeds. Using a low stirring rate, leads to the formation of clusters due to the fusion of single nanoparticles during the formation of the mesoporous silica shell. On the other hand, low stirring conditions favour the formation of well-ordered mesoporous structures.

High stirring rates (850 rpm, 3 h) lead to magnetic nanoparticles that are well dispersed, facilitating an efficient coating of single magnetic seeds and preventing the formation of nanoparticle clusters. However, application of high stirring rates also influence the assembly of the silica-coated micelles, leading to a more disordered mesoporous structure.

In order to overcome this problem, a sequential stirring procedure was implemented. Vigorous stirring was applied after the addition of the silica precursor in an attempt to distribute the different reaction components and prevent the formation of clusters. Then, the stirring rate was reduced in order to facilitate the formation of an ordered mesoporous structure. The different combinations of times and rates of stirring investigated are summarized in Table 1.

**Table 1:** Stirring parameters used in the different stirring conditions evaluated.

	<b>Initial stirring</b>	<b>Main reaction stirring</b>
<b>Condition 1</b>	850 rpm, 10 min	350 rpm, 3 h
<b>Condition 2</b>	850 rpm, 2 min	350 rpm, 3 h
<b>Condition 3</b>	1050 rpm, 2 min	350 rpm, 3 h
<b>Condition 4</b>	650 rpm, 2 min	350 rpm, 3 h

Application of a high stirring rate (850 rpm) during the first 10 minutes of reaction revealed that the formation of dimers and trimers could be effectively prevented by a sequential stirring procedure, as shown in Figure 27.A. However, the obtained core-shell M-MSNs were not perfectly spherical and the structure of the mesoporous shells looked slightly disorganized. In condition 2, the time of initial stirring at 850 rpm was further reduced from 10 to 2 minutes, leading to nanoparticles with well-defined structures and mostly a single magnetic core per nanoparticle (Figure 27.B).

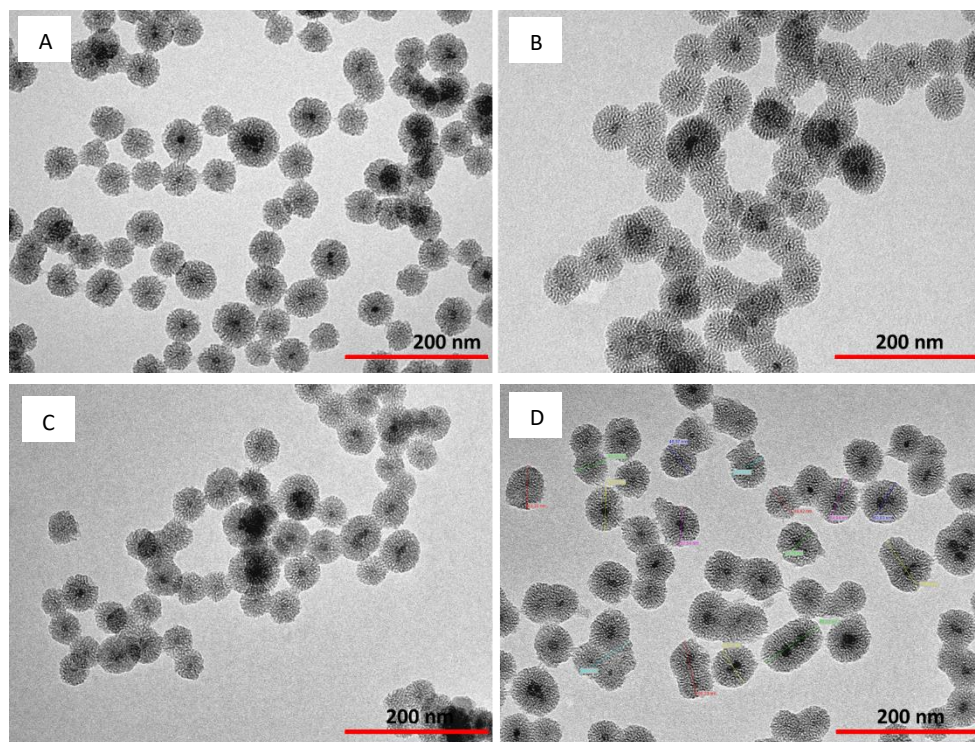


**Figure 27:** Representative TEM micrographs of the core-shell M-MSNs obtained under the stirring conditions 1 (A), 2 (B), 3 (C) and 4 (D).

These results suggested that the first minutes of reaction are critical for the formation of the core-shell M-MSNs. The intensity of stirring was therefore evaluated during the first 2 minutes of reaction in conditions 3 and 4. Excessively turbulent stirring (1050 rpm, 2 min) again led to a more disorganized mesoporous structure (Figure 27.C), whereas dimers and trimers formed when the stirring rate was reduced to 650 rpm (Figure 27.D). As a result, an initial stirring rate of 850 rpm during 2 minutes was selected as the optimal value for the preparation of single-core M-MSNs with ordered mesoporous silica structures.

### 4.3.4.3. Initial concentration of magnetic seeds

As already mentioned in this work, the synthesis of the core-shell M-MSNs is based on a seeded-growth mechanism in which the initial amount of seeds used in the reaction is expected to influence the size and polydispersity of the final nanoparticles. This was already noted in the work of Kim *et al.*, in which a reduction of the total nanoparticle size was observed as the initial amount of seeds was increased.<sup>42</sup> This was also predicted by the semi-empirical model developed in this project: when a large number of seeds are used in the reaction, the amount of silica-coated micelles available per nanoparticle decreases, leading to smaller core-shell M-MSNs.

To test this hypothesis, the initial amount of seeds used in the synthesis of our core-shell M-MSNs was modified while keeping the rest of reaction parameters unaltered. The difference in the content of magnetite within the obtained materials was manifested by the colours of the samples, which went from beige in the samples prepared with less magnetic nanoparticles to an ochre colour in the samples prepared with a higher concentration of magnetic nanoparticles (Figure 28).

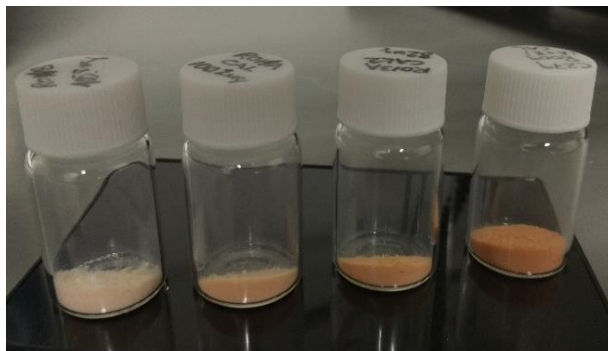


**Figure 28:** Calcined core-shell M-MSNs synthesised with increasing concentrations of magnetic seeds (from left to right).

### Low concentration of magnetic seeds

The initial concentration of magnetic nanoparticles established in the general protocol corresponds to an iron concentration of 0.85 mM, leading to nanoparticles with an average size around 70 nm. When the initial concentration of seeds was reduced (iron concentration of 0.15 mM), a mixture of large core-shell M-MSNs over 100 nm and smaller MSNs around 65 nm which lacked a magnetic core were obtained (Figure 29). This suggested that a deficiency of seeds in the initial reaction mixture favoured the self-nucleation of silica/surfactant species and the growth of secondary nanoparticles without a magnetic core, in agreement with previous observations on the synthesis of core-shell nanoparticles.<sup>40,41,100,101</sup>

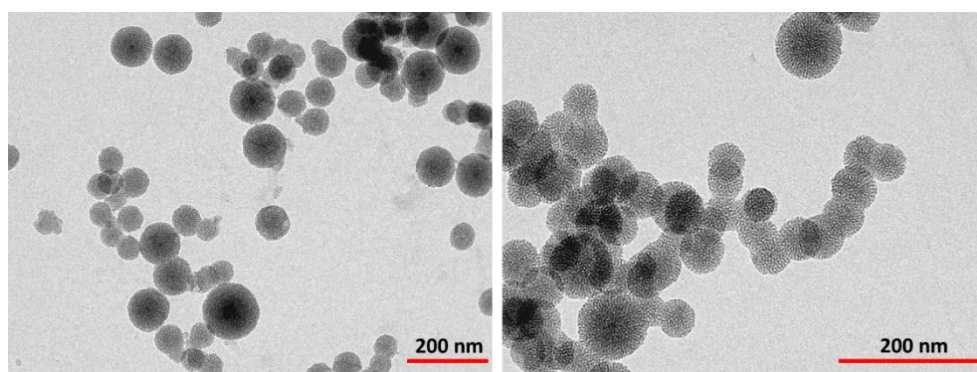


**Figure 29:** Representative TEM micrographs of the core-shell M-MSNs obtained using an initial concentration of magnetic seeds corresponding to  $[\text{Fe}] = 0.15 \text{ mM}$ .

It is important to highlight that the mesoporous structure in both nanoparticles with and without magnetic cores is exactly the same, with radially aligned mesoporous channels going from the centre to the surface of the nanoparticles. This suggests that a similar seeded-growth operates in both cases. However, the formation of nanoparticles with two different sizes suggests the existence of two differentiated growth processes. The silica-coated micelles would assemble preferentially around the pre-existing magnetic nanoparticles and, meanwhile, additional nucleation sites would form out of the saturated surfactant/silica solution, leading to a second growth process around the newly formed nucleation sites.<sup>87,88,102</sup> The appearance of this secondary nucleation is determined by the total specific surface area of the seeds and the distance between them.<sup>103</sup>

High concentration of magnetic seeds

The use of a great excess of seeds (iron concentration of 7 mM) had a completely different effect on the outcome of the reaction. In this case, interconnected chains of iron oxide nanoparticles surrounded by a thin shell of mesoporous silica were obtained, as can be seen in Figure 30. These results suggest that the presence of magnetic seeds in close proximity during the early stages of the reaction leads to a poor distribution of the silica-coated micelles and the formation of intergrowth chains of nanoparticles.

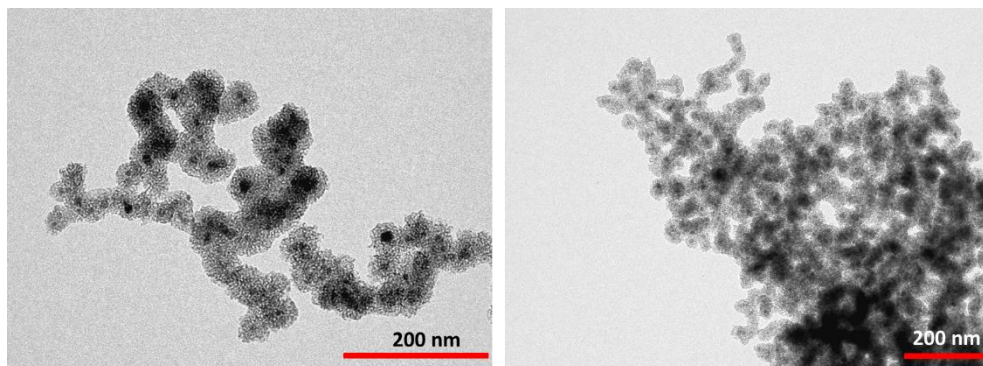


**Figure 30:** Representative TEM micrographs of the core-shell M-MSNs obtained using a great excess of magnetic seeds, [Fe]=7 mM.

In conclusion, these results showed that the initial amount of seeds used in the reaction not only determines the thickness of the silica shell but also the formation of secondary nanoparticles and the appearance of agglomeration. Accordingly, the range of nanoparticle sizes that can be prepared through the variation of the initial amount of seeds would be limited by the appearance of these unwanted effects.



### Intermediate concentrations of magnetic seeds

The formation of core-shell M-MSNs was then evaluated by using intermediate amounts of seeds. In an attempt to prevent the formation of secondary nanoparticles, the initial concentration of magnetic seeds was increased from 0.15 mM to 0.37 mM of iron. This resulted in a significant reduction of secondary nanoparticles without magnetic core and provided core-shell M-MSNs with an average size of 91 nm, as shown in Figure 31.

Further increasing the initial amount of seeds from 0.37mM to 0.44 mM of iron, completely eliminated unwanted secondary nanoparticles and favoured the formation of highly uniform nanoparticles with an average size of 88.52 nm (Figure 32.A). Accordingly, this concentration of magnetic seeds (0.44 mM of iron) was set as the lower limit for the preparation of large and monodisperse core-shell M-MSNs.

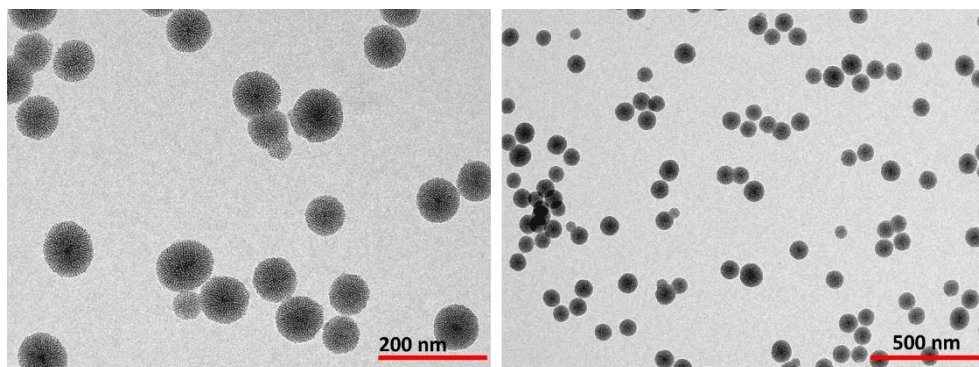


**Figure 31:** Representative TEM micrographs of the core-shell M-MSNs obtained using an initial concentration of magnetic seeds corresponding to  $[\text{Fe}] = 0.37 \text{ mM}$ .

Three additional concentrations of magnetic seeds were evaluated, corresponding to an iron concentration of 0.73 mM, 1.47 mM and 2.20 mM. As can be seen in Figure 32.B, 32.C and 32.D, increasing the initial amount of seeds led to progressively smaller nanoparticles, in agreement with the hypothesis of a seeded-growth mechanism and the results reported by Kim *et al.*<sup>42</sup>

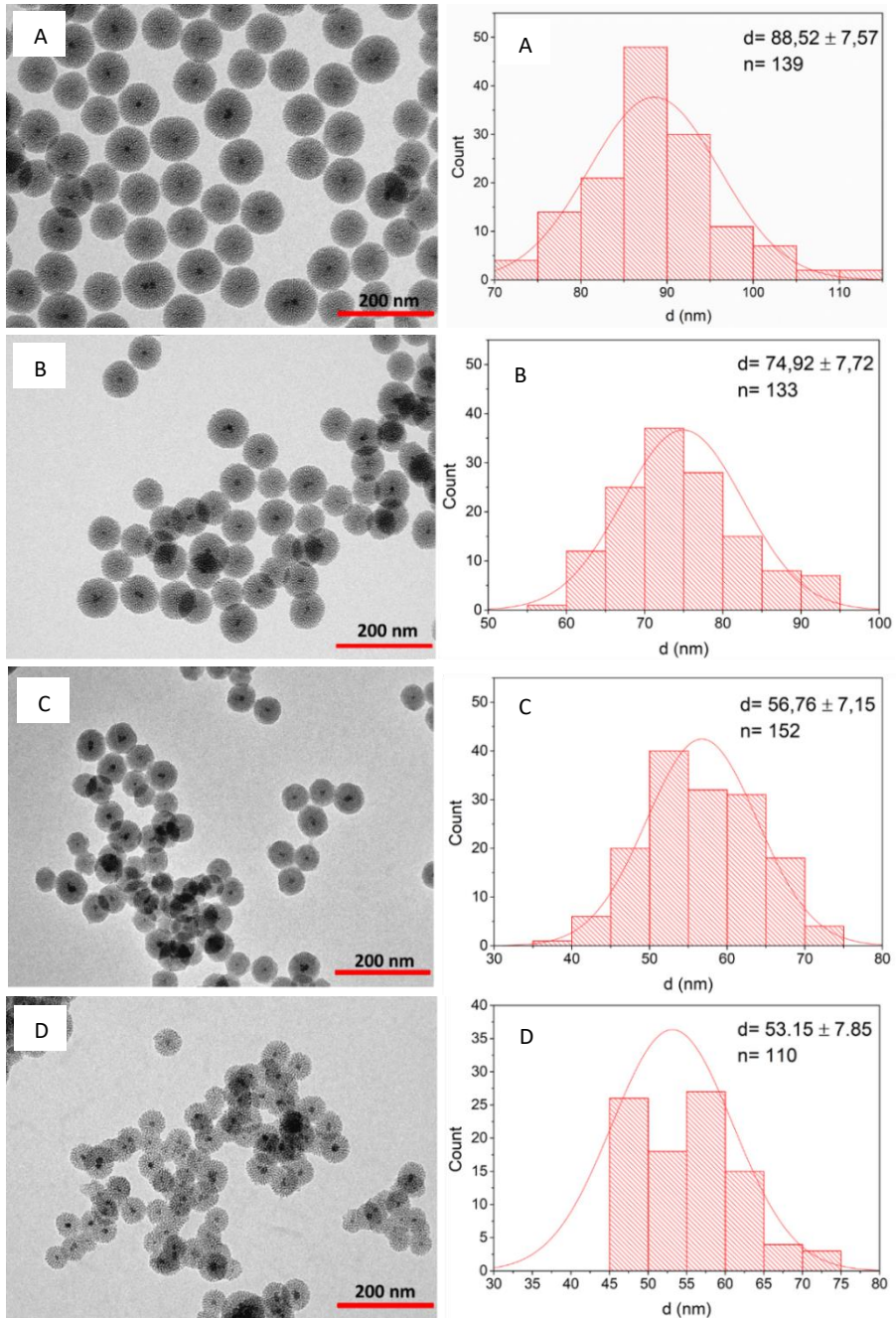


**Figure 32:** Representative TEM micrographs of the core-shell M-MSNs obtained using an initial concentration of magnetic seeds corresponding to (A) 0.44 mM, (B) 0.73 mM, (C) 1.47 mM and (D) 2.20 mM.

The TEM micrographs also revealed that, as the nanoparticles became smaller, aggregation between them increased. This would be consistent with a large number of nucleation sites in close proximity during the growth of the silica shell, leading to the formation of clusters and chains. Additionally, smaller nanoparticles are also more reactive, which would facilitate their aggregation when the concentration of nucleation sites is increased. However, aggregation is also likely to occur during the calcination of the synthesised nanoparticles or during the preparation and measurement of the TEM samples (evaporation of solvent and application of ultra-high vacuum inside the microscope), therefore a direct link between the number of seeds and nanoparticle aggregation could not be established only based on TEM observations. DLS analysis was used as an alternative technique, as will be discussed in section 4.3.4.4.

#### Comparison with the predictions of the semi-empirical model

The average size of the resulting core-shell M-MSNs was determined by TEM analysis and compared with the sizes predicted by the semi-empirical model. The obtained experimental results perfectly matched those predicted by the model, as shown in Figure 33.

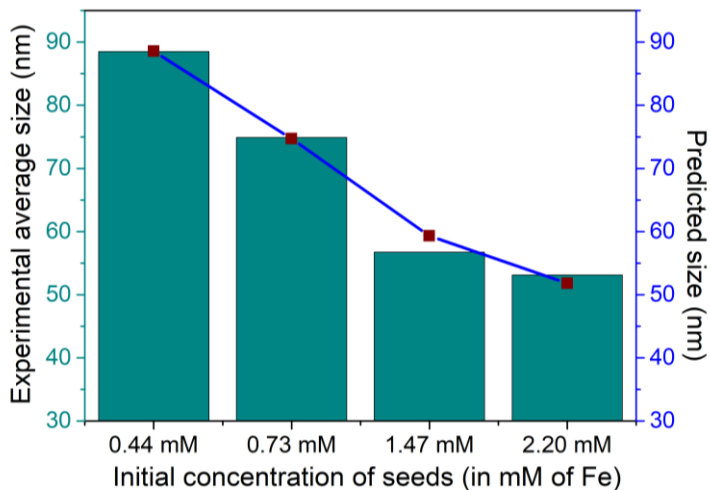


**Figure 33:** Comparison between the experimental average size of the core-shell M-MSNs determined by TEM (bars) and the sizes predicted by the semi-empirical model (line).

The close proximity between these values suggested that the developed model had a significant predicting potential despite the rough approximations and simplifications adopted, providing quantitative information that could be useful to understand the formation of the core-shell M-MSNs.

#### 4.3.4.4. Time of reaction

As previously mentioned in this chapter, the formation of MSNs can take place in just a few minutes when working under alkaline conditions.<sup>33,62</sup> This is in marked contrast with the several hours of reaction reported in many synthetic protocols, including those used as a reference for the synthesis of our core-shell M-MSNs.<sup>42,60,61,66</sup>

Although *in situ* characterization techniques would be desirable in order to study the formation of the nanoparticles, we applied dynamic light scattering (DLS) in an attempt to monitor the growth of the nanoparticles during the reaction. In order to do this, several aliquots were directly taken from the reaction at different time points. In an attempt to reduce the rate of reaction and prevent nanoparticle aggregation, the aliquots were placed into an ice bath previous to the DLS measurements.

#### Initial stage of the reaction

The first experiment was conducted using an intermediate concentration of magnetic seeds (0.73 mM of Fe), which according to the semi-empirical model would lead to the formation of core-shell M-MSNs with a diameter around 75 nm. Following the standard protocol developed, the stirring rate was increased to 850 rpm after the addition of the silica precursor. A first aliquot was immediately taken after this (time 0). The sample presented certain turbidity, which was attributed to the presence of small oily droplets from the oil-in-water emulsion. A second aliquot was taken 2 minutes after the addition of TEOS, when the stirring rate was reduced to 350 rpm. The turbidity of this sample was significantly lower, suggesting that the oily droplets of TEOS had already been consumed. Finally, a third aliquot was taken 10 minutes after the addition of TEOS.

As can be seen in Figure 34, each aliquot gave a distinctive population with different sizes. The first two aliquots gave a Z-average size over 200 nm, well above the expected size for the core-shell M-MSNs prepared in this experiment. This was attributed to the heterogeneous mixture of emulsion droplets, micellar structures and magnetic seeds coexisting during the first minutes of reaction. Conversely, the sample taken after 10 minutes of reaction showed a single and narrow size distribution, indicating that the species present in solution presented a highly uniform size. Interestingly, the Z-average size of this population was 84 nm, a value compatible with the hydrodynamic size expected for the core-shell M-MSNs.

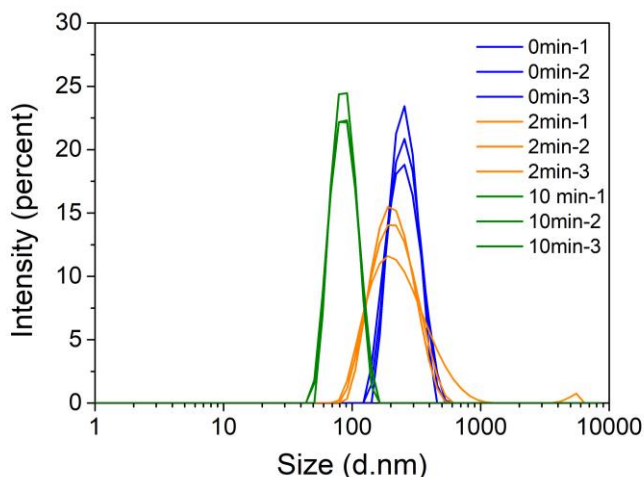


**Figure 34:** Intensity-weighted hydrodynamic size distributions for the aliquots taken at 0, 2 and 10 minutes after the addition of TEOS.

The aliquot taken 10 minutes after the addition of the silica precursor was analysed using TEM microscopy, which confirmed that core-shell M-MSNs with a well-developed morphology were already formed, as shown in Figure 35. The mesoporous structure of the nanoparticles was blurry compared to the images obtained from calcined samples, which was attributed to the presence of CTAB and other reacting species. Moreover, the nanoparticles were highly aggregated, with bridges joining different nanoparticles. This is consistent with the presence of reactive species in the reaction mixture that facilitate the aggregation of nanoparticles during the preparation of the sample for TEM analysis. The

nanoparticles presented an average size around 60 nm, suggesting that the growing of the silica shell was still not complete after 10 minutes of reaction. However, these results were highly informative about the formation kinetics of the core-shell M-MSNs, suggesting that the initial heterogeneous mixture of reaction components rapidly evolves into a stable suspension of uniformly-sized nanoparticles.

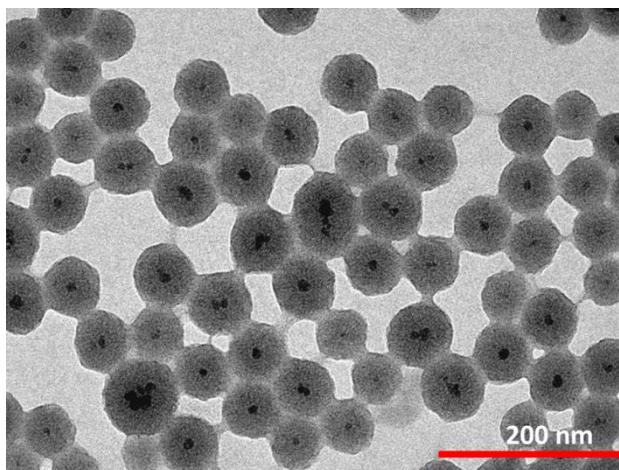


**Figure 35:** TEM micrograph of the aliquot taken 10 minutes after the addition of TEOS, confirming that the formation of the core-shell structure occurs during the first minutes of reaction.

### Evolution of the nanoparticle size with time

Additional aliquots were taken at 34, 60, 120 and 180 minutes after the addition of TEOS in order to monitor the evolution of the reaction with time. Table 2 presents the Z-average size and PDI values obtained. After an initial reduction in the Z-average size, the size of the nanoparticles starts to increase, indicating the existence of an inflexion point after the third aliquot (10 minutes). On the other hand, the analysis of the polydispersity index (PDI), a dimensionless parameter used to describe the broadness of the particle size distribution, revealed that between the first and second hour of reaction there is a significant increase of polydispersity. The increase of polydispersity is also accompanied by a significant increase in the size of the main population, reaching a maximum Z-average value of 773 nm after 3 h of reaction. Both the increase of PDI and Z-average values are indicative of the formation of aggregates during the reaction.

**Table 2:** Z-average and PDI values obtained for the aliquots taken at different time points during the reaction.

Aliquot	Time point (min)	Z-average (nm)	PDI
1	0	244.6	0.045
2	2	203.4	0.167
3	10	84.2	0.022
4	34	92.73	0.018
5	60	107.6	0.039
6	120	246.8	0.212
7	180	773.0	0.434

Figure 36 shows the intensity-weighted size distributions of the aliquots taken after 1 h, 2 h and 3 h of reaction. The broadening of the size distribution with time can be clearly observed, eventually splitting into three different peaks for the aliquot taken after 3 h. Increase of polydispersity also manifested in an increase of turbidity in the samples, as shown in Figure 37. Note that all the samples were stable apart from the aliquot taken after 3 h, in which phase separation was observed due to the sedimentation of large aggregates.

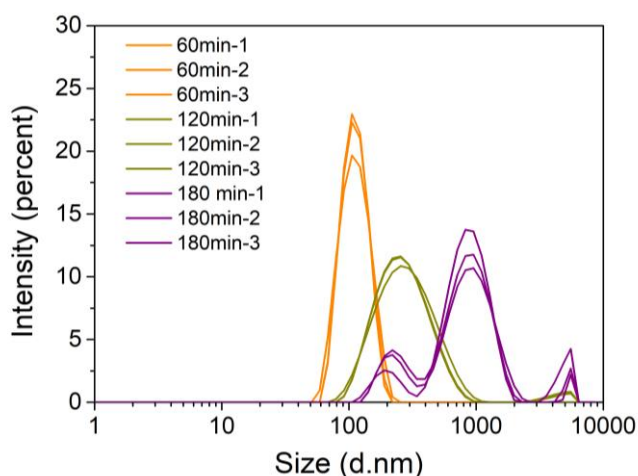


**Figure 36:** Intensity-weighted hydrodynamic size distributions for the aliquots taken at 60, 120 and 180 minutes after the addition of TEOS.

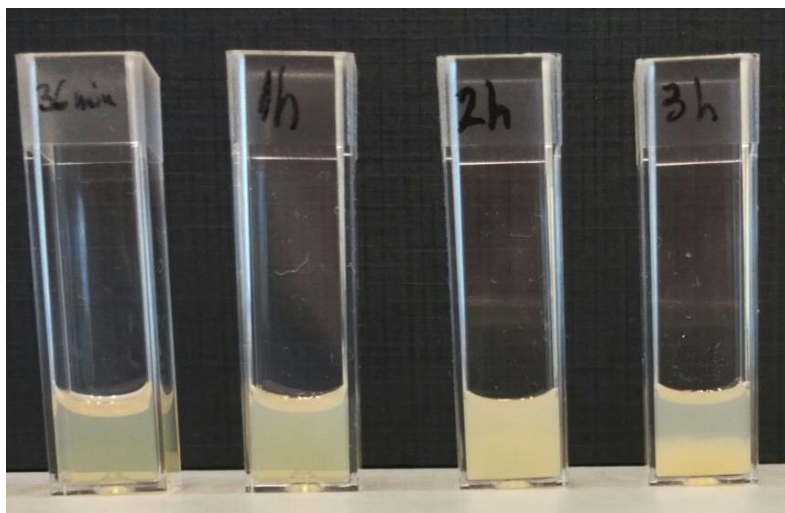


**Figure 37:** Increase of turbidity experienced by the aliquots as the time of reaction increases. Note the phase separation experienced in the aliquot taken 3 h after addition of TEOS.

Based on these results, it was concluded that the reaction time for the synthetic protocol developed should not exceed 1 h of reaction. Additionally, it was confirmed that aggregation is an important factor to consider in the synthesis of the core-shell M-MSNs. Understanding the processes that lead to the formation of aggregates and identifying those experimental factors that influence them, is therefore essential in order to obtain monodisperse and uniform core-shell M-MSNs.

#### Initial concentration of magnetic seeds

DLS analysis proved to be an efficient technique to monitor the appearance of aggregation in the synthesis of the core-shell M-MSNs. Thus, we decided to investigate if the initial concentration of magnetic seeds used in the reaction could influence the formation of aggregates, as suggested by the TEM observations presented before. The working hypothesis was that the presence of a large number of nucleation sites in the initial reaction mixture would facilitate the intergrowth of nanoparticles and the formation of clusters and chains.



As can be seen in Figure 38.A, the nanoparticle size distribution for the sample synthesised with a lower initial concentration of seeds barely changed during the first hour of reaction. Conversely, a significant broadening of the nanoparticle size distribution was observed for the sample prepared with a higher concentration of magnetic seeds (Figure 38.B), indicating that aggregation was starting to develop in this sample during the first hour of reaction.

It is important to highlight that both samples display a narrow and well-defined size distribution around 100 nm after just 10-15 minutes of reaction, again suggesting that the growth of the mesoporous silica shell around the magnetic seeds occurs during the first minutes of reaction. This would explain the paramount importance of stirring during the first minutes of reaction, which are critical for the assembly of the silica-coated micelles around the magnetic seeds and the formation of the mesoporous silica shell. Once the main structure of the core-shell M-MSNs is formed, the size of the resulting nanoparticles barely changes. However, if a threshold reaction time is exceeded, aggregation between particles starts to develop, a process that seems to be determined by the initial amount of seeds used in the reaction.

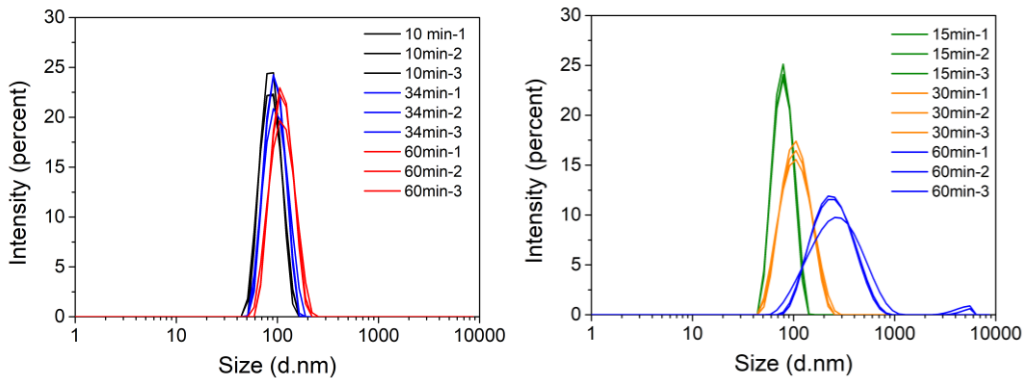


**Figure 38:** Evolution of the distribution of nanoparticle sizes during the first hour of reaction for core-shell M-MSNs synthesised with a lower (left) and higher (right) initial concentration of magnetic seeds.

## 4.4. Conclusions

In this chapter, the synthesis of monodisperse core-shell M-MSNs has been thoroughly investigated. Through a systematic study of the different reaction parameters involved in the reaction, a reliable and reproducible synthetic protocol has been developed. The obtained results have shown that the formation of this type of nanoparticles is affected by multiple parameters, which have to be optimized in order to obtain high-quality nanoparticles with well-defined physico-chemical properties.

Evaluation of the possible mechanisms involved in the reaction and application of a reference model helped us to understand and predict the effect that different reaction parameters have on the reaction. Moreover, the quantitative prediction of the nanoparticle size and yield of the synthesis provided by the model was in good agreement with the experimental results, strongly suggesting that the formation of the core-shell M-MSNs occurs through the assembly of small silica-coated micelles around single magnetic seeds, the hypothesis upon which the model was developed. This mechanism is consistent with the effects observed during the optimization of the synthesis:

- The first minutes of reaction are critical, which require fast stirring rates. This favours the growth of the mesoporous silica shell around single magnetic seeds and prevents the formation of nanoparticle clusters. Then, slower stirring rates are required for the development of an ordered mesoporous silica structure.
- The initial amount of magnetic seeds determines the final size of the core-shell M-MSNs. When the amount of seeds is increased, the amount of silica-coated micelles available per nanoparticle decreases, leading to smaller core-shell M-MSNs.

Finally, it has been shown that DLS analysis can provide valuable information about the formation of the nanoparticles and the appearance of aggregation, although it presents some limitations when heterogeneous mixtures are analysed. Reaction times under 1 h are usually required in order to avoid the formation of aggregates, a process that is also highly influenced by the initial amount of seeds used in the reaction.

## 4.5. References

- (1) Sing, K. S. W.; Everett, D. H.; Haul, R. A. W.; Moscou, L.; Pierotti, R. A.; Rouqu rol, J.; Siemieniewska, T. *Pure Appl. Chem.* **1985**, *57* (4), 603–619.
- (2) Kresge, C. T.; Leonowicz, M. E.; Roth, W. J.; Vartuli, J. C.; Beck, J. S. *Nature* **1992**, *359* (22), 710–712.
- (3) Beck, J. S.; Vartuli, J. C.; Roth, W. J.; Leonowicz, M. E.; Kresge, C. T.; Schmitt, K. D.; Chu, C. T.-W.; Olson, D. H.; Sheppard, E. W.; McCullen, S. B.; Higgins, J. B.; Schlenker, J. L. *J. Am. Chem. Soc.* **1992**, No. 14, 10834–10843.
- (4) Di Renzo, F.; Cambon, H.; Dutartre, R. *Microporous Mater.* **1997**, *10* (4–6), 283–286.
- (5) Deng, Y.; Cai, Y.; Sun, Z.; Zhao, D. *Chem. Phys. Lett.* **2011**, *510* (1–3), 1–13.
- (6) Igarashi, M.; Matsumoto, T.; Yagihashi, F.; Yamashita, H.; Ohhara, T.; Hanashima, T.; Nakao, A.; Moyoshi, T.; Sato, K.; Shimada, S. *Nat. Commun.* **2017**, *8* (140), 1–8.
- (7) Swaddle, T. W.; Selerno, J.; Tregloan, P. A. *Chem. Soc. Rev.* **1994**, *23* (5), 319–325.
- (8) Iler, R. K. *The Chemistry of Silica*; 1979.
- (9) Bergna, H. E. *The Colloid Chemistry of Silica*; Bergna, H. E., Ed.; Washington DC, 1994; Vol. 19.
- (10) Solovyov, L. A. *Chem. Soc. Rev.* **2013**, *42* (9), 3708–3720.
- (11) Israelachvili, J. N. *Intermolecular and Surface Forces*, Third.; 2011.
- (12) Edler, K. J. Template Induction of Supramolecular Structure: Synthesis and Characterisation of the Mesoporous Molecular Sieve, MCM-41, 1997.
- (13) Raman, N. K.; Anderson, M. T.; Brinker, C. J. *Chem. Mater.* **1996**, *8* (8), 1682–1701.
- (14) Landry, C. C.; Tolbert, S. H.; Gallis, K. W.; Monnier, A.; Stucky, G. D.; Norby, P.; Hanson, J. C. *Chem. Mater.* **2001**, *13* (5), 1600–1608.
- (15) Anderson, M. T.; Martin, J. E.; Odinek, J. G.; Newcomer, P. P. *Chem. Mater.* **1998**, *10* (1), 311–321.
- (16) Edler, K. J. In *Porous Materials*; Bruce, D. W., O’Hare, D., Walton, R. I., Eds.; Wiley, 2011; pp 69–145.
- (17) Zhuravlev, L. T. *Colloids Surfaces A Physicochem. Eng. Asp.* **2000**, *173* (1–3), 1–38.
- (18) Yang, H.; Coombs, N.; Ozin, G. A. *Nature* **1997**, *386* (6626), 692–695.
- (19) Huo, Q.; Feng, J.; Sch uth, F.; Stucky, G. D. *Chem. Mater.* **1997**, *9* (1), 14–17.
- (20) Stober, W.; Fink, A. *J. Colloid Interface Sci.* **1968**, *26*, 62–69.
- (21) Grun, M.; Lauer, I.; Unger, K. K. *Adv. Mater.* **1997**, *9* (3), 254–257.
- (22) Grun, M.; Unger, K. K.; Matsumoto, A.; Tsutsumi, K. *Microporous Mesoporous Mater.* **1999**, *27*, 207–216.
- (23) Buchel, G.; Grun, M.; Unger, K. K.; Matsumoto, A.; Tsutsumi, K. *Supramol.*

- Sci.* **1998**, *5* (3–4), 253–259.
- (24) Grun, M.; Buchel, G.; Kumar, D.; Schumacher, K.; Bidlingmaier, B.; Unger, K. *K. Stud. Surf. Sci. Catal.* **2000**, *128* (5), 155–165.
- (25) Pauwels, B.; Van Tendeloo, G.; Thoelen, C.; Van Rhijn, W.; Jacobs, P. A. *Adv. Mater.* **2001**, *41* (17), 1317–1320.
- (26) Tendeloo, G. Van; Lebedeb, O. I.; Collart, O.; Cool, P.; Vansant, E. F. *J. Phys. Condens. Matter* **2003**, *15*, S3037–S3046.
- (27) Chen, Q.; Han, L.; Gao, C.; Che, S. *Microporous Mesoporous Mater.* **2010**, *128* (1–3), 203–212.
- (28) Schumacher, K.; Renker, S.; Unger, K. K.; Ulrich, R.; Du Chesne, A.; Spiess, H. W.; Wiesner, U. In *Studies in Surface Science and Catalysis 129*; 2000; pp 1–6.
- (29) Yano, K.; Fukushima, Y. *J. Mater. Chem.* **2003**, *13* (10), 2577–2581.
- (30) Luo, Q.; Li, L.; Xue, Z.; Zhao, D. In *Studies in Surface Science and Catalysis 129*; 2000; pp 37–43.
- (31) Yano, K.; Fukushima, Y. *J. Mater. Chem.* **2004**, *14* (10), 1579.
- (32) Yano, K.; Suzuki, N.; Akimoto, Y.; Fukushima, Y. *Bull. Chem. Soc. Jpn.* **2002**, *75* (9), 1977–1982.
- (33) Fowler, C. E.; Khushalani, D.; Lebeau, B.; Mann, S. *Adv. Mater.* **2001**, *13* (9), 649–652.
- (34) Cai, Q.; Luo, Z. S.; Pang, W. Q.; Fan, Y. W.; Chen, X. H.; Cui, F. Z. *Chem. Mater.* **2001**, *13* (2), 258–263.
- (35) Sadasivan, S.; Khushalani, D.; Mann, S. *J. Mater. Chem.* **2003**, *13* (5), 1023–1029.
- (36) Nooney, R. I.; Thirunavukkarasu, D.; Yimei, C.; Josephs, R.; Ostafin, A. E. *Chem. Mater.* **2002**, *14* (11), 4721–4728.
- (37) Mukherjee, P.; Patra, C. R.; Kumar, R.; Sastry, M. *PhysChemComm* **2001**, *4*, 1–2.
- (38) Cai, W.; Zhang, Y.; Jia, J.; Zhang, L. *Appl. Phys. Lett.* **1998**, *73* (19), 2709–2711.
- (39) Mulukutla, R. S.; Asakura, K.; Kogure, T.; Namba, S.; Iwasawa, Y. *Phys. Chem. Chem. Phys.* **1999**, *1* (8), 2027–2032.
- (40) Nooney, R. I.; Dhanasekaran, T.; Chen, Y.; Josephs, R.; Ostafin, A. E. *Adv. Mater.* **2002**, *14* (7), 529–532.
- (41) Nooney, R. I.; Thirunavukkarasu, D.; Chen, Y.; Josephs, R.; Ostafin, A. E. *Langmuir* **2003**, *19* (18), 7628–7637.
- (42) Kim, J.; Kim, H. S.; Lee, N.; Kim, T.; Kim, H.; Yu, T.; Song, I. C.; Moon, W. K.; Hyeon, T. *Angew. Chem. Int. Ed.* **2008**, *47* (44), 8438–8441.
- (43) Vartuli, J. C.; Kresge, C. T.; Leonowicz, M. E.; Chu, A. S.; McCullen, S. B.; Johnson, I. D.; Sheppard, E. W. *Chem. Mater.* **1994**, *6* (11), 2070–2077.
- (44) Vartuli, J. C.; Schmitt, K. D.; Kresge, C. T.; Roth, W. J.; Leonowicz, M. E.; McCullen, S. B.; Hellring, S. D.; Beck, J. S.; Schlenker, J. L.; Olson, D. H.;

- Sheppard, E. W. *Chem. Mater.* **1994**, *6* (12), 2317–2326.
- (45) Chen, C.-Y.; Burkett, S. L.; Li, H.-X.; Davis, M. E. *Microporous Mater.* **1993**, *2*, 27–34.
- (46) Edler, K. J. *Aust. J. Chem.* **2005**, *58*, 627–643.
- (47) Monnier, A.; Schuth, F.; Huo, Q.; Kumar, D.; Margolese, D.; Maxwell, R. S.; Stucky, G. D.; Krishnamurty, M.; Petroff, P.; Firouzi, A.; Janicke, M.; Chmelka, B. F. *Science (80-. )*. **1993**, *261* (5126), 1299–1303.
- (48) Firouzi, A.; Kumar, D.; Bull, L. M.; Besier, T.; Sieger, P.; Huo, Q.; Walker, S. A.; Zasadzinski, J. A.; Glinka, C.; Nicol, J.; Margolese, D.; Stucky, G. D.; Chmelka, B. F. *Science (80-. )*. **1995**, *267* (5201), 1138–1143.
- (49) Ågren, P.; Linden, M.; Rosenholm, J. B.; Schwarzenbacher, R.; Kriechbaum, M.; Amenitsch, H.; Laggner, P.; Blanchard, J.; Schuth, F. *J. Phys. Chem. B* **1999**, *103* (29), 5943–5948.
- (50) Gallis, K. W.; Landry, C. C. *Chem. Mater.* **1997**, *9* (10), 2035–2038.
- (51) Baute, D.; Frydman, V.; Zimmermann, H.; Kababya, S.; Goldfarb, D. *J. Phys. Chem. B* **2005**, *109* (16), 7807–7816.
- (52) Huo, Q.; Margolese, D. I.; Ciesla, U.; Feng, P.; Gier, T. E.; Sieger, P.; Leon, R.; Petroff, P. M.; Schuth, F.; Stucky, G. D. *Nature* **1994**, *368*, 317–321.
- (53) Huo, Q.; Margolese, D. I.; Ciesla, U.; Demuth, D. G.; Feng, P.; Gier, T. E.; Sieger, P.; Firouzi, A.; Chmelka, B. F.; Schuth, F.; Stucky, G. D. *Chem. Mater.* **1994**, *6* (8), 1176–1191.
- (54) Sadasivan, S.; Fowler, C. E.; Khushalani, D.; Mann, S. *Angew. Chemie - Int. Ed.* **2002**, *41* (12), 2151–2153.
- (55) Philipse, A. In *Fundamentals of Interface and Colloid Science-Volume IV: Particulate Colloids*; Elsevier, 2005; Vol. IV.
- (56) Blaaderen, A. Van; Vrij, A. In *The Colloid Chemistry of Silica*; Bergna, H. E., Ed.; 1994; pp 83–111.
- (57) LaMer, V. K.; Dinegar, R. H. *J. Am. Chem. Soc.* **1950**, *72* (11), 4847–4854.
- (58) Wang, Y.; Gu, H. *Adv. Mater.* **2014**, 1–10.
- (59) Fan, H.; Yang, K.; Boye, D. M.; Sigmon, T.; Malloy, K. J.; Xu, H.; López, G. P.; Brinker, C. J. *Sci. Reports* **2004**, *304* (5670), 567–571.
- (60) Nyalosaso, J. L.; Rascol, E.; Pisani, C.; Dorandeu, C.; Dumail, X.; Maynadier, M.; Gary-Bobo, M.; Kee Him, J. L.; Bron, P.; Garcia, M.; Devoisselle, J. M.; Prat, O.; Guari, Y.; Charnay, C.; Chopineau, J. *RSC Adv.* **2016**, *6* (62), 57275–57283.
- (61) Zhang, J.; Li, X.; Rosenholm, J. M.; Gu, H. *J. Colloid Interface Sci.* **2011**, *361* (1), 16–24.
- (62) Suteewong, T.; Sai, H.; Lee, J.; Bradbury, M.; Hyeon, T.; Gruner, S. M.; Wiesner, U. *J. Mater. Chem.* **2010**, *20* (36), 7807.
- (63) Liong, M.; Lu, J.; Kovichich, M.; Xia, T.; Ruehm, S. G.; Nel, A. E.; Tamanoi, F.; Zink, J. I. *ACS Nano* **2008**, *2* (5), 889–896.

- (64) Zhang, J.; Rosenholm, J. M.; Gu, H. *ChemPhysChem* **2012**, *13* (8), 2016–2019.
- (65) Zhang, L.; Wang, Y.; Tang, Y.; Jiao, Z.; Xie, C.; Zhang, H.; Gu, P.; Wei, X.; Yang, G.-Y.; Gu, H.; Zhang, C. *Nanoscale* **2013**, *5* (10), 4506–4516.
- (66) Ye, F.; Laurent, S.; Fornara, A.; Astolfi, L.; Qin, J.; Roch, A.; Martini, A.; Toprak, M. S.; Muller, R. N.; Muhammed, M. *Contrast Media Mol. Imaging* **2012**, *7* (5), 460–468.
- (67) Moros, M.; Pelaz, B.; López-Larrubia, P.; García-Martin, M. L.; Grazú, V.; de la Fuente, J. M. *Nanoscale* **2010**, *2* (9), 1746–1755.
- (68) Lyklema, J. *Fundamentals of Interface and Colloid Science-Volume IV: Particulate Colloids*; Elsevier, Ed.; 2005.
- (69) Yi, Z.; Dumée, L. F.; Garvey, C. J.; Feng, C.; She, F.; Rookes, J. E.; Mudie, S.; Cahill, D. M.; Kong, L. *Langmuir* **2015**, *31* (30), 8478–8487.
- (70) Mata, J.; Varade, D.; Bahadur, P. *Thermochim. Acta* **2005**, *428* (1–2), 147–155.
- (71) Ekwall, P.; Mandell, L.; Solyom, P. *J. Colloid Interface Sci.* **1971**, *35* (4), 519–528.
- (72) Helgeson, M. E.; Hodgdon, T. K.; Kaler, E. W.; Wagner, N. J. *J. Colloid Interface Sci.* **2010**, *349* (1), 1–12.
- (73) Kuperkar, K.; Abezgauz, L.; Prasad, K.; Bahadur, P. *J. Surfactants Deterg.* **2010**, *13* (3), 293–303.
- (74) Delsanti, M.; Moussaid, A.; Munch, J. P. *Journal of Colloid And Interface Science.* 1993, pp 285–290.
- (75) Nazir, N.; Ahanger, M. S.; Akbar, A. *J. Dispers. Sci. Technol.* **2009**, *30* (1), 51–55.
- (76) Goyal, P. S.; Dasannacharya, B. A.; Kelkar, V. K.; Manohar, C.; Rao, K. S.; Valaulikar, B. S. *Phys. B* **1991**, *174*, 196–199.
- (77) Van Blaaderen, A.; Van Geest, J.; Vrij, A. *J. Colloid Interface Sci.* **1992**, *154* (2), 481–501.
- (78) Znezevic, N. Z.; Slowing, I. I.; Lin, V. S.-Y. *Chem Plus Chem* **2012**, *77*, 48–55.
- (79) Brinker, C. J. *J. Non. Cryst. Solids* **1988**, *100*, 31–50.
- (80) Lin, R.; Carlström, G.; Dat Pham, Q.; Anderson, M. W.; Topgaard, D.; Edler, K. J.; Alfredsson, V. *J. Phys. Chem. C* **2016**, *120* (7), 3814–3821.
- (81) Brinker, C. J.; Scherer, G. W. *Sol-Gel Science: The Physics and Chemistry of Sol-Gel Processing*; Academic Press, 1990.
- (82) Kim, J.; Lee, J. E.; Lee, J.; Yu, J. H.; Kim, B. C.; An, K.; Hwang, Y.; Shin, C.-H.; Park, J.-G.; Kim, J.; Hyeon, T. *J. Am. Chem. Soc.* **2006**, *128* (3), 688–689.
- (83) Suteewong, T.; Sai, H.; Hovden, R.; Muller, D.; Bradbury, M. S.; Gruner, S. M.; Wiesner, U. *Science (80- )*. **2013**, *340*, 337–341.
- (84) Stucky, G. D.; Monnier, A.; Schuth, F.; Huo, Q.; Margolese, D.; Kumar, D.; Krishnamurty, M.; Petroff, P.; Firouzi, A.; Janicke, M.; Chmelka, B. F. *Mol. Cryst. Liq. Cryst.* **1994**, *240* (1), 187–200.

- 
- (85) Edler, K. J.; Dougherty, J.; Durand, R.; Iton, L.; Kirton, G.; Lockhart, G.; Wang, Z.; Withers, R.; White, J. W. *Colloids Surfaces A Physicochem. Eng. Asp.* **1995**, *102* (C), 213–230.
- (86) Liu, S.; Cool, P.; Collart, O.; Voort, P. Van Der; Vansant, E. F.; Lebedev, O. I.; Tendeloo, G. Van; Jiang, M. *J. Phys. Chem. B* **2003**, *107* (38), 10405–10411.
- (87) Yu, M.; Zhou, L.; Zhang, J.; Yuan, P.; Thorn, P.; Gu, W.; Yu, C. *J. Colloid Interface Sci.* **2012**, *376*, 67–75.
- (88) Möller, K.; Kobler, J.; Bein, T. *Adv. Funct. Mater.* **2007**, *17* (4), 605–612.
- (89) Lindén, M.; Schunk, S. A.; Schüth, F. *Angew. Chemie - Int. Ed.* **1998**, *37* (6), 821–823.
- (90) Edler, K. J.; White, J. W. *J. Mater. Chem.* **1999**, *9* (10), 2611–2615.
- (91) Li, Y.; Bastakoti, B. P.; Imura, M.; Tang, J.; Aldalbahi, A.; Torad, N. L.; Yamauchi, Y. *Chem. - A Eur. J.* **2015**, *21* (17), 6375–6380.
- (92) Lebedev, O. I.; Tendeloo, G. Van; Collart, O.; Cool, P.; Vansant, E. F. *Solid State Sci.* **2004**, *6*, 489–498.
- (93) Ng, J. B. S.; Vasiliev, P. O.; Bergström, L. *Microporous Mesoporous Mater.* **2008**, *112* (1–3), 589–596.
- (94) Wang, J. G.; Xiao, Q.; Zhou, H. J.; Sun, P. C.; Ding, D. T.; Chen, T. H. *J. Colloid Interface Sci.* **2008**, *323* (2), 332–337.
- (95) *Giant Micelles: Properties and Applications*; Zana, R., Kaler, E. W., Eds.; CRC Press: Boca Raton, 2007; Vol. 140.
- (96) Jensen, G. V.; Lund, R.; Gummel, J.; Narayanan, T.; Pedersen, J. S. *Angew. Chemie - Int. Ed.* **2014**, *53* (43), 11524–11528.
- (97) Pérez-Sánchez, G.; Gomes, J. R. B.; Jorge, M. *Langmuir* **2013**, *29* (7), 2387–2396.
- (98) Johnson, C. S.; Gabriel, D. A. *Laser Light Scattering*; Dover: Florida, 1981.
- (99) Munson, B. R.; Young, D. F.; Okiishi, T. H.; Huebsch, W. W. *Fundamentals of Fluid Mechanics*, Sixth Edit.; Wiley.
- (100) Liz-Marzán, L. M.; Giersig, M.; Mulvaney, P. *Langmuir* **1996**, *12* (18), 4329–4335.
- (101) Sanz-Ortiz, M. N.; Sentosun, K.; Bals, S.; Liz-Marzán, L. M. *ACS Nano* **2015**, *9* (10), 10489–10497.
- (102) Sang, M. C.; Lee, M.; Kim, W. S. *J. Colloid Interface Sci.* **2005**, *286* (2), 536–542.
- (103) Chou, K. Sen; Chen, C. C. *Ceram. Int.* **2008**, *34* (7), 1623–1627.





**Chapter 5:**

***Structural characterization of core-shell  
magnetic mesoporous silica nanoparticles***



## 5.1. Introduction

The study of the mesostructure and morphology of the core-shell M-MSNs is fundamental in order to determine their properties and potential applications. Moreover, to understand how the mesoporous channels are arranged within the silica shell of the nanoparticles could provide valuable information about the formation mechanism of this type of nanoparticles. However, to decipher the mesoporous architecture of the core-shell M-MSNs is a challenging undertaking due to the inherent complexity of their structure.

In this work, several complementary characterization techniques were employed, including powder XRD analysis, nitrogen physisorption analysis, transmission electron microscopy (TEM) and scanning electron microscopy (SEM). An accurate interpretation of the experimental data is crucial in order to obtain meaningful structural parameters such as the average pore-to-pore distance, the pore size distribution (PSD) or the specific surface area and specific pore volume of the material.

The characterization of mesoporous silica materials with well-defined geometries such as the hexagonal MCM-41 or the cubic MCM-48 is well documented.<sup>1-3</sup> However, much less is known about the characterization of mesoporous silica materials with an irregular (but not random) geometry, such as the radial mesoporous channels sometimes found in MSNs. As a result, multiple (and sometimes contradicting) interpretations about the determination of the average pore-to-pore distance or the pore size distribution of this type of materials can be found in the literature.

In an attempt to provide a clear context for the characterization of the core-shell M-MSNs synthesised in this project, a brief introduction is provided in this chapter focusing on the evaluation of XRD patterns and adsorption isotherms. This is followed by the characterization results obtained from our core-shell M-MSNs, which are comprehensively discussed at the end of the chapter.

### 5.1.1. XRD analysis

XRD analysis is a common characterization technique used to investigate the atomic positions within crystalline materials and to determine structural parameters such as the distance and angles between atoms. The technique is based on the scattering of X-rays when interacting with matter, with the peculiarity that the wavelength of X-rays is of the same order of magnitude as common interatomic distances. As a result, if the sample of study presents an ordered arrangement of atoms, the scattered waves will interact through constructive/destructive interferences leading to a characteristic diffraction pattern.<sup>4</sup> The position of the obtained diffraction peaks reflect the distance between “diffracting planes” in the crystal, a relation that is given by the Bragg’s law:

$$n\lambda = 2d_{hkl}\sin\theta \quad (1)$$

where  $n$  is the order of reflection,  $2\theta$  is the angle between the incident and diffracted X-ray beams,  $\lambda$  is the wavelength of the X-ray radiation and  $d_{hkl}$  represents the interplanar spacing for a particular set of equidistant planes, which are characterized by the three  $hkl$  Miller indices.<sup>4</sup> Figure 1 shows a simplified representation of the diffraction phenomenon and its relation with the Bragg’s law.<sup>5</sup>

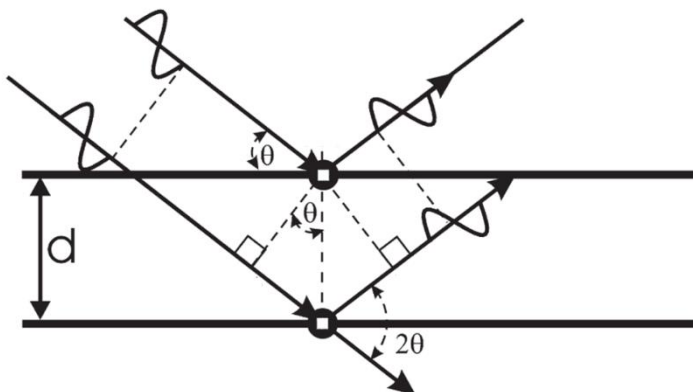


**Figure 1:** Diffraction of X-ray beams by two parallel lattice planes separated by an interplanar spacing  $d$ .  $2\theta$  represents the diffracting angle formed by the incident and diffracted X-ray beams. *Adapted from Powder Diffraction Theory and Practice; Dinnebier, R. E., Billinge, S. J. L., Eds.; RSC Publishing, 2008.*

### 5.1.1.1. Mesoporous silica materials

XRD analysis is also an essential characterization technique for the study of ordered mesostructured materials.<sup>6</sup> Although these type of materials are usually amorphous and do not present a well-defined structure at the atomic level, the periodicity in the arrangement of mesoporous structures is reflected in a characteristic diffraction pattern.<sup>7</sup> However, due to the larger distances between mesopores (compared to interatomic distances) the diffraction peaks appear at much lower angles in agreement with the Bragg's law. Most mesoporous materials are obtained in the form of fine powders/nanoparticles. This is the case of the materials prepared in this work, which are analysed by powder XRD.

Figure 2 shows the diffraction patterns exhibited by three classic members of the M41S family of mesostructured materials: MCM-41, MCM-48 and MCM-50.<sup>1,2</sup> As can be seen in the image, these materials present a small number of broad overlapping diffraction peaks at low angles, in contrast to the sharp diffraction peaks usually obtained in crystalline materials. Despite those limitations, the position and intensities of low-angle diffraction peaks can still provide valuable information about the symmetry and structural order within the mesostructure. MCM-41 materials are probably the most studied members of the M41S family and are characterized by a hexagonal arrangement of unidimensional cylindrical mesopores forming a honeycomb-like structure. The presence of parallel and equally-spaced diffracting planes is responsible for the appearance of a characteristic diffraction pattern. This pattern is shown in Figure 2, in which a main first-order reflection is accompanied by three additional diffraction peaks, which can be indexed as (100), (110), (200) and (210), in agreement with hexagonal arrangement of channels ( $p6mm$  space group).<sup>8,9</sup>

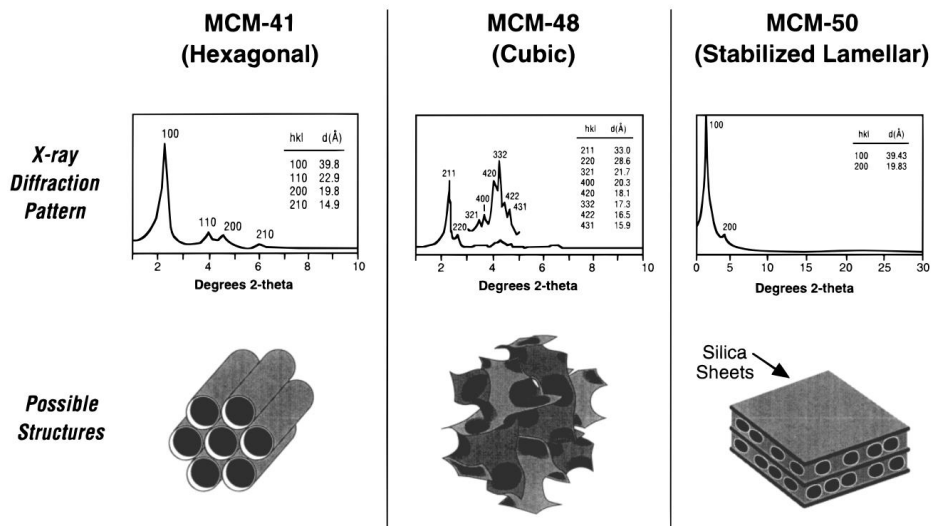


**Figure 2:** X-ray diffraction patterns and proposed structures of MCM-41, MCM-48 and MCM-50. Reprinted with permission from *Chem. Mater.* 1999, 11 (10), 2633–2656.

Many other mesoporous silica materials with well-defined geometries have been synthesised, such as the aforementioned bicontinuous cubic MCM-48 (*la3d* space group)<sup>10</sup> and lamellar MCM-50 (*p2* space group)<sup>1</sup> or the cubic SBA-1 (*Pm3n* space group)<sup>11</sup> and 3D-hexagonal SBA-2 (*P6<sub>3</sub>/mmc* space group)<sup>12</sup>. However, mesoporous materials do not always present a regular arrangement of pores with a well-defined geometry. This is the case of core-shell-type M-MSNs, which are characterized by wormhole-like channels arranged radially from the core to the surface of the nanoparticles.<sup>13–15</sup> Their XRD pattern shows a single and broad diffraction peak, which is indicative of loss of structural order compared to other mesoporous silica materials with well-defined geometries. On the other hand, the presence of a single and intense diffraction peak indicates that there is a periodic pattern that repeats within the mesoporous structure. However, to identify which is the structural motif responsible for this type of pattern and to select the symmetry space group that better describes the geometry of the mesoporous structure is not trivial. In the following section, a brief review about mesoporous materials that exhibit a single diffraction peak is presented in order to provide an adequate context for the structural characterization of our core-shell M-MSNs.

### 5.1.1.2. Mesoporous silica materials with distorted geometry

The appearance of a single and broad diffraction peak (sometimes accompanied by a second, even broader peak) was already reported in the early works about the synthesis of surfactant-templated silica materials,<sup>16–18</sup> being attributed to an inefficient packing of cylindrical pores, as shown in Figure 3. This idea was further developed by the team of Schüth and co-workers, which constructed a computational model to simulate the diffraction patterns of MCM-41 materials with varying degrees of structural order.<sup>19</sup> The authors concluded that the loss of diffraction reflections could be produced by the reduced size of domains with hexagonal symmetry, by disordered mesoporous channels that, on average, are hexagonally arranged or by any other structural motif that presents a specific repeat distance,  $a_0$ .

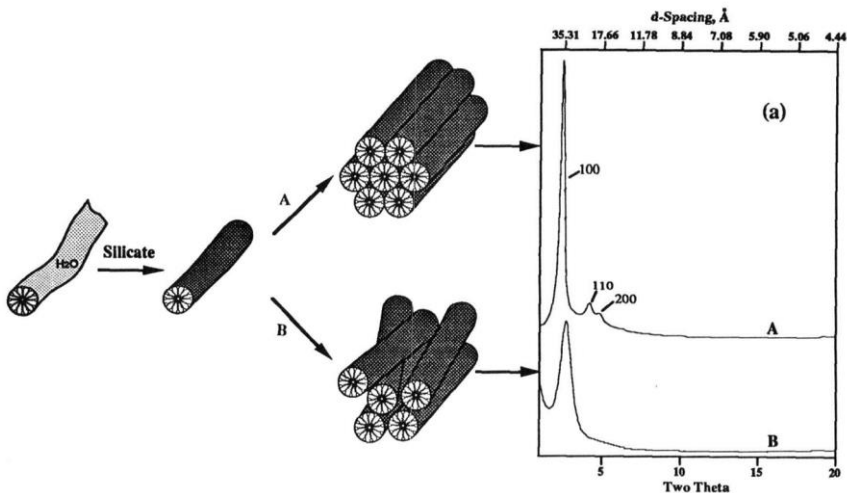


**Figure 3:** Model proposed to explain the loss of diffraction peaks in mesoporous silica materials composed of cylindrical channels. *Reprinted with permission from Mat.Res.Soc.Symp.Proc. 1994, 346, 831–842.*

## 5.1.1.3. Disordered mesoporous silica materials

Another important family of materials is composed of the so-called disordered mesoporous silicas. This type of materials present highly uniform mesopore sizes and large surface areas around 1000 m<sup>2</sup>/g. In contrast to well-ordered mesoporous materials such as MCM-41 or MCM-48, they are characterized by a random arrangement of interconnected mesoporous channels, as shown in Figure 4. Interestingly, they also exhibit broad diffraction peaks, which was interpreted as an indication of short-range structural order. In the case of MSU materials it was proposed that the disordered mesoporous channels would be, on average, hexagonally arranged.<sup>20</sup> In the case of KIT materials, the three broad peaks identified were arbitrarily indexed as (100), (200) and (300), due to the similarity with the XRD pattern of layered materials.<sup>21,22</sup>

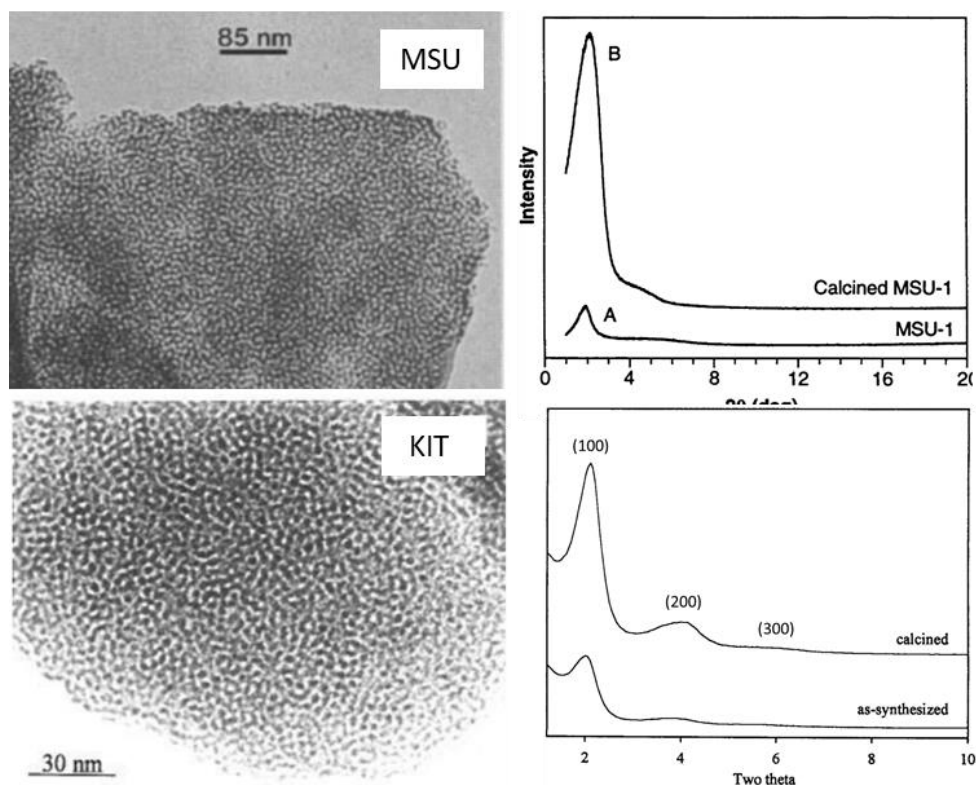


**Figure 4:** TEM micrographs and corresponding XRD patterns of MSU (top) and KIT materials (bottom). Adapted from *Science* 1995, 269, 1242–1244 and *J. Phys. Chem.* 1996, 100 (45), 17718–17721.



#### 5.1.1.4. Spherical particles and loss of structural order

The appearance of a single diffraction peak was also reported in mesoporous silica materials which were synthesised in the form of spherical micrometer and submicrometer-sized particles.<sup>23–26</sup> This was also attributed to a loss of order in the arrangement of the mesoporous channels. Additionally, TEM analysis showed that, in most cases, the mesostructure of this type of particles was composed of a disordered network of mesoporous channels such as that found in KIT and MSU-X materials.

In other cases however, the obtained spherical mesoporous particles presented diffraction patterns that resembled those of MCM-41 materials, as shown in Figure 5.A.<sup>27</sup> However, after calcination the intensity of the diffraction peaks significantly decreased and the (110) and (200) diffraction reflections merged into a single peak. TEM micrographs revealed that the internal mesostructure of this type of particles was composed of elongated channels that were not completely straight, but slightly curved. Moreover, these wormhole-like channels were not parallel as in MCM-41 materials but arranged in a radial distribution, going from the core to the surface of the particles (Figure 5.B). The authors suggested that the particle mesostructure would be composed of a mixture of hexagonally arranged and disordered mesoporous channels. However, this interpretation seemed to contradict the radial distribution of channels observed in the TEM micrographs.

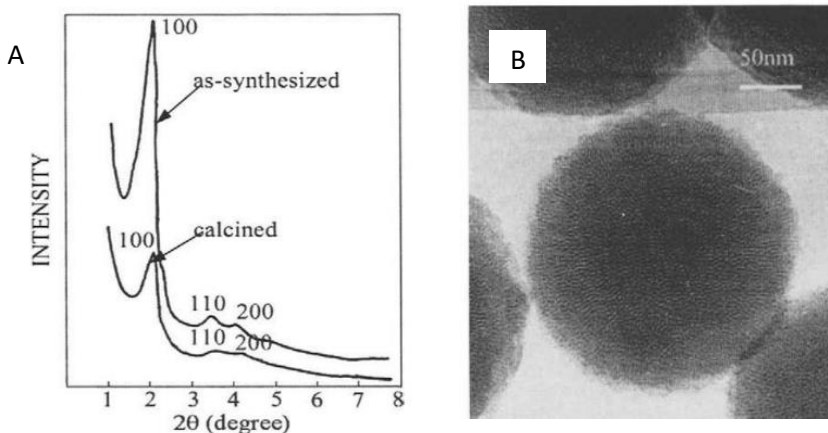


**Figure 5:** TEM micrograph and corresponding XRD patterns of calcined and as-synthesized spherical MSNs with radially aligned wormhole-like channels. *Adapted from Studies in Surface Science and Catalysis 129; 2000; pp 37–43.*

Tendeloo and co-workers also synthesised spherical particles with radially-aligned mesoporous channels.<sup>28</sup> The use of high-resolution TEM (HRTEM) revealed much more details about the internal mesoporous structure of the particles, as shown in Figure 6. Two structural features were clearly identified: the existence of domains with perfectly ordered channels perpendicular to the particle surface and domains with hexagonal symmetry that were visible when the electron beam of the microscope was aligned parallel to the channels. The conclusion drawn from these experiments was that ordering exists at the local level but it is progressively lost on a larger scale. Hexagonal symmetry would be found only when we look at one specific pore and its closest neighbouring pores. However, as we move away from that specific pore, long-range order would be lost due to the spherical symmetry imposed by the shape of the particles, leading to a broadening of the diffraction peaks.

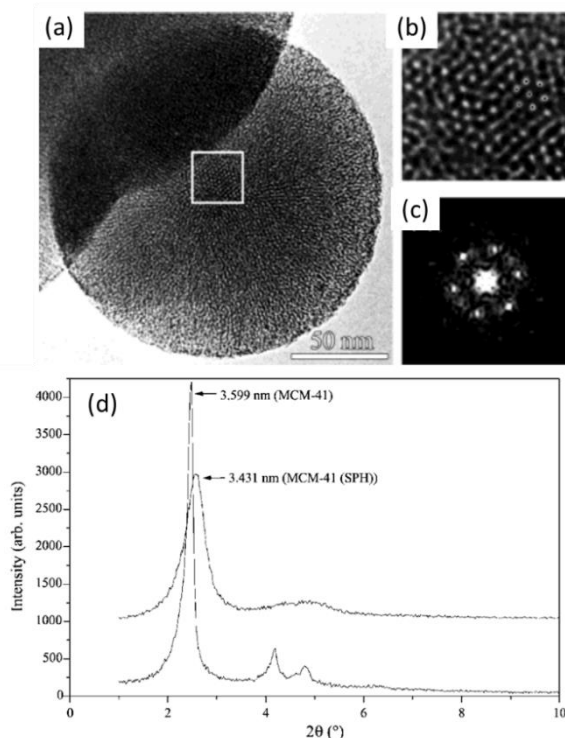


**Figure 6:** a) HRTEM image of a spherical particle with radially-aligned channels (MCM-41 SPH). b) Enlargement of the core corresponding to the white square of (a). c) FFT of (b) showing a hexagonal symmetry. d) XRD patterns of MCM-41 and MCM-41 SPH nanoparticles. *Adapted from Adv. Mater.* 2001, 41 (17), 1317–1320.

### 5.1.1.5. Interpretation of diffraction data in this project

The results obtained by Tendeloo and co-workers implied a relation between the loss of long-range order and the size of the particles.<sup>28</sup> Small particles with higher curvature would present a more disordered mesostructure, leading to diffraction patterns with broader diffraction peaks. On the other hand, large particles with lower curvature would be more likely to present mesoporous channels arranged in a hexagonal distribution, displaying diffraction patterns with sharper peaks and greater hexagonal order.

Taking this idea one step further, the degree of hexagonal order is also expected to vary within the mesostructure of a single nanoparticle, going from a more disordered structure at the core (higher curvature) to a hexagonal-like packing of channels near the nanoparticle surface (less curvature). Overall, this interpretation could explain the origin of the distorted hexagonal symmetry sometimes found in spherical particles with radially-aligned mesopores and the similarities with the diffraction patterns of MCM-41 materials.

Based on the previous observations, several key ideas are highlighted for the interpretation of XRD patterns produced by spherical nanoparticles with radially aligned mesoporous channels:

- The appearance of a diffraction pattern is attributed to short-range order within the structure and should be considered as “an indication of the distance between nearest neighbours, rather than as distances between lattice planes”.<sup>28</sup> Only those domains in which the mesopores are arranged following an ordered periodic pattern will contribute to the formation of the XRD pattern.
- The arrangement of mesopores within the mesoporous structure cannot be represented by a single standard geometry.
- The radial distribution of channels imposes physical restrictions to the development of long-range order, leading to diffraction patterns with a limited number of diffraction peaks.

Interpretation of the diffraction data requires the assumption of a specific geometric model. However, in the case of our core-shell M-MSNs, a single geometry cannot be applied throughout the whole mesoporous structure. The semi-empirical model developed suggests that the mesoporous structure is formed through the assembly of spheroidal silica-coated micelles. Accordingly, the way the silica-coated micelles assemble around the magnetic seeds is expected to determine the geometry of the resulting mesoporous silica structure and the corresponding diffraction pattern.

Two limiting geometries are adopted in this project based on the close packing of uniformly-sized spheres: square packing and hexagonal packing (Figure 7). We hypothesise that the arrangement of the silica-coated micelles (and therefore the distribution of the final mesoporous channels) can be described by a geometric arrangement intermediate between these two limiting scenarios. This intermediate situation would be compatible with a very loose random packing of identical spheres, from which a mean “layer spacing” can be calculated using the corresponding packing density value.<sup>29</sup> As a result, a combination of domains with different geometries going from perfectly hexagonal to others with a skewed alignment (towards the square alignment) as well as a definitely random distribution could produce, on average, homogeneous regions with short-range order and a characteristic diffraction pattern. This random packing is fundamentally similar to that found in the so called "amorphous alloys", where the distance between atoms can be described by a pair correlation function. For a comprehensive analysis of the scattering produced by the irregular assembly of uniformly-sized spheres, see: Particle and particle systems characterization: small-angle scattering (SAS) applications.<sup>30</sup>

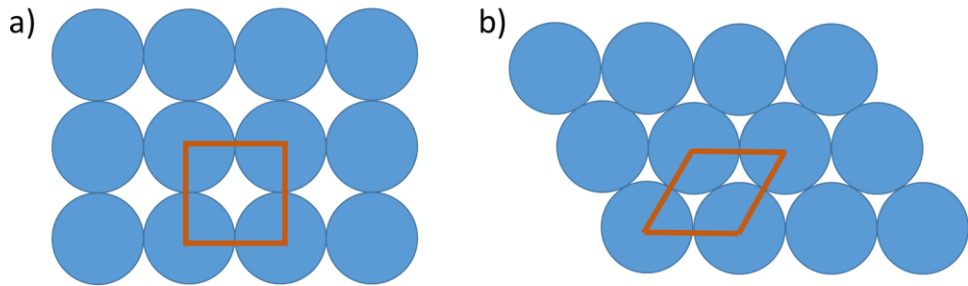


**Figure 7:** Close packing of uniformly-sized spheres arranged in a square lattice (a) and hexagonal lattice (b). The repeating unit cell of each pattern is highlighted.

### 5.1.2. Gas adsorption analysis

The adsorption of gas molecules on the surface of a solid material is an interfacial process that allows the structural characterization of fine powders and porous materials. A brief introduction to the topic is provided here focused on the structural characterization of ordered mesoporous materials. For a detailed description of gas adsorption processes, the reader is referred to specialized articles.<sup>31–34</sup>

According to the IUPAC recommendations,<sup>35</sup> the gas substance is called adsorptive in the fluid phase and adsorbate once adsorbed on the surface of the solid, which is known as the adsorbent (Figure 8).

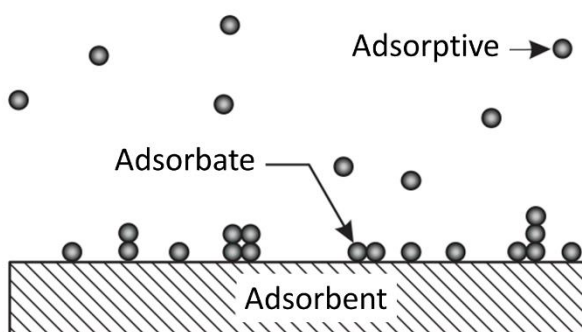


**Figure 8:** Common terms associated with gas adsorption: adsorptive, adsorbate and adsorbent. Adapted from *Physics and Chemistry of Interfaces*; Wiley-VCH, 2003.

Two types of adsorption processes are differentiated depending on the strength of the intermolecular forces between the adsorbate and the surface of the adsorbent: irreversible adsorption and reversible adsorption. In irreversible adsorption (also known as chemisorption), the adsorbed molecules are chemically bound to the surface of the solid, whereas in reversible adsorption (also known as physisorption), the interactions between adsorbate and adsorbent are governed by van der Waals' forces.<sup>32</sup> In the context of this work, we are dealing with the physical adsorption of nitrogen on the surface of mesoporous silica nanoparticles.

### 5.1.2.1. Adsorption isotherms

In adsorption experiments, the amount of gas adsorbed at a fixed temperature is measured as a function of the relative pressure of the gas ( $P/P_0$ ), where  $P$  is the equilibrium pressure and  $P_0$  is the saturation vapour pressure of the bulk liquid at that particular temperature.<sup>35</sup> An adsorption isotherm is a graphical representation of the amount of gas adsorbed per unit mass of adsorbate versus the relative pressure.

The adsorption behaviour of the gas depends on the particular pore structure of the adsorbent and its surface properties, leading to adsorption isotherms with different shapes.<sup>31</sup> Accordingly, the shape of the isotherm already contains structural information about the particular adsorbent investigated. According to the updated IUPAC classification,<sup>35</sup> adsorption isotherms can be classified into six main groups that are represented in Figure 9. Type III and type V isotherms present a small amount of gas adsorbed at low relative pressures, which indicates the existence of relatively weak interactions between the adsorbate and the adsorbent. Type II isotherms are usually exhibited by non-porous or macroporous materials, in which unrestricted monolayer-multilayer adsorption occurs.<sup>32</sup> Multi-layer adsorption is also found in the special type VI isotherm, where the adsorption of each layer can be clearly differentiated. Type I isotherms are characteristic of microporous materials, being further divided into type I(a) and type I(b) depending on the size of the micropores. Finally, type IV isotherms are found in mesoporous materials such as those prepared in this work. A detailed description of type IV

isotherms is presented in the following section, focusing on mesoporous silica materials.

**Type I:** Microporous materials.  
 (a) Narrow micropores <1 nm  
 (b) Wider micropores < 2.5 nm

**Type II:** Nonporous or macroporous materials with unrestricted monolayer-multilayer formation.

**Type III:** Nonporous or macroporous materials with weak adsorbate-adsorbent interactions.

**Type IV:** Mesoporous materials.  
 (a) Exhibit hysteresis loops.  
 (b) Completely reversible (e.g. MCM-41).

**Type V:** Microporous or mesoporous materials with weak adsorbate-adsorbent interactions.

**Type VI:** Nonporous materials with stepwise multilayer adsorption.

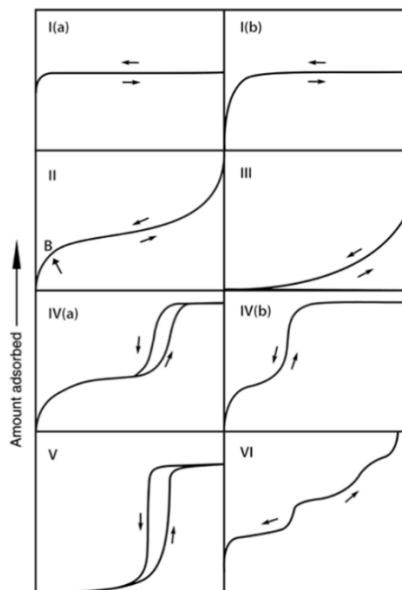


**Figure 9:** Description and graphical representation of the main types of adsorption isotherms according to the updated IUPAC classification. *Adapted from Pure Appl. Chem.* 2015, 87 (9–10), 1051–1069.

- The type IV isotherm in mesoporous materials

Type IV isotherms present a distinctive adsorption step at intermediate relative pressures produced by the capillary condensation (also known as pore condensation) of the gas inside the mesopores. This gas-liquid phase transition occurs at a relative pressure below the saturation pressure of the bulk liquid, a phenomenon induced by the confinement of the gas inside the mesopores and the appearance of fluid-wall and fluid-fluid interactions.<sup>36</sup> Accordingly, the relative pressure at which capillary condensation occurs depends on the size of the mesopores, a relation that is described by the Kelvin equation.<sup>32</sup>

The Kelvin equation predicts that the smaller the diameter of the pores, the lower is the relative pressure at which pore condensation occurs, a phenomenon that has been experimentally observed using mesoporous silica materials with different pore sizes.<sup>37</sup> This dependence has another consequence: pore condensation in materials with homogeneous pore sizes will occur over a small

range of relative pressures giving a steep condensation step. On the other hand, the presence of a heterogeneous distribution of mesopore sizes leads to a more progressive condensation step over a wide range of relative pressures.<sup>32</sup>

- The type IV isotherm in mesoporous silica nanoparticles

Figure 10 shows a representative example corresponding to the nitrogen adsorption-desorption isotherm of MCM-41 nanoparticles. The first part of the isotherm corresponds to monolayer-multilayer adsorption (I), which occurs at low relative pressures similarly to type II isotherms. Multilayer adsorption is followed by the aforementioned capillary condensation inside the mesopores (II), which accounts for the steep increase of gas adsorbed at relative pressures between 0.2-0.4. Once the mesopores are completely filled with liquid, a plateau region is observed in which the amount of gas adsorbed hardly increases (III). The preparation of mesoporous materials in the form of nanometer-sized particles leads to the appearance of an additional adsorption step in the isotherm at high relative pressures (IV). This is produced by the adsorption of gas in the cavities and interstices formed between the nanoparticles, usually referred as interparticle porosity.<sup>38</sup>

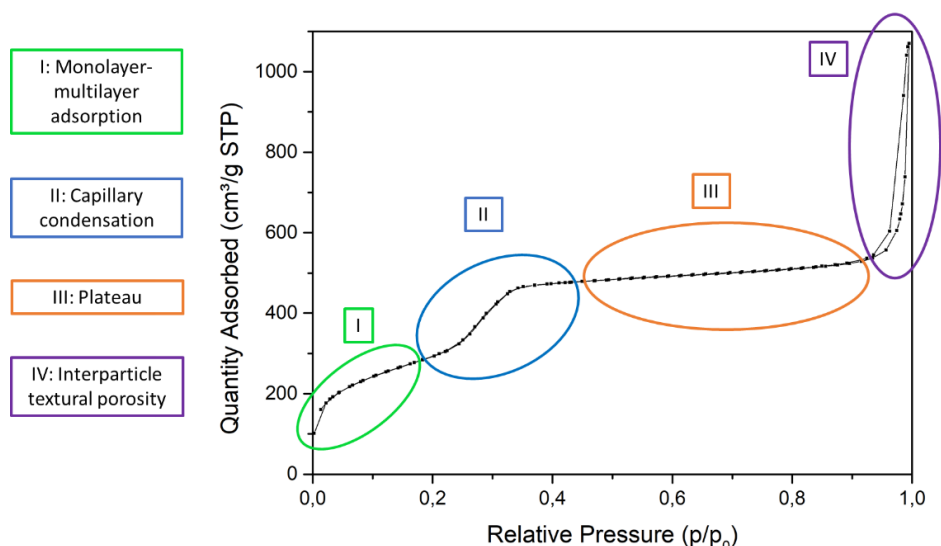


**Figure 10:** Type IV adsorption isotherm of mesoporous silica nanoparticles highlighting main characteristic regions.



- Sorption hysteresis

It is also important to highlight that type IV isotherms are sometimes accompanied by sorption hysteresis, a phenomenon that is observed when capillary condensation and capillary evaporation occur at different relative pressures.<sup>39</sup> As a result, type IV adsorption isotherms are further divided into type IV(a) and type IV(b) depending on the appearance or absence of hysteresis during capillary condensation.<sup>35</sup> For a given adsorption system, it has been shown that the appearance of hysteresis depends on the size and shape of the mesopores and also the temperature of the experiment.<sup>40,41</sup> A representative example is shown in Figure 11, in which the nitrogen adsorption isotherms of mesoporous silica materials with different pore sizes and shapes are presented. Reversible sorption isotherms were obtained for MCM-41 materials (with mesopore sizes of 3.30 and 4.25 nm), whereas hysteresis loops were obtained in the case of SBA-15 (6.7 nm) and controlled-pore glasses (11 and 16 nm).<sup>39</sup>

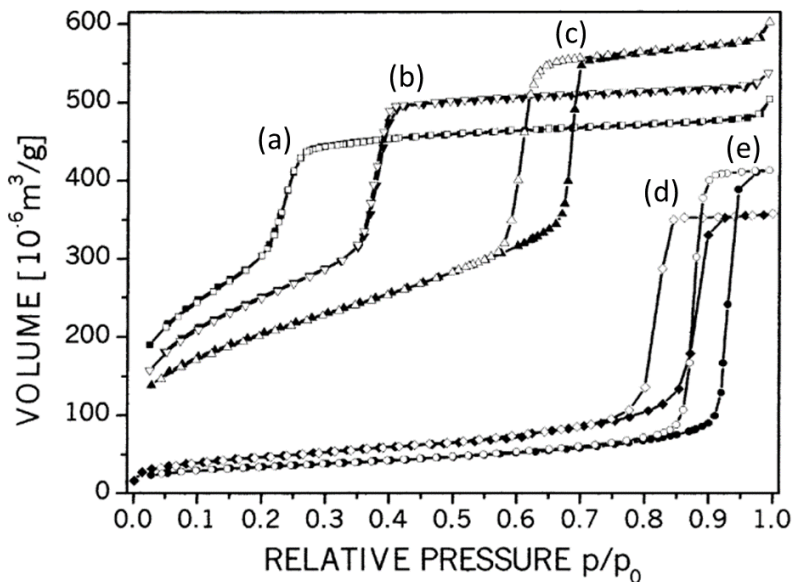


**Figure 11:** Nitrogen adsorption-desorption isotherms at 77 K in (a) MCM-41A (3.30 nm), (b) MCM-41C (4.25 nm), (c) SBA-15 (6.7 nm), (d) CPG (11 nm) and (e) CPG (16 nm). *Adapted from Appl. Surf. Sci. 2002, 196, 239–249.*

### 5.1.2.2. Assessment of adsorption isotherms in mesoporous silica nanoparticles

As already shown, the shape of the isotherms, the position and steepness of the condensation step or the appearance of hysteresis can provide information about the type of porosity, the size of the pores or even the uniformity in the distribution of pore sizes. However, in order to quantitatively determine key structural parameters such as the surface area of the material, the pore volume or the pore size distribution (PSD), the application of specific models of analysis is required.<sup>36</sup> Understanding the advantages and limitations of these models is therefore fundamental in order to obtain meaningful results.

- Surface area: the BET method

The surface area of porous and finely-divided materials has been traditionally evaluated using the Brunauer, Emmett and Teller (BET) method.<sup>42</sup> This method was derived from the kinetic model developed by Langmuir, which was further extended in order to describe the effect of multilayer adsorption.

The BET method is used to determine the monolayer capacity ( $n_m$ ), *i.e.* the amount of gas needed to form a monolayer of adsorbed molecules on the surface of the material. Once the monolayer capacity of the adsorbent is known, the specific surface area of the material ( $S_{BET}$ ) can be easily calculated using the average area occupied by the adsorbed molecules (*i.e.* the molecular cross-sectional area,  $a_0$ ). The relation between the BET surface area, monolayer capacity and molecular cross-sectional area is given by following equation, where  $N_A$  represents the Avogadro constant:<sup>43</sup>

$$S_{BET} = n_m N_A a_0 \quad (1)$$

As can be deduced from the previous equation, surface areas determined by the BET method strongly depend on both the accurate determination of  $n_m$  and  $a_0$ . The monolayer capacity,  $n_m$ , can be calculated using the BET equation, which is usually expressed in its linear form as:

$$\frac{P/P_0}{n(1-P/P_0)} = \frac{1}{n_m C} + \frac{C-1}{n_m C} \left( \frac{P}{P_0} \right) \quad (2)$$

where  $n$  is the amount of gas adsorbed at a given relative pressure ( $P/P_0$ ), and  $C$  is a parameter related to the heat of adsorption.<sup>35</sup>

In order to accurately determine the monolayer capacity, the BET method should be applied in the region of the isotherm in which the BET plot gives a straight line. In many porous materials with type II and type IVa isotherms, a linear relation is usually obtained in the range of relative pressures between 0.05-0.30.<sup>35</sup> Special attention must be paid when choosing the range of relative pressures in materials with type IVb isotherms, in which pore condensation may start at low relative pressures, overlapping with monolayer-multilayer adsorption and interfering with the determination of the monolayer capacity.<sup>32</sup> Determination of the monolayer capacity is also problematic in materials with a mixture of micropores and mesopores, making difficult to differentiate between the filling of micropores and the adsorption due to monolayer formation (both occurring at low relative pressures). In these cases, application of the BET method leads to an apparent surface area that includes both contributions.<sup>43,44</sup>

Regarding the molecular cross-sectional area of the adsorbate,  $a_0$ , it has been shown that its value strongly depends on the surface chemistry of the material used as adsorbent.<sup>45</sup> In the case of nitrogen, which is used as the standard adsorptive for the determination of BET surface areas, a molecular cross-sectional area of  $16.20 \text{ \AA}^2$  was originally proposed based on a close-packed arrangement of nitrogen molecules.<sup>46</sup> Although this value has been widely accepted as the customary cross-sectional area of nitrogen at  $77 \text{ }^\circ\text{K}$ , different values have been proposed for different adsorbent materials.<sup>31,45</sup>

The variation in the value of the cross-sectional area is attributed to the quadrupole moment of the nitrogen molecule, which can lead to a preferential adsorption orientation on materials with polar surface sites.<sup>32,43</sup> This effect has been reported in mesoporous silica materials with hydroxylated surfaces, in which the BET surface areas were overestimated by *ca.* 20% when the customary value of  $16.20 \text{ \AA}^2$  was applied.<sup>47</sup> The group of Jelinek and co-workers, proposed a corrected

nitrogen cross-sectional area of  $13.50 \text{ \AA}^2$ , obtained from the measurement of  $\text{N}_2$  adsorbed on hydroxylated silica spheres of known diameter.<sup>48</sup> Later works confirmed that the use of this value when working with silica materials led to BET surface areas that were in much better agreement with those obtained from argon adsorption experiments and those predicted by non-local density functional theory (NLDFT) models.<sup>39</sup> Accordingly, the corrected cross-sectional area of nitrogen ( $13.50 \text{ \AA}^2$ ) will be used to calculate the BET surface area of the mesoporous silica nanoparticles prepared in this work.

- Pore volume

Determination of the total pore volume is relatively simple in mesoporous materials that exhibit type IV isotherms with a well-defined horizontal plateau at high relative pressures. In these cases, it is customary to derive the total specific pore volume,  $V_p$ , from the amount of gas adsorbed at a relative pressure close to 1 (usually  $P/P_0 = 0.95$ ).<sup>31</sup>

In order to calculate liquid volumes from the amount of gas adsorbed, the Gurvich rule is usually applied, which assumes that the density of the adsorbate is equivalent to the density of the bulk liquid at the operational temperature.<sup>49</sup> Accordingly, the quantities of gas adsorbed ( $Q_a$ ) can be converted into liquid equivalent volumes ( $V_l$ ) by applying the following equation:

$$V_{li} = \frac{Q_i V_{mol}}{V_{mol,STP}} \quad (3)$$

where  $V_{mol}$  is the liquid molar volume of the fluid ( $34.65 \text{ cm}^3$  for  $\text{N}_2$  at  $77 \text{ °K}$ ) and  $V_{mol,STP}$  is the molar volume of the fluid at standard temperature and pressure ( $22414 \text{ cm}^3$ ).

In the case of mesoporous nanoparticles that exhibit interparticle porosity, the amount of gas adsorbed at a relative pressure close to 1 can no longer be used to estimate the total pore volume.<sup>35</sup> In these cases, there is not a defined relative pressure for the estimation of the mesopore volume. Some authors have opted to measure the amount of gas adsorbed just after the capillary condensation

process,<sup>39,47</sup> whereas others consider the amount of gas adsorbed at the end of the plateau.<sup>50–52</sup> Once again, different interpretations lead to experimental results that are not comparable between different publications. In this work, mesopore volumes will be determined based on the amount of gas adsorbed just after capillary condensation, which corresponds to the complete pore filling.<sup>32</sup>

- Pore size analysis

Pore condensation has been traditionally described using the Kelvin equation, which relates the diameter of the mesopores with the relative pressure at which pore condensation occurs.<sup>45</sup> In fact, the Kelvin equation has become the basis for the development of many classical methods for the determination of the mesopore size, such as the widely used Barrett-Joyner-Halenda (BJH) method.<sup>53</sup> However, all these methods rely on the applicability of the Kelvin equation, which was conceived based on macroscopic, thermodynamic assumptions.<sup>43</sup> As a result, these classical approaches become less and less reliable as the size of the mesopores decreases, since the equilibrium phase transition occurring inside narrow mesopores can no longer be described using macroscopic/thermodynamic concepts.<sup>32</sup> It has been shown that application of the BJH approach and related methods to determine the mesopore size of materials with narrow mesopores (< 10 nm) can lead to an underestimation of the mesopore size up to 20-30%.<sup>35,54</sup>

In an attempt to overcome the limitations found when using classical approaches, microscopic methods based on molecular simulations or density functional theory (DFT) were developed.<sup>55–58</sup> DFT methods are able to predict the theoretical isotherm for a specific adsorptive/adsorbent system and a particular pore geometry. It is now well accepted that these methods are able to describe the phase behaviour of the adsorbate on a molecular level, providing more reliable pore size distributions throughout the whole micropore-mesopore range.<sup>35,36,43</sup>

In the context of this work, the BJH method will be used as a first approximation to assess the adsorption processes occurring in the core-shell M-MSNs. Determination of pore sizes will be conducted using the more accurate DFT method, using a specific model for the adsorption of nitrogen on materials with an oxide surface and cylindrical pores.

## 5.2. Materials and methods

### 5.2.1. Synthesis of MCM-41 nanoparticles

The synthesis of MCM-41 nanoparticles was conducted based on a previous reported protocol.<sup>59</sup> Briefly, 1 g of CTAB (2.74 mmol) was first dissolved in 480 ml of milli Q water. The solution was stirred at 500 rpm inside a 1 L beaker using a rod-shaped stirring magnet (L = 3 cm). NaOH (0.28 g, 7 mmol) was dissolved separately in 3.5 ml of milli Q water and added to the previous solution. The temperature of the reaction was increased to 80 °C and the stirring rate was adjusted to 1200 rpm. Then, 5 ml of TEOS (22.39 mmol) were added dropwise leading to the formation of a white precipitate. The reaction was left stirring for 2 h. The obtained white precipitate was centrifuged at 9500 rpm during 20 min. and washed with distilled water until neutral pH. Then, the solid was dried in oven at 70 °C and the surfactant template was removed by calcination in air at 550 °C during 5 h.

### 5.2.2. Synthesis of core-shell M-MSNs

For the preparation of the core-shell M-MSNs, the general protocol developed in chapter 4 was applied.

### 5.2.3. Characterization techniques

Powder X-ray diffraction (PXRD) measurements were conducted using a Bruker AXS D8 Advance diffractometer equipped with CuK $\alpha$  radiation ( $\lambda=1.5406 \text{ \AA}$ ) and working at 40 kV/40 mA. The study of mesostructural order within the core-shell M-MSNs was conducted in the low-angle region of  $2\theta = 1.3 - 8.3$ .

TEM analysis was performed on a 100 kV JEOL JEM-1010 transmission electronic microscope operated with AMT image capture engine software. Samples were prepared by dropping 10  $\mu\text{l}$  of nanoparticles suspended in ethanol onto carbon-coated copper grids. The size of the nanoparticles was measured using TEM analysis imaging software.

SEM analysis was performed using a ZEISS-ULTRA 55 field emission scanning electron microscope working in the range 0.5-20 kV.

High-resolution transmission electron microscopy (HRTEM) was conducted on a 200 kV JEOL JEM-2100F equipment. The microscope is equipped with a STEM unit with a high-angle annular dark-field (HAADF) detector, which was used for STEM dark-field imaging.

Dynamic light scattering (DLS) experiments were conducted with a Zetasizer Nano ZS (Malvern Instruments) equipped with a laser of 633 nm and collecting the signal at 173°. Hydrodynamic size distributions were measured three times, from which the average PDI and Z-average values were obtained using Zetasizer Software (version 7.10).

Nitrogen adsorption experiments (77.35 °K) were conducted using a TriStar II Plus surface area and porosity analyzer from Micromeritics. Prior to gas adsorption experiments, the samples were outgassed at 493 °K and high vacuum for at least 12 h. Analysis of the isotherm curves was conducted using MicroActive for TriStar II Plus software (version 2.02). BET surface areas were calculated from the adsorption branch in a range of relative pressures before the pore condensation step, assuming a cross-sectional area of nitrogen of 13.5 Å<sup>2</sup> (value proposed for N<sub>2</sub> molecules adsorbed on hydroxylated silica).<sup>47,48</sup> The pore size distribution (PSD) and cumulative pore volumes were determined using the density functional theory (DFT) method applied to the adsorption branch. A model for the adsorption of nitrogen on materials with an oxide surface and pores with a cylindrical geometry was applied, as recommended for silica materials with H1 type hysteresis.<sup>60</sup> Mesopore volumes were determined directly from the adsorption branch of the isotherm just after the capillary condensation process, which corresponds to the complete filling of the mesopores.<sup>32</sup>

For comparison purposes, a second equipment was used to determine the PSD of two core-shell M-MSNs samples synthesised under different stirring conditions. The equipment used was a Quadrasorb-Kr/MP from Quantachrome. The samples were outgassed at 523 °K for 8 h and the PSD was determined using a DFT method (Calc. Model: N<sub>2</sub> at 77 K on silica, cylindrical pore, NLDFT equilibrium model).

## 5.3. Results and discussion

### 5.3.1. Structural characterization

As already discussed in the introduction, core-shell-type M-MSNs present a complex structure that cannot be described using a simple geometrical model. For this reason, MCM-41-type MSNs have also been prepared and analysed in this work, being used as a reference material due to their well-known structural properties.

The structural properties of the core-shell M-MSNs have been investigated using three main characterization techniques: powder XRD, nitrogen adsorption analysis and electron microscopy analysis. These techniques have also been used to assess the effect that the main reaction parameters identified in the previous chapter (stirring rate, initial amount of seeds and time of reaction) have on the structure of the nanoparticles.

#### 5.3.1.1. XRD analysis

##### MCM-41 nanoparticles

The obtained MCM-41 nanoparticles exhibited the characteristic diffraction pattern of MCM-41 materials, with a main first-order reflection accompanied by three additional diffraction peaks (Figure 12). The diffraction peaks appear separated by a  $1: \sqrt{3}: \sqrt{4}: \sqrt{7}$  ratio, in agreement with a hexagonal arrangement of mesoporous channels ( $p6mm$  space group), being indexed as (100), (110), (200) and (210).<sup>8,9</sup> The position of the diffraction peaks ( $2\theta$  values) were used to calculate the corresponding interplanar spacings ( $d_{hkl}$ ), which are included in Figure 12.



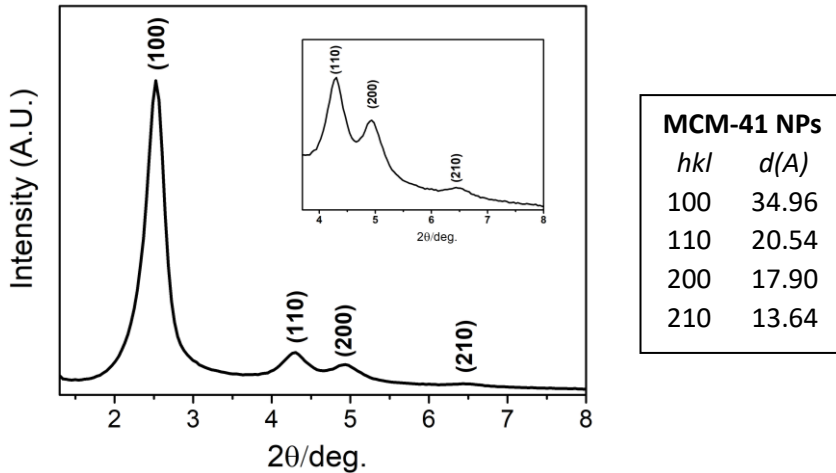


**Figure 12:** Diffraction pattern of calcined MCM-41 nanoparticles and corresponding *d*-spacing values calculated using Bragg's law (CuK $\alpha$ 1 radiation:  $\lambda=1.5406$  Å).

Considering that the pores of the MCM-41 nanoparticles are arranged following a hexagonal pattern, the obtained interplanar spacings can be used to calculate the average centre-to-centre pore distance. An ideal hexagonal unit cell is presented in Figure 13, in which the lattice constant parameter ( $a_0$ ), the [100] and [110] planes, and the  $d_{100}$  and  $d_{110}$  interplanar spacings are shown. The  $a_0$  parameter corresponds to the centre-to-centre pore distance in the 2-dimensional hexagonal lattice and can be calculated using basic trigonometric functions ( $a_0 = 2 \cdot d_{100} / \sqrt{3}$ ). An average centre-to-centre pore distance of 4 nm was obtained for our MCM-41 nanoparticles in perfect agreement with the values reported for MCM-41 materials synthesized using CTAB as a template.<sup>1,2</sup>

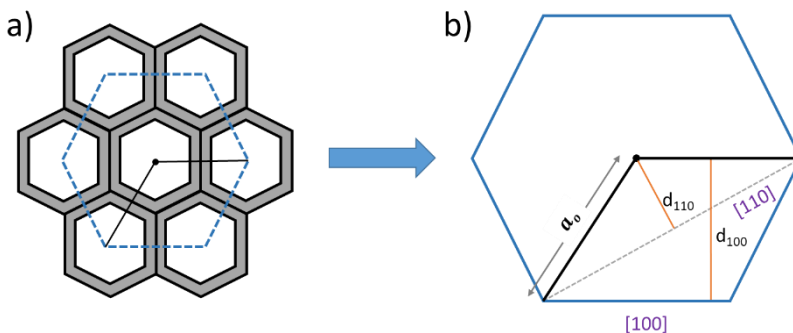


**Figure 13:** a) Characteristic hexagonal arrangement of pores in MCM-41 materials and b) hexagonal unit cell with the lattice constant parameter ( $a_0$ ), the [100] and [110] planes, and the  $d_{100}$  and  $d_{110}$  interplanar spacings. Adapted from *Phys. Chem. Chem. Phys.* 2006, 8 (29), 3467–3474.

### Core-shell M-MSNs

The diffraction pattern of the core-shell M-MSNs showed an intense diffraction peak accompanied by a second much broader signal, highlighted by an arrow in Figure 14. The reduction in the number of diffraction reflections is indicative of a loss of structural order. This is also manifested by the broadening of the diffraction peaks, which indicates that the distance between neighbouring pores is less homogeneous than in the MCM-41 particles. However, it is important to note that the broadening of the XRD signals could also be related with a reduction in the size of the nanoparticles.<sup>61</sup>

The position of the main (100) diffraction peak is shifted to lower angles compared to the MCM-41 nanoparticles, leading to a higher  $d_{100}$ -spacing value (48.66 Å). Based on the two geometries proposed to describe the local order of the mesoporous channels of the core-shell M-MSNs, two lattice constant parameters are obtained: 4.9 nm for a square-like arrangement of channels and 5.6 nm for a hexagonal-like arrangement.

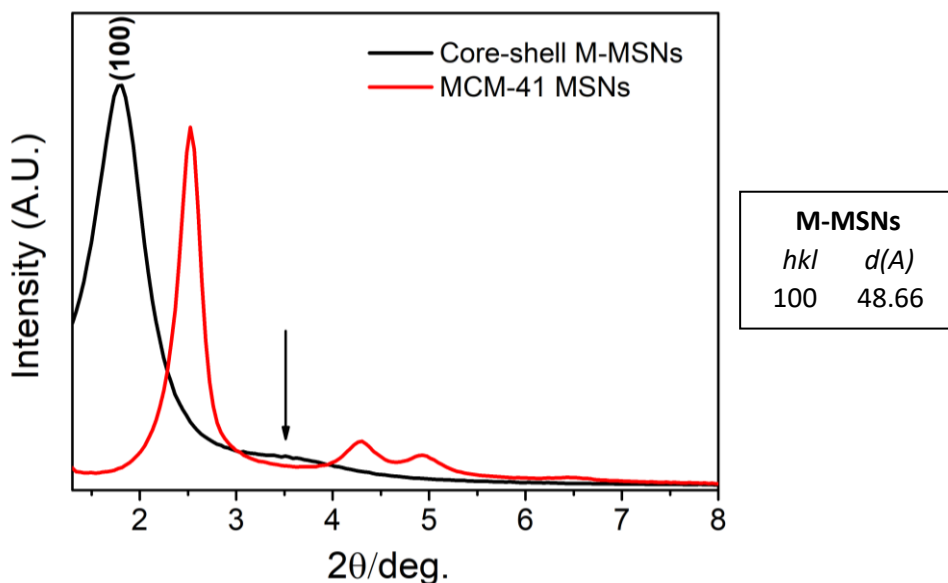


**Figure 14:** Diffraction pattern of calcined MCM-41 vs calcined core-shell M-MSNs.  $d$ -spacing value calculated from the (100) diffraction peak of the core-shell M-MSNs.

### Effect of calcination

The diffraction patterns before and after calcination of the nanoparticles were also compared in order to identify any structural changes produced by the high temperatures applied during calcination (550 °C, 3 h). As can be seen in Figure 15.A, the MCM-41 nanoparticles presented the same number of diffraction peaks after calcination, indicating that the hexagonal symmetry in the arrangement of channels was maintained. However, the peaks are shifted to higher  $2\theta$  values and present a significant increase of intensity compared to the uncalcined sample. The shift to higher angles is commonly observed in mesoporous silica materials due to the condensation of silanol groups and the contraction of the silica framework after calcination.<sup>1</sup> The increase of diffraction intensity is also well documented and it is attributed to an improvement of structural order due to a most efficient packing of the mesoporous channels together with an increase of contrast between the silica walls and the empty mesoporous channels after elimination of surfactant and water.<sup>6,20,62</sup>

The core-shell M-MSNs presented the same diffraction pattern after calcination (Figure 15.B), indicating that the mesoporous structure was thermally stable. In contrast to the MCM-41 nanoparticles, the position of the main diffraction peak barely changed after calcination, indicating that the condensation of silanol groups in this type of materials is not leading to a significant shrinkage of the silica framework. As a result, the centre-to-centre pore distance in the core-shell M-MSNs is not experiencing a big change after calcination, in contrast to the significant reduction observed in the MCM-41 nanoparticles, as shown in Table 1.

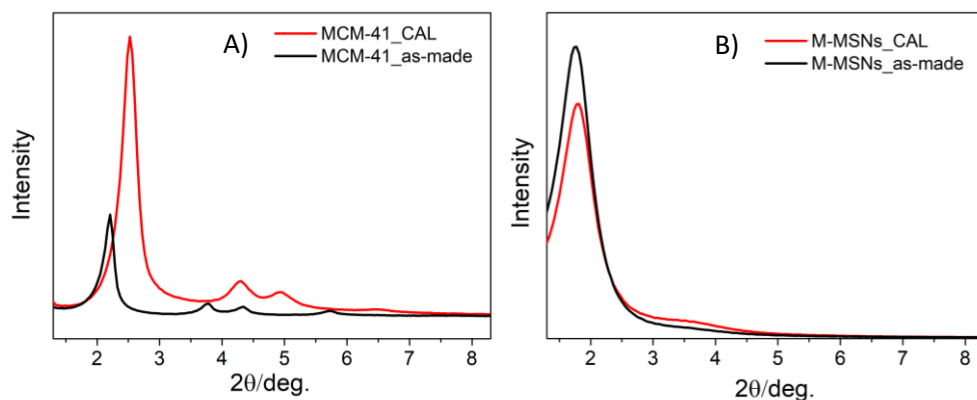


**Figure 15:** XRD patterns of calcined vs as-made MCM-41 nanoparticles (A) and core-shell M-MSNs (B).

**Table 1:** Comparison of lattice parameters (centre-to-centre pore distances) between as-made and calcined samples. \*Pores arranged in a hexagonal lattice ( $a_0 = 2 \cdot d_{100} / \sqrt{3}$ ). \*\*Pores arranged in a square lattice ( $a_0 = d_{100}$ ).

Material	$2\theta$ (°)	$d_{100}$ (Å)	$a_0$ (Å)*	$a_0$ (Å)**
MCM-41_as-made	2.209	39.96	46.14	-
MCM-41_CAL	2.525	34.96	40.37	-
M-MSNs_as-made	1.773	49.78	57.48	49.78
M-MSNs_CAL	1.814	48.66	56.19	48.66

### 5.3.1.2. Electron microscopy

In agreement with the diffraction patterns obtained for the MCM-41 MSNs, TEM analysis confirmed the presence of parallel straight mesoporous channels, which could be seen arranged in a hexagonal pattern when aligned parallel to the microscope electron beam (red circle in Figure 16.A). In the case of the core-shell M-MSNs, the mesoporous channels are sometimes curved, which gives them their “wormhole-like” appearance, as shown in Figure 16.B. The second characteristic feature of these particles is the radial alignment of the mesoporous channels, stretching from the core to the surface of the nanoparticles. As a result, the

channels can be seen perpendicular to the nanoparticle surface. This particular arrangement of channels is in agreement with the results obtained for similar core-shell M-MSNs synthesised through a seeded-growth method.<sup>13-15,63</sup>

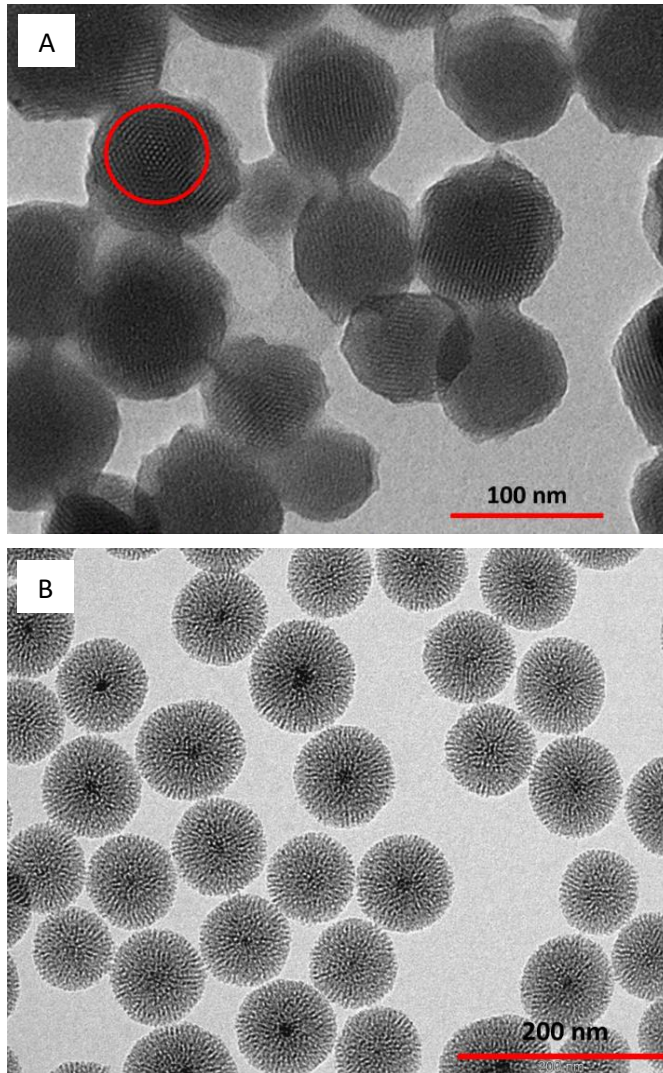


**Figure 16:** TEM micrographs of (A) calcined MCM-41 nanoparticles and (B) core-shell M-MSNs. The hexagonal arrangement of channels in the MCM-41 nanoparticles is highlighted.

High-resolution transmission electron microscopy (HRTEM) and high-angle annular dark field scanning transmission electron microscopy (HAADF-STEM) provided complementary images about the internal structure of the core-shell M-MSNs. It is important to highlight that both HRTEM and HAADF-STEM images are 2-D projections of a 3-dimensional object, which poses some limitations to the study of the internal network of mesoporous channels. As can be seen in Figure 17, the particular orientation of the particle with respect to the microscope electron beam reveals different structural motifs: a hexagonal pattern at the center of the particle (red), parallel channels perpendicular to the nanoparticle surface (green) and an irregular structure (blue).

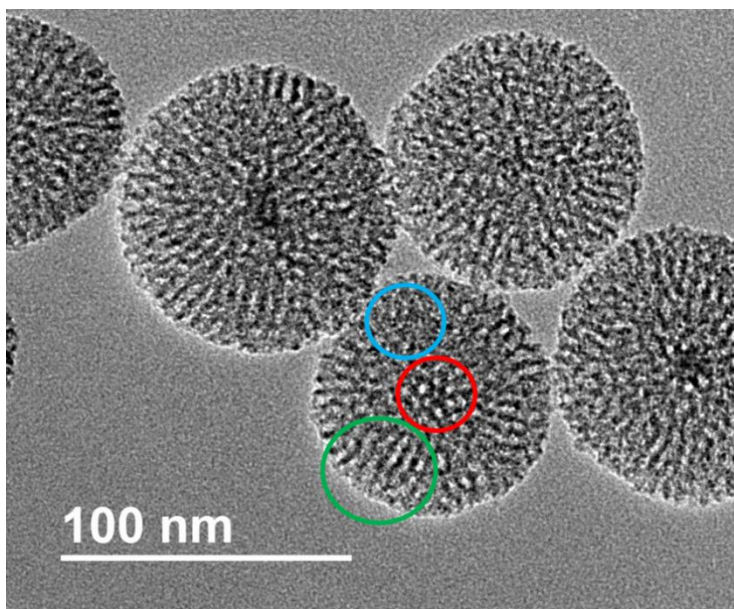


**Figure 17:** HRTEM micrograph showing the variability of structures exhibited by the obtained core-shell M-MSNs.

The complementary images obtained by HAADF-STEM displayed the dense magnetic cores and silica walls in a bright colour against a black background, revealing the “skeleton” of the nanoparticles (Figure 18.A). This confirmed that all the core-shell M-MSNs presented at least one magnetic core per nanoparticle. A section of Figure 18.A was magnified and contrast-saturated in order to facilitate

the visualization of the internal structure, revealing a sponge-like structure formed by radially aligned mesoporous channels (Figure 18.B).

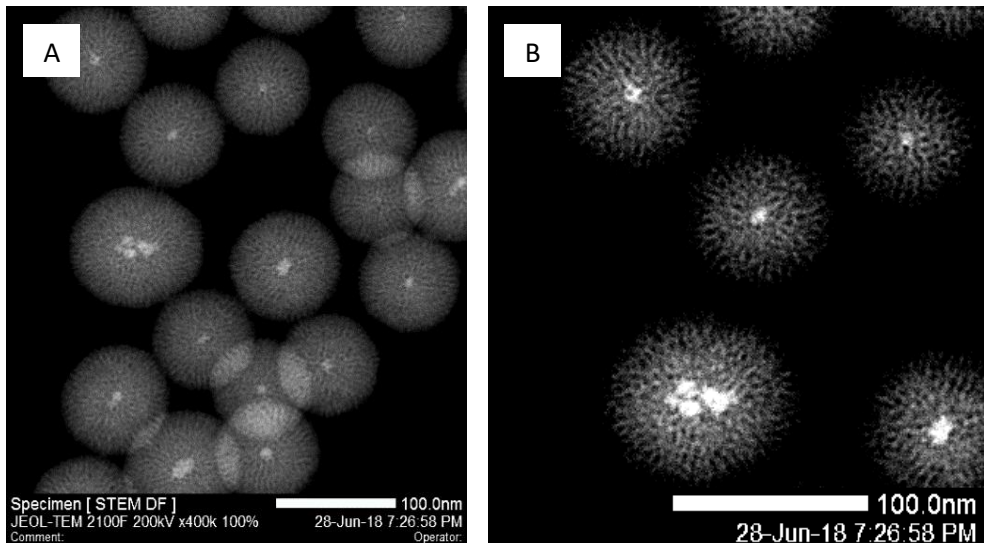


**Figure 18:** (A) HAADF-STEM micrograph of the obtained core-shell M-MSNs and (B) contrast-saturated magnified section of (A).

Finally, the surface of the nanoparticles was analysed using scanning electron microscopy (SEM). SEM micrographs showed that the obtained core-shell M-MSNs present a spherical morphology and confirmed that the size of the nanoparticles is highly uniform, as shown in Figure 19.A. Moreover, the nanoparticles present a homogeneous distribution of pores along the surface, resembling miniaturized sponges, in agreement with the structure observed in similar nanoparticles with radially-aligned mesoporous channels.<sup>64</sup>

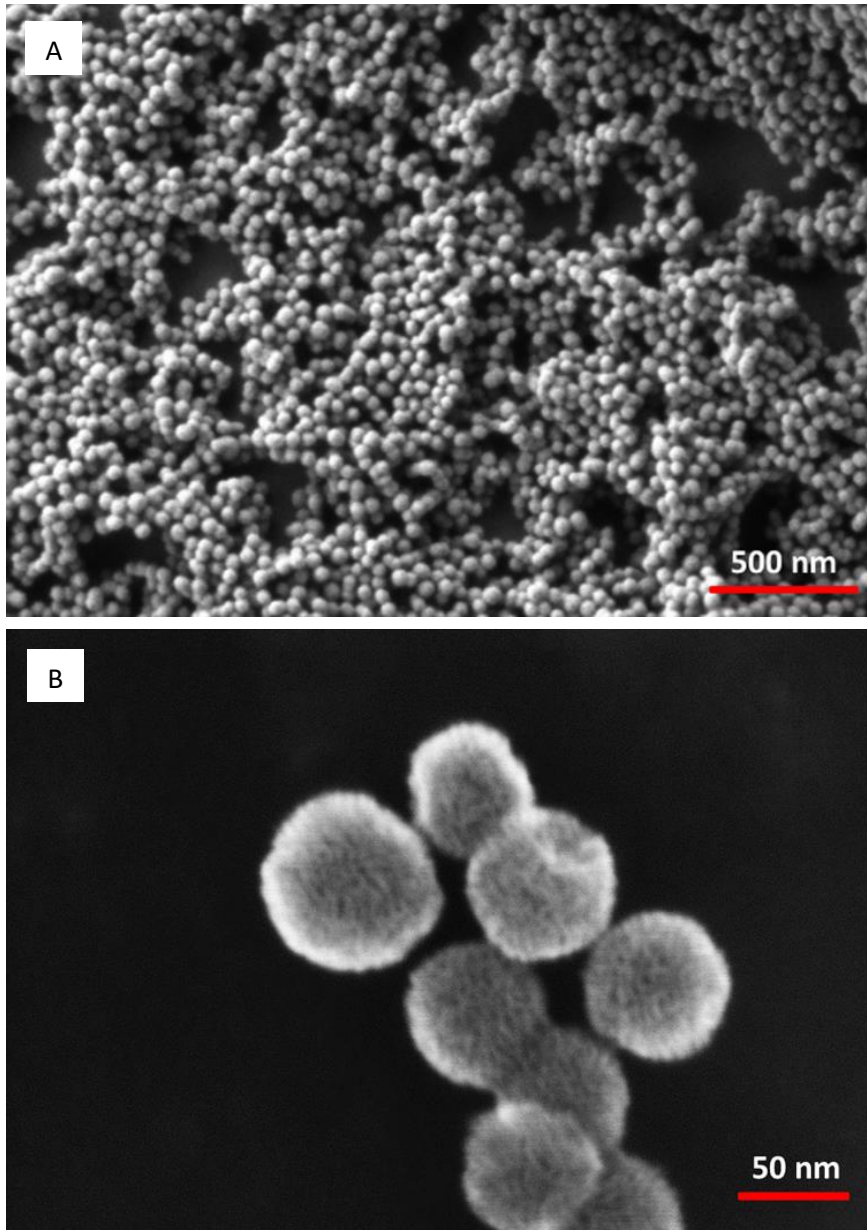


**Figure 19:** Two representative SEM micrographs taken from core-shell M-MSNs, showing (A) highly uniform spherical particles and (B) the homogeneous distribution of pores on the surface of the nanoparticles.



### 5.3.1.3. Nitrogen adsorption analysis

The nitrogen adsorption-desorption isotherms of both calcined MCM-41 nanoparticles and calcined core-shell M-MSNs are presented in Figure 20. Both nanoparticles displayed the characteristic type IV isotherms of mesoporous materials.<sup>35</sup> The pore condensation step is more pronounced in the case of the MCM-41 nanoparticles, reflecting that the size of the mesoporous channels is highly homogeneous in this material. On the other hand, the core-shell M-MSNs presented a more progressive condensation step, in agreement with a wider distribution of mesopore sizes. Finally, the significant adsorption of gas at high relative pressures ( $P/P_0 > 0.9$ ) indicates that both types of nanoparticles present interparticle porosity due to their small particle size.<sup>38</sup>

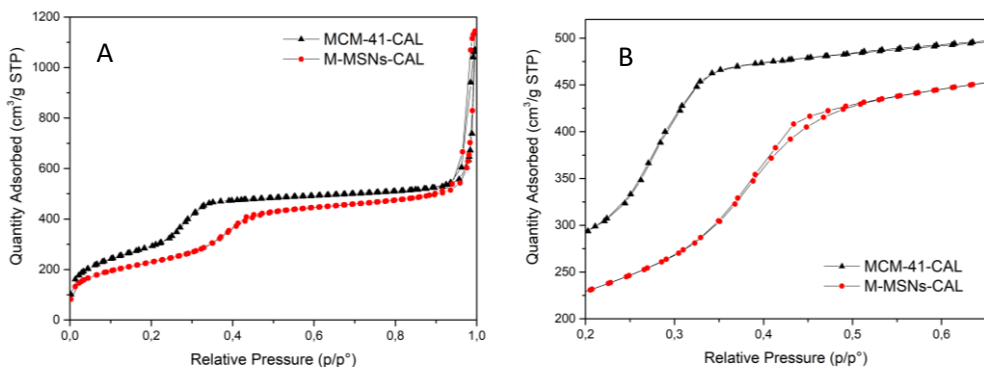


**Figure 20:** (A) Nitrogen adsorption-desorption isotherms of calcined MCM-41 nanoparticles and core-shell M-MSNs. (B) Magnified view corresponding to the pore condensation step, showing the small hysteresis exhibited by the core-shell M-MSNs.

Figure 20.B shows a magnified view corresponding to the pore condensation step. As can be seen in the image, pore condensation starts at lower relative pressures in the MCM-41 nanoparticles (inflection point at  $P/P_0 = 0.27$ ) compared to the core-shell M-MSNs (inflection point of the desorption branch at  $P/P_0 = 0.39$ ). According to the Kelvin equation, this is a first indication about the smaller diameter of the mesoporous channels in the MCM-41 nanoparticles compared to the core-shell M-MSNs.<sup>32</sup> It is also important to highlight that the adsorption-desorption isotherms of the MCM-41 nanoparticles are completely reversible, whereas the core-shell M-MSNs presented a small hysteresis. The absence of a large hysteresis

loop in the core-shell M-MSNs is especially relevant, being compatible with a regular network of more or less cylindrical mesoporous channels.<sup>43</sup>

The BJH model was applied as a first approximation to assess the PSD of the samples, which showed a single distribution of mesopore sizes as shown in Figure 21.A. It also confirmed that the MCM-41 nanoparticles presented smaller mesopore sizes (2.5 nm) than the core-shell M-MSNs (3.1 nm). A similar trend was obtained when the PSD was evaluated with a DFT method (Figure 21.B). In this case however, the average mesopore size predicted by the model was 3.5 nm for the MCM-41 nanoparticles and 4.2 nm for the core-shell M-MSNs. This is consistent with the underestimation of size reported in the literature when the BJH model is applied to materials with pores smaller than 10 nm.<sup>35,54</sup> As a result, the pore size analysis of the materials synthesised in this work, will be conducted using the more accurate DFT method.

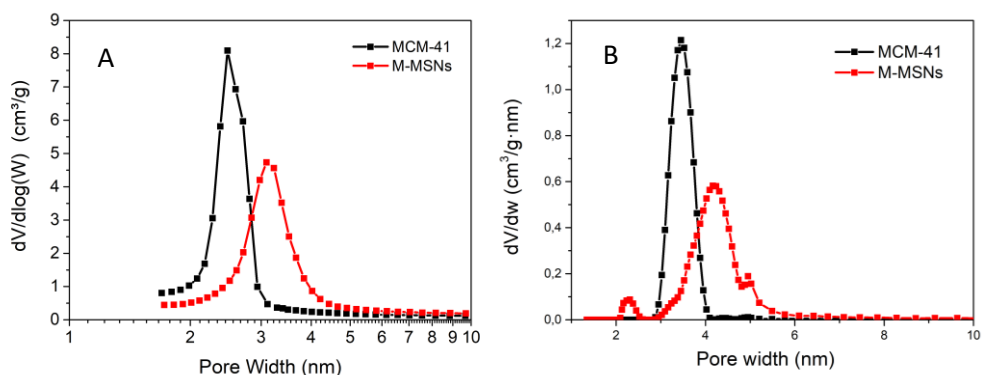


**Figure 21:** PSD distributions derived from the adsorption isotherms of the MCM-41 nanoparticles and core-shell M-MSNs using (A) the BJH method and (B) a DFT method.

### 5.3.2. Influence of reaction parameters on the structural properties of core-shell M-MSNs

#### 5.3.2.1. Stirring rate

As already discussed in the previous chapter, stirring rate plays a fundamental role in the synthesis of the core-shell M-MSNs and it was expected to greatly influence the mesoporous structure of the nanoparticles. Two samples were prepared applying different stirring conditions during a 3 h reaction. The first sample,  $S_M$ , was prepared under moderate stirring conditions (850 rpm during the first 2 min. and 350 rpm for 3 h), whereas the second sample,  $S_T$ , was prepared applying turbulent stirring conditions (850 rpm, 3 h). TEM analysis clearly showed the difference in the structural order between both samples:  $S_M$  presented the characteristic radially-aligned wormhole-like channels, whereas  $S_T$  showed a more disordered mesostructure (Figure 22).

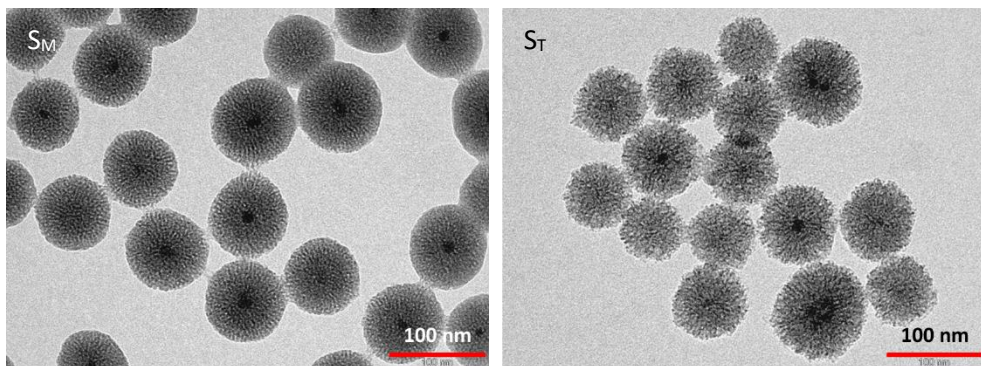


**Figure 22:** TEM micrographs of core-shell M-MSNs synthesised under moderate (left) and turbulent stirring conditions (right).

The increase of disorder within the structure was also reflected in the corresponding diffraction patterns: turbulent conditions led to a much broader diffraction peak, which was shifted towards lower angles (Figure 23). Peak broadening indicates that the  $S_T$  particles present a wider distribution of mesopore sizes, in agreement with a more disordered assembly of silica-coated micelles during the formation of the mesoporous silica shell. The shift of the peak towards lower angles suggests that the  $S_T$  samples is composed of channels that are further apart (increase of wall thickness) and/or present larger diameters.

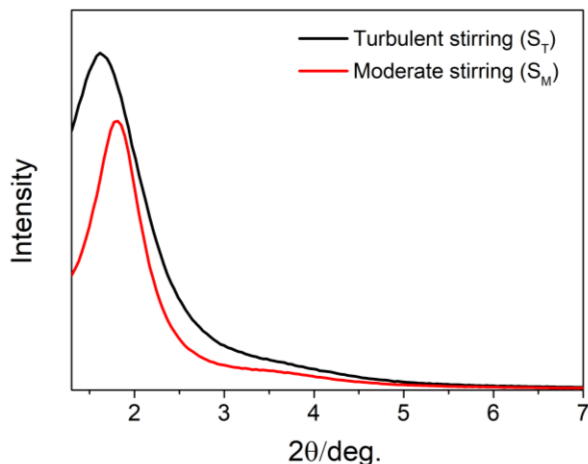


**Figure 23:** XRD patterns of core-shell M-MSNs synthesised under different stirring conditions.

Nitrogen adsorption analysis confirmed that the stirring conditions applied during the synthesis also influenced the mesoporous structure of the nanoparticles. This can be appreciated in the adsorption isotherms of both materials, which showed that an increase of stirring leads to a shift of pore condensation to higher relative pressures and an increase of the hysteresis loop (Figure 24.A and 24.B). As a result, a broader distribution of mesopore sizes was obtained for the  $S_T$  sample, reflecting an increase of disorder due to the use of turbulent stirring conditions (Figure 24.C). However, the PSD of the  $S_T$  sample was split into two sharp peaks, in marked contrast with the single adsorption step observed in the adsorption isotherm of the sample, which suggested that the additional peaks could be an artifact of the model applied.

In order to test this hypothesis, the samples were measured in a different gas adsorption instrument, which was equipped with a different analysis software (see materials and methods). The PSD was determined in this case with a NLDFT equilibrium model for the adsorption of nitrogen on silica with cylindrical pores (model 2). As can be seen in Figure 24.D, the PSD calculated with the model 2 presented a single peak, confirming that the additional peaks observed in the first case were an artifact of the model applied. The textural properties determined by both models are presented in Table 2.

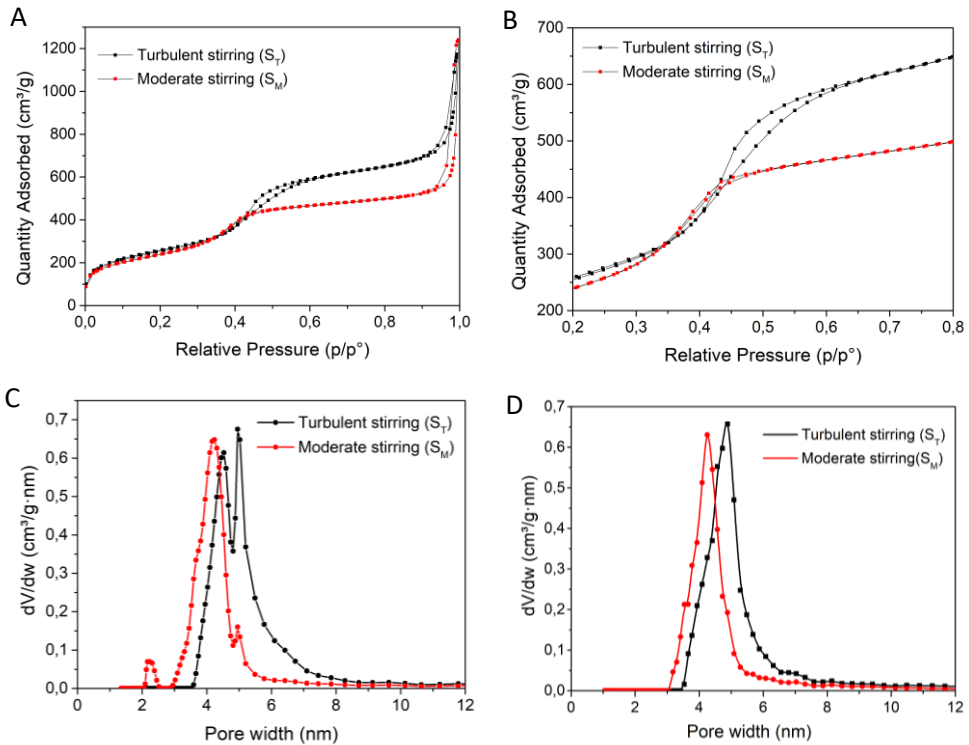


**Figure 24:** Textural characterization of core-shell M-MSNs synthesised under different stirring conditions. (A) Nitrogen adsorption-desorption isotherms. (B) Magnified view of the pore condensation step. (C) PSD calculated by a DFT method using the model 1 and (D) PSD calculated using a NLDFT equilibrium model (model 2).

**Table 2:** Textural properties of the  $S_T$  and  $S_M$  samples determined by two different instruments, one from Micromeritics® (equipment 1) and another from Quantachrome® (equipment 2). <sup>a)</sup> The average pore diameter ( $d_p$ ) was determined by a DFT method in the equipment 1 and a NLDFT equilibrium method in the equipment 2. <sup>b)</sup> Pore volumes ( $V_p$ ) were calculated directly from the isotherm at a relative pressure corresponding to the complete filling of the mesopores:  $P/P_0=0.65$  for the  $S_T$  sample and  $P/P_0=0.5$  for the  $S_M$  sample.

Sample	Equipment/ model	$d_p^{\text{a)}$ (nm)	$V_p^{\text{b)}$ ( $\text{cm}^3/\text{g}$ )
$S_T$	1	4.5	0.94
$S_M$	1	4.2	0.69
$S_T$	2	4.8	0.87
$S_M$	2	4.2	0.68

Both models show how the use of turbulent stirring conditions leads to a slight increase of mesopore sizes and, more significantly, an increase of pore volumes. Additional tests would be desirable in order to confirm this correlation, since it represents a simple strategy to tune the textural properties of the material by simply adjusting the stirring conditions applied during the reaction.

It is also important to note that both models, which were developed assuming a cylindrical geometry of channels, predicted very similar textural properties for the  $S_M$  sample (Table 2). This indicates a good correlation between the cylindrical geometry of the models and the shape of the mesoporous channels in this sample. This is not the case for the  $S_T$  sample, in which the appearance of artifacts (model 1) and variations in the parameters predicted by the models, suggest deviations from an ideal cylindrical geometry induced by the turbulent conditions applied.

### 5.3.2.2. Initial amount of seeds and reaction time

As already discussed in chapter 4, the initial amount of seeds used in the reaction determines the size of the final core-shell M-MSNs. Moreover, it was observed that extended reaction times lead to an increase of nanoparticle aggregation during the synthesis. Thus, it was essential to test if variation of these reaction parameters could also influence the structural properties of the resulting nanoparticles.

Figure 25 shows the diffraction pattern of four representative samples synthesised under the stirring conditions established in our optimized synthetic protocol (850 rpm during the first 2 minutes of reaction and 350 rpm for the remaining reaction time). It can be seen that both the position and broadness of the main diffraction peak are very similar in all cases, independently of the size of the nanoparticles or the reaction time applied. The only noticeable difference is the intensity of the main diffraction peak, which was attributed to the amount of sample used in each case for the XRD measurements. The similarity between the different diffraction patterns indicates that, under the reaction conditions applied, the mesostructure of the nanoparticles is not highly influenced by the amount of seeds used or the time of reaction applied.

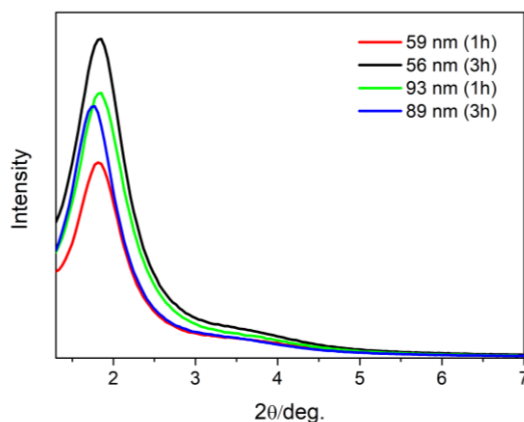


**Figure 25:** Representative XRD patterns from core-shell M-MSNs with different sizes and synthesised in 1 h/3 h.

The diffraction patterns of 10 different samples prepared under the optimized stirring conditions were analysed in order to obtain a representative centre-to-centre pore distance. Table 3 shows the size of the core-shell M-MSNs (determined by TEM analysis), together with the position of the main (100) diffraction peak and the corresponding lattice parameter calculated for the two limiting geometries proposed.

**Table 3:** Comparison of lattice parameters (centre-to-centre pore distances) between core-shell M-MSNs of different sizes and synthesis reaction times of 1h or 3h. \*Pores arranged in a square lattice ( $a_0 = d_{100}$ ). \*\*Pores arranged in a hexagonal lattice ( $a_0 = 2 \cdot d_{100} / \sqrt{3}$ ).

Sample	React. time (h)	$d_{\text{TEM}}$ (nm)	$2\theta_{100}$ (°)	$a_0$ (Å)*	$a_0$ (Å)**
1	3	56	1.774	49.75	57.45
2	3	62	1.853	47.63	55.00
3	3	75	1.735	50.89	58.76
4	3	83	1.814	48.67	56.20
5	3	87	1.735	50.89	58.76
6	3	89	1.774	49.75	57.45
7	3	91	1.774	49.75	57.45
8	1	57	1.814	48.67	56.20
9	1	59	1.853	47.63	55.00
10	1	93	1.853	47.63	55.00
<b>Average</b>			<b>1.800</b>	<b>49.13</b>	<b>56.73</b>

The obtained results showed that the synthetic protocol developed provided excellent control over the structural order of the core-shell M-MSNs. The position of the main (100) diffraction peak consistently appeared at a  $2\theta$  value centered around  $1.8^\circ$ , which corresponds to a cell parameter of  $4.9 \pm 0.1$  nm for an ideal square-like arrangement of channels and  $5.7 \pm 0.1$  nm for a perfectly hexagonal arrangement of channels. Accordingly, an average centre-to-centre pore distance between these two values is proposed for the core-shell M-MSNs. It could be argued that the presence of a second broad peak at approximately twice the distance of the (100) peak, indicates a greater contribution from domains in which the channels are arranged on average following a square-like pattern. Based on this assumption, a centre-to-centre pore distance around 4.9 nm would be more representative than the 5.7 nm obtained for a hexagonal arrangement of channels.

Finally, the effect of synthesis reaction time and amount of seeds was evaluated by nitrogen adsorption analysis. Figure 26 shows the adsorption isotherms and PSD of four representative samples synthesised under the optimized stirring conditions. The corresponding textural properties are summarized in Table 4, being compared with the textural properties of the MCM-41 nanoparticles used as a reference.

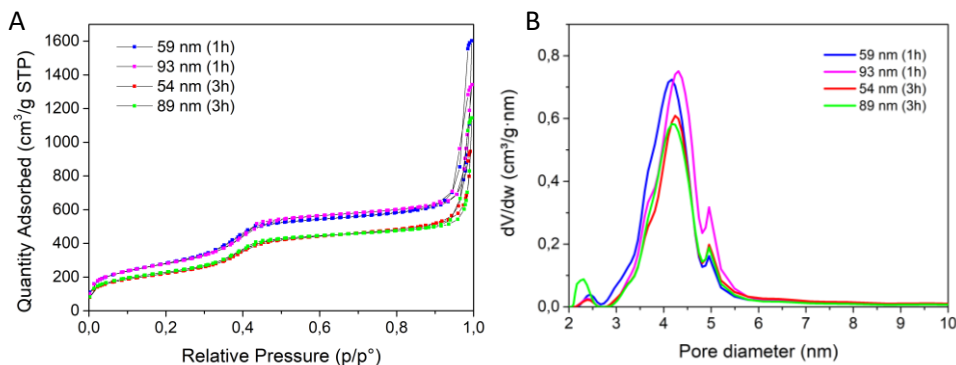


**Figure 26:** (A) Adsorption-desorption isotherms and (B) PSD from core-shell M-MSNs with different sizes and synthesised in 1h/3h.



**Table 4:** Textural properties of core-shell M-MSNs of different sizes and synthesis reaction times of 1 h vs 3 h. <sup>a)</sup> Specific surface area determined by the multipoint BET method using the adsorption data in the range of relative pressures ( $P/P_0$ ) of 0.05-0.15 and a surface cross-sectional area of nitrogen of  $13.50 \text{ \AA}^2$ . <sup>b)</sup> Average pore size determined from the isotherm using the DFT method. <sup>c)</sup> Pore volumes were calculated directly from the isotherm at a relative pressure corresponding to complete filling of the mesopores:  $P/P_0=0.55$  for the core-shell M-MSNs and  $P/P_0=0.4$  for the MCM-41 NPs.

Sample	Reaction time (h)	$d_{\text{TEM}}$ (nm)	$A_{\text{BET}}^{\text{a)}$ ( $\text{m}^2/\text{g}$ )	$d_p^{\text{b)}$ (nm)	$V_p^{\text{c)}$ ( $\text{cm}^3/\text{g}$ )
1	1	59	847	4.2	0.825
2	1	93	842	4.3	0.856
3	3	54	667	4.2	0.669
4	3	89	699	4.2	0.677
MCM41-NPs			881	3.5	0.732

The obtained results revealed that variation of the initial amount of seeds or reaction time had little effect on the size of the mesoporous channels of the core-shell M-MSNs, which presented a diameter between 4.2 and 4.3 nm. This value is in perfect agreement with the 4.5 nm obtained when measuring the CTAB micelles present in the initial reaction mixture (see chapter 4). The size difference between the channels of the MCM-41 NPs and the core-shell M-MSNs (around 0.7-0.8 nm) was attributed to the greater lattice contraction experienced by the MCM-41 material during calcination. It is important to note that this small difference can be critical for loading large therapeutically-relevant biomolecules, as suggested in a recent work about the delivery of siRNA from core-shell MSNs.<sup>65</sup>

The obtained core-shell M-MSNs presented comparable and even larger specific pore volumes and surface areas than the MCM-41 nanoparticles. However, it was observed that increasing the reaction time from 1 h to 3 h significantly reduced the specific pore volumes and surface area of the particles, suggesting a partial blockage of the channels probably due to the increase of aggregation between particles. This effect was not observed when comparing nanoparticles of different sizes that were synthesised under similar reaction times (sample 1 vs sample 2 or sample 3 vs sample 4).

## 5.4. Conclusions

In this chapter, the structural properties of core-shell M-MSNs and MCM-41 nanoparticles have been thoroughly investigated using powder XRD analysis, nitrogen adsorption analysis and electron microscopy.

The obtained results have confirmed that the core-shell M-MSNs are composed of wormhole-like channels arranged in a radial distribution, in agreement with a seeded-growth formation mechanism. This particular arrangement of channels together with the spherical shape of the particles imposes physical restrictions to the development of long-range order within the structure. Nonetheless, an intense diffraction peak is obtained in this type of nanoparticles, which suggests that certain order exists in the arrangement of the channels at the local level.

The position and broadness of the main diffraction peak gave valuable information about the internal structural order of the core-shell M-MNs. In particular, the stirring conditions used during the synthesis were identified as the main cause of variability in the formation of the mesoporous silica structure. Remarkably, application of the optimized stirring conditions developed in this project led to core-shell M-MSNs that exhibited very similar diffraction patterns independently of the size of the resulting nanoparticles. A centre-to-centre pore distance in the range 4.9-5.7 nm was determined based on the two geometries proposed for the interpretation of the diffraction data.

Nitrogen adsorption analysis was used to analyse the textural properties of the obtained materials. Despite the different arrangement of pores exhibited by the MCM-41 MSNs and the core-shell M-MSNs, similar type IV isotherms were obtained in both cases together with comparable specific surface areas and pore volumes. The application of DFT methods was especially relevant in order to accurately determine the average mesopore size of the core-shell M-MSNs (4.2 nm).

Finally, two important conclusions were drawn concerning the effect of the reaction parameters on the textural properties of the core-shell M-MSNs:

- Increasing the stirring rate of the reaction leads to more disordered structures with larger mesopore sizes and higher loading capacities.

- Extended reaction times (3 h) lead to a reduction of the specific pore volume of the nanoparticles.

## 5.5. References

- (1) Beck, J. S.; Vartuli, J. C.; Roth, W. J.; Leonowicz, M. E.; Kresge, C. T.; Schmitt, K. D.; Chu, C. T.-W.; Olson, D. H.; Sheppard, E. W.; McCullen, S. B.; Higgins, J. B.; Schlenker, J. L. *J. Am. Chem. Soc.* **1992**, No. 14, 10834–10843.
- (2) Kresge, C. T.; Leonowicz, M. E.; Roth, W. J.; Vartuli, J. C.; Beck, J. S. *Nature* **1992**, 359 (22), 710–712.
- (3) Barton, T. J.; Bull, L. M.; Klemperer, W. G.; Loy, D. A.; McEnaney, B.; Misono, M.; Monson, P. A.; Pez, G.; Schere, G. W.; Vartuli, J. C.; Yaghi, O. M. *Chem. Mater.* **1999**, 11 (10), 2633–2656.
- (4) Cullity, B. D.; Stock, S. R. *Elements of X-Ray Diffraction*, Third Edit.; Pearson, **2014**.
- (5) *Powder Diffraction Theory and Practice*; Dinnebier, R. E., Billinge, S. J. L., Eds.; RSC Publishing, 2008.
- (6) Solovyov, L. A.; Kirik, S. D.; Shmakov, A. N.; Romannikov, V. N. *Microporous Mesoporous Mater.* **2001**, 44–45, 17–23.
- (7) Solovyov, L. A. *Chem. Soc. Rev.* **2013**, 42 (9), 3708–3720.
- (8) Zhang, L.; Qiao, S.; Jin, Y.; Yang, H.; Budihartono, S.; Stahr, F.; Yan, Z.; Wang, X.; Hao, Z.; Lu, G. Q. *Adv. Funct. Mater.* **2008**, 18, 3203–3212.
- (9) Chan, H. B. S.; Budd, P. M.; De Naylor, T. V. *J. Mater. Chem.* **2001**, 11 (3), 951–957.
- (10) Schumacher, K.; Ravikovitch, P. I.; Chesne, A. Du; Neimark, A. V.; Unger, K. K. *Langmuir* **2000**, 16 (8), 4648–4654.
- (11) Huo, Q.; Margolese, D. I.; Ciesla, U.; Demuth, D. G.; Feng, P.; Gier, T. E.; Sieger, P.; Firouzi, A.; Chmelka, B. F.; Schuth, F.; Stucky, G. D. *Chem. Mater.* **1994**, 6 (8), 1176–1191.
- (12) Huo, Q.; Leon, R.; Petroff, P. M.; Stucky, G. D. *Science*. **1995**, 268 (5215), 1324–1327.
- (13) Kim, J.; Kim, H. S.; Lee, N.; Kim, T.; Kim, H.; Yu, T.; Song, I. C.; Moon, W. K.; Hyeon, T. *Angew. Chem. Int. Ed.* **2008**, 47 (44), 8438–8441.
- (14) Zhang, J.; Li, X.; Rosenholm, J. M.; Gu, H. J. *Colloid Interface Sci.* **2011**, 361 (1), 16–24.
- (15) Nyalosaso, J. L.; Rascol, E.; Pisani, C.; Dorandeu, C.; Dumail, X.; Maynadier, M.; Gary-Bobo, M.; Kee Him, J. L.; Bron, P.; Garcia, M.; Devoisselle, J. M.; Prat, O.; Guari, Y.; Charnay, C.; Chopineau, J. *RSC Adv.* **2016**, 6 (62), 57275–57283.
- (16) Davis, M. E.; Chen, C.-Y.; Burkett, S. L.; Lobo, R. F. *Mat.Res.Soc.Symp.Proc.* **1994**, 346, 831–842.
- (17) Chen, C.-Y.; Burkett, S. L.; Li, H.-X.; Davis, M. E. *Microporous Mater.* **1993**, 2, 27–34.
- (18) Chen, C. Y.; Xiao, S. Q.; Davis, M. E. *Microporous Mater.* **1995**, 4 (1), 1–20.

- (19) Schacht, S.; Janicke, M.; Schüth, F. *Microporous Mesoporous Mater.* **1998**, *22* (1–3), 485–493.
- (20) Bagshaw, S. A.; Prouzet, E.; Pinnavaia, T. J. *Science* (80-. ). **1995**, *269*, 1242–1244.
- (21) Ryoo, R.; Kim, J. M.; Ko, C. H.; Shin, C. H. *J. Phys. Chem.* **1996**, *100* (45), 17718–17721.
- (22) Ryoo, R.; Kim, J. M.; Shin, C. H.; Lee, J. Y. *Stud. Surf. Sci. Catal.* **1997**, *105*, 45–52.
- (23) Buchel, G.; Grun, M.; Unger, K. K.; Matsumoto, A.; Tsutsumi, K. *Supramol. Sci.* **1998**, *5* (3–4), 253–259.
- (24) Grun, M.; Buchel, G.; Kumar, D.; Schumacher, K.; Bidlingmaier, B.; Unger, K. K. *Stud. Surf. Sci. Catal.* **2000**, *128* (5), 155–165.
- (25) Huo, Q.; Feng, J.; Schüth, F.; Stucky, G. D. *Chem. Mater.* **1997**, *9* (1), 14–17.
- (26) Yang, H.; Vovk, G.; Coombs, N.; Sokolov, I.; Ozin, G. A. *J. Mater. Chem.* **1998**, *8* (3), 743–750.
- (27) Luo, Q.; Li, L.; Xue, Z.; Zhao, D. In *Studies in Surface Science and Catalysis 129*; 2000; pp 37–43.
- (28) Pauwels, B.; Van Tendeloo, G.; Thoelen, C.; Van Rhijn, W.; Jacobs, P. A. *Adv. Mater.* **2001**, *41* (17), 1317–1320.
- (29) Dullien, F. A. L. *Porous Media: Fluid Transport and Pore Structure*, Second Edi.; Academic Press: San Diego, 1992.
- (30) De Graef, M.; McHenry, M. E. *Structure of Materials*; Cambridge University Press, **2007**.
- (31) Gille, W. *Particle and particle systems characterization: small-angle scattering (SAS) applications*; CRC Press, **2013**.
- (32) Rouquerol, F.; Rouquerol, J.; Sing, K. S. W.; Llewellyn, P.; Maurin, G. *Adsorption by Powders and Porous Solids*, Second Edi.; Elsevier, **2014**.
- (33) Lowell, S.; Shields, J. E.; Thomas, M. A.; Thommes, M. *Characterization of Porous Solids and Powders: Surface Area, Pore Size and Density*; Kluwer Academic Publishers, **2004**; Vol. 16.
- (34) *Nanoporous Materials: Science and Engineering*; Lu, G. Q., Zhao, X. S., Eds.; Imperial College Press, 2004; Vol. 4.
- (35) Butt, H.-J.; Graf, K.; Kappl, M. *Physics and Chemistry of Interfaces*; Wiley-VCH: Weinheim, **2003**.
- (36) Thommes, M.; Kaneko, K.; Neimark, A. V.; Olivier, J. P.; Rodriguez-Reinoso, F.; Rouquerol, J.; Sing, K. S. W. *Pure Appl. Chem.* **2015**, *87* (9–10), 1051–1069.
- (37) Thommes, M.; Cychoz, K. A. *Adsorption* **2014**, *20* (2–3), 233–250.
- (38) Morishige, K.; Tateishi, M. *Langmuir* **2006**, *22* (9), 4165–4169.
- (39) Cai, Q.; Luo, Z. S.; Pang, W. Q.; Fan, Y. W.; Chen, X. H.; Cui, F. Z. *Chem. Mater.* **2001**, *13* (2), 258–263.
- (40) Froba, M.; Thommes, M.; Ko, R. *Appl. Surf. Sci.* **2002**, *196*, 239–249.

- (41) Branton, P. J.; Hall, P. G.; Sing, K. S. W.; Reichert, H.; Schüth, F.; Unger, K. K. *J. Chem. Soc., Faraday Trans.* **1994**, *90* (19), 2965–2967.
- (42) Ravikovitch, P. I.; O’Domhnaill, S. C.; Neimark, A. V.; Schiith, F.; Unger, K. K. *Langmuir* **1995**, *11* (12), 4765–4772.
- (43) Brunauer, S.; Emmett, P. H.; Teller, E. *J. Am. Chem. Soc.* **1938**, *60* (2), 309–319.
- (44) Cychosz, K. A.; Guillet-Nicolas, R.; García-Martínez, J.; Thommes, M. *Chem. Soc. Rev.* **2017**, *46* (2), 389–414.
- (45) Rouquerol, J.; Llewellyn, P.; Rouquerol, F. *Stud. Surf. Sci. Catal.* **2007**, *160*, 49–56.
- (46) Gregg, S. J.; Sing, K. S. W. *Adsorption, Surface Area and Porosity*, Second Ed.; Academic Press: London, 1982.
- (47) Emmett, P. H.; Brunauer, S. *J. Am. Chem. Soc.* **1937**, *59* (8), 1553–1564.
- (48) Dutartre, R.; Di Renzo, F.; Galarneau, A.; Desplandier, D. *Microporous Mesoporous Mater.* **1999**, *27* (2–3), 297–308.
- (49) Jelinek, L.; Kováts, E. sz. *Langmuir* **1994**, *10* (11), 4225–4231.
- (50) Gurvich, L. *J. Phys. Chem. Soc. Russ.* **1915**, *47*, 805.
- (51) Nooney, R. I.; Thirunavukkarasu, D.; Yimei, C.; Josephs, R.; Ostafin, A. E. *Chem. Mater.* **2002**, *14* (11), 4721–4728.
- (52) Möller, K.; Kobler, J.; Bein, T. *Adv. Funct. Mater.* **2007**, *17* (4), 605–612.
- (53) Nyalosaso, J. L.; Rascol, E.; Pisani, C.; Dorandeu, C.; Dumail, X.; Maynadier, M. *RSC Adv.* **2016**, *6*, 57275–57283.
- (54) Barrett, E. P.; Joyner, L. G.; Halenda, P. P. *J. Am. Chem. Soc.* **1951**, *73* (1), 373–380.
- (55) Thommes, M. In *Nanoporous Materials: Science and Engineering*; **2004**; pp 317–364.
- (56) Seaton, N. A.; Walton, J. P. R. B.; Quirk, N. *Carbon N. Y.* **1989**, *27* (6), 853–861.
- (57) Evans, R.; Tarazona, P. *Phys. Rev. Lett.* **1984**, *52* (7), 557–560.
- (58) Papadopoulou, A.; Van Swol, F.; Marconi, U. M. B. *J. Chem. Phys.* **1992**, *97* (9), 6942–6952.
- (59) Peterson, B. K.; Gubbins, K. E. *Mol. Phys.* **1987**, *62* (1), 215–226.
- (60) Lai, C. Y.; Trewyn, B. G.; Jeftinija, D. M.; Jeftinija, K.; Xu, S.; Jeftinija, S.; Lin, V. S. Y. *J. Am. Chem. Soc.* **2003**, *125* (15), 4451–4459.
- (61) Landers, J.; Gor, G. Y.; Neimark, A. V. *Colloids Surfaces A Physicochem. Eng. Asp.* **2013**, *437*, 3–32.
- (62) Chiche, D.; Digne, M.; Revel, R.; Chanéac, C.; Jolivet, J.-P. *J. Phys. Chem. C* **2008**, *112* (23), 8524–8533.
- (63) Edler, K. J.; Reynolds, P. A.; White, W.; Cookson, D.; White, J. W.; Cookson, D. *J. Chem. Soc. Faraday Trans.* **1997**, *93* (Di), 199–202.
- (64) Zhang, L.; Wang, Y.; Tang, Y.; Jiao, Z.; Xie, C.; Zhang, H.; Gu, P.; Wei, X.; Yang,

- G.-Y.; Gu, H.; Zhang, C. *Nanoscale* **2013**, 5 (10), 4506–4516.
- (65) Möller, K.; Bein, T. *Chem. Mater.* **2017**, 29 (1), 371–388.
- (66) Möller, K.; Müller, K.; Engelke, H.; Bräuchle, C.; Wagner, E.; Bein, T. *Nanoscale* **2016**, 8 (7), 4007–4019.





## **Chapter 6:**

### ***General conclusions***



## 6.1. Conclusions

In this thesis, a comprehensive study about the synthesis and characterization of core-shell M-MSNs has been presented. The design of a reproducible synthetic protocol has received special attention with the aim of preparing high-quality nanoparticles that could be used for the development of theranostic nanodevices with application in nanomedicine.

**Chapter 3** shows that highly versatile iron oxide nanoparticles can be prepared using a simple and cost-effective coprecipitation method. The application of a size-selective precipitation procedure has proved to be an effective strategy to obtain highly-stable nanoparticles with a balanced distribution of sizes centered around 10 nm. The obtained results suggest that the magnetic nanoparticles are coated with a monolayer of highly-packed oleate molecules, which may be responsible for their enhanced chemical and colloidal stability. As a result, the obtained magnetic nanoparticles can be stored for extended periods of time and be used as seeds for the preparation of core-shell M-MSNs.

The optimized nanoparticles exhibit high saturation magnetization and show good heating efficiency in magnetic hyperthermia experiments. Moreover, relaxivity measurements revealed that the nanoparticles are also able to provide significant dual  $T1/T2$  signal enhancement. This indicates that the developed USPIOs are excellent candidates for the development of theranostic nanodevices with potential application in both hyperthermia and dual  $T1/T2$  MR imaging.

In **Chapter 4** monodisperse core-shell M-MSNs are synthesized through a surfactant templated seeded-growth strategy. The initial attempts to prepare nanoparticles with well-defined physico-chemical properties have shown that multiple reaction parameters are involved in the synthesis of this type of nanoparticles. The main problems detected are related to the control over the number of seeds per nanoparticle, the aggregation between particles, the structure of the mesoporous silica shell and the final size of the core-shell M-MSNs. The consideration of the possible mechanisms involved in the reaction and the application of a semi-empirical model provided a reference framework to

understand and predict the effect that different reaction parameters have on the reaction.

The stirring conditions applied have been identified as a crucial reaction parameter for the reproducible synthesis of core-shell M-MSNs. To the best of our knowledge, this is the first time that stirring conditions are thoroughly assessed and directly related to the physico-chemical properties of the resulting nanoparticles. An optimized sequential stirring protocol has been proposed in which high stirring rates are applied during the first 2 minutes of reaction followed by a reduction of stirring intensity, leading to core-shell M-MSNs with a single magnetic core and ordered mesoporous silica structures.

A clear relation has also been observed between the initial amount of magnetic seeds used in the reaction and the final size of the core-shell M-MSNs: increasing the amount of seeds leads to nanoparticles with thinner silica shells. All these results can be explained based on the preferential assembly of silica-coated micelles around the magnetic seeds, a formation mechanism that was supported by the predictions of the semi-empirical model developed.

The time of reaction has also been identified as a key reaction parameter. Reaction times under 1 h are usually required in order to avoid the formation of aggregates, a process that is also highly influenced by the initial amount of seeds used in the reaction.

**Chapter 5** presents a detailed analysis about the structural characterization of mesoporous silica materials and, in particular, MSNs with a radial distribution of wormhole-like channels.

The obtained core-shell M-MSNs are characterized by a single X-ray diffraction peak, which position and broadness can be used to assess the centre-to-centre pore distance and structural order between different samples. This type of nanoparticles also exhibit type IV adsorption isotherms with negligible hysteresis when working with nitrogen at 77 °K.

Application of DFT methods is advised for the determination of the PSD in this type of nanoparticles, since the widely used BJH method leads to a significant underestimation of mesopore sizes. Under the optimized reaction conditions

established in this work, 4.2 nm mesoporous channels with an average centre-to-centre pore distance in the range of 4.9-5.7 nm are obtained. As a result, the obtained core-shell M-MSNs exhibit large specific surface areas and pore volumes, which are comparable to those displayed by reference MCM-41-type nanoparticles.

Stirring conditions have been shown to highly influence the structural properties of the resulting nanoparticles, from the arrangement of the mesoporous channels to the size of the mesopores and the pore volume of the core-shell M-MSNs. Moreover, excessive times of reaction have been shown to be detrimental, leading to a significant reduction of the pore volumes.

Overall, we believe that the reproducibility and control achieved by the developed synthetic protocol is a first step towards the industrial production of this type of nanoparticles, which hold great promise for the development of future applications in the field of nanomedicine.

